



Universiteit Gent
Faculteit Wetenschappen
Vakgroep Fysica en Sterrenkunde

² No title yet

³ No sub-title neither, obviously...

⁴ Alexis Fagot

5



Thesis to obtain the degree of
Doctor of Philosophy in Physics
Academic years 2012-2017



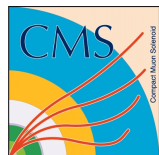


Universiteit Gent
Faculteit Wetenschappen
Vakgroep Fysica en Sterrenkunde

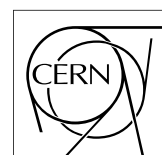
Promotoren: Dr. Michael Tytgat
Prof. Dr. Dirk Ryckbosch

Universiteit Gent
Faculteit Wetenschappen
Vakgroep Fysica en Sterrenkunde
Proeftuinstraat 86, B-9000 Gent, België
Tel.: +32 9 264.65.28
Fax.: +32 9 264.66.97

17



Thesis to obtain the degree of
Doctor of Philosophy in Physics
Academic years 2012-2017



Acknowledgements

¹⁹ Ici on remerciera tous les gens que j'ai pu croiser durant cette aventure et qui m'ont permis de passer
²⁰ un bon moment

²¹ *Gent, ici la super date de la mort qui tue de la fin d'écriture*
²² *Alexis Fagot*

Table of Contents

24	Acknowledgements	i
25	Nederlandse samenvatting	vii
26	English summary	ix
27	1 Introduction	1-1
28	1.1 A story of High Energy Physics	1-1
29	1.2 Organisation of this study	1-1
30	2 Investigating the TeV scale	2-1
31	2.1 The Standard Model of Particle Physics	2-2
32	2.1.1 A history of particle physics	2-2
33	2.1.2 Construction and test of the model [TO SEE IF KEPT - MAYBE TOO COMPLEX]	2-8
34	2.1.3 Investigating the TeV scale	2-9
35	2.2 The Large Hadron Collider & the Compact Muon Solenoid	2-9
36	2.2.1 LHC, the most powerful particle accelerator	2-9
37	2.2.1.1 Particle acceleration	2-10
38	2.2.1.2 LHC discoveries and LHC physics program	2-13
39	2.2.1.3 High Luminosity LHC	2-14
40	2.2.2 CMS, a multipurpose experiment	2-14
41	2.3 Muon Phase-II Upgrade	2-14
42		
43	3 Physics of Resistive plate chambers	3-1
44	3.1 Principle	3-1
45	3.1.1 Electron drift velocity	3-4
46	3.2 Rate capability and time resolution of Resistive Plate Chambers	3-4
47	3.2.1 Operation modes	3-4
48	3.2.2 Detector designs and performance	3-6
49	3.2.2.1 Double-gap RPC	3-7
50	3.2.2.2 Multigap RPC (MRPC)	3-8
51	3.2.2.3 Charge distribution and performance limitations	3-9
52	3.3 Signal formation	3-12
53	3.4 Gas transport parameters	3-12
54	4 Longevity studies and Consolidation of the present CMS RPC subsystem	4-1
55	4.1 Resistive Plate Chambers at CMS	4-1
56	4.1.1 Overview	4-1
57	4.1.2 The present RPC system	4-2
58	4.1.3 Pulse processing of CMS RPCs	4-3

59	4.2	Testing detectors under extreme conditions	4-4
60	4.2.1	The Gamma Irradiation Facilities	4-7
61	4.2.1.1	GIF	4-7
62	4.2.1.2	GIF++	4-9
63	4.3	Preliminary tests at GIF	4-11
64	4.3.1	Resistive Plate Chamber test setup	4-11
65	4.3.2	Data Acquisition	4-13
66	4.3.3	Geometrical acceptance of the setup layout to cosmic muons	4-13
67	4.3.3.1	Description of the simulation layout	4-14
68	4.3.3.2	Simulation procedure	4-16
69	4.3.3.3	Results	4-17
70	4.3.4	Photon flux at GIF	4-17
71	4.3.4.1	Expectations from simulations	4-17
72	4.3.4.2	Dose measurements	4-22
73	4.3.5	Results and discussions	4-23
74	4.4	Longevity tests at GIF++	4-24
75	4.4.1	Description of the Data Acquisition	4-27
76	4.4.2	RPC current, environmental and operation parameter monitoring	4-28
77	4.4.3	Measurement procedure	4-29
78	4.4.4	Longevity studies results	4-29
79	5	Investigation on high rate RPCs	5-1
80	5.1	Rate limitations and ageing of RPCs	5-1
81	5.1.1	Low resistivity electrodes	5-1
82	5.1.2	Low noise front-end electronics	5-1
83	5.2	Construction of prototypes	5-1
84	5.3	Results and discussions	5-1
85	6	Conclusions and outlooks	6-1
86	6.1	Conclusions	6-1
87	6.2	Outlooks	6-1
88	A	A data acquisition software for CAEN VME TDCs	A-1
89	A.1	GIF++ DAQ file tree	A-1
90	A.2	Usage of the DAQ	A-2
91	A.3	Description of the readout setup	A-3
92	A.4	Data read-out	A-3
93	A.4.1	V1190A TDCs	A-4
94	A.4.2	DataReader	A-6
95	A.4.3	Data quality flag	A-10
96	A.5	Communications	A-12
97	A.5.1	V1718 USB Bridge	A-13
98	A.5.2	Configuration file	A-13
99	A.5.3	WebDCS/DAQ intercommunication	A-17
100	A.5.4	Example of inter-process communication cycle	A-18
101	A.6	Software export	A-18

102	B Details on the offline analysis package	B-1
103	B.1 GIF++ Offline Analysis file tree	B-1
104	B.2 Usage of the Offline Analysis	B-2
105	B.2.1 Output of the offline tool	B-3
106	B.2.1.1 ROOT file	B-3
107	B.2.1.2 CSV files	B-5
108	B.3 Analysis inputs and information handling	B-6
109	B.3.1 Dimensions file and IniFile parser	B-6
110	B.3.2 TDC to RPC link file and Mapping	B-7
111	B.4 Description of GIF++ setup within the Offline Analysis tool	B-9
112	B.4.1 RPC objects	B-9
113	B.4.2 Trolley objects	B-10
114	B.4.3 Infrastructure object	B-11
115	B.5 Handeling of data	B-12
116	B.5.1 RPC hits	B-13
117	B.5.2 Clusters of hits	B-14
118	B.6 DAQ data Analysis	B-15
119	B.6.1 Determination of the run type	B-16
120	B.6.2 Beam time window calculation for efficiency runs	B-17
121	B.6.3 Data loop and histogram filling	B-18
122	B.6.4 Results calculation	B-19
123	B.6.4.1 Rate normalisation	B-19
124	B.6.4.2 Rate and activity	B-21
125	B.6.4.3 Strip masking tool	B-23
126	B.6.4.4 Output CSV files filling	B-25
127	B.7 Current data Analysis	B-29

¹²⁸

Nederlandse samenvatting –Summary in Dutch–

¹²⁹

¹³⁰ Le resume en Neerlandais (j'aurais peut-être pu apprendre la langue juste pour ça...).

¹³¹

English summary

¹³² Le meme résume mais en Anglais (on commencera par la hein!).

List of Figures

133

134 2.1	Through the gold foil experiment Rutherford could show that most of the mass of 135 atoms was contained in a positively charged nucleus and could then propose a more 136 accurate atomic model than that of Thomson.	2-3
137 2.2	Figure 2.2a: Meson octet. Figure 2.2b: Baryon octet. Figure 2.2c: Baryon decuplet. .	2-7
138 2.3	CERN accelerator complex.	2-10
139 2.4	Pictures of the different accelerators. From top to bottom: first the LINAC 2 and the 140 <i>Pb</i> source of LINAC 3. Then the Booster and the LEIR. Finally, the PS, the SPS and 141 the LHC.	2-12
142 2.5	Figure 2.5a: schematics of the LHC cryodipoles. 1: Superconducting Coils, 2: Beam 143 pipe, 3: Heat exchanger Pipe, 4: Helium-II Vessel, 5: Superconducting Bus-bar, 6: 144 Iron Yoke, 7: Non-Magnetic Collars, 8: Vacuum Vessel, 9: Radiation Screen, 10: 145 Thermal Shield, 11: Auxiliary Bus-bar Tube, 12: Instrumentation Feed Throughs, 146 13: Protection Diode, 14: Quadrupole Bus-bars, 15: Spool Piece Bus-bars. Fig- 147 ure 2.5b: magnetic field and resulting motion force applied on the beam particles. .	2-13
148 2.6	Figure 2.6a: picture of the LHC quadrupoles. Figure 2.6b: magnetic fields and 149 resulting focussing force applied on the beam by 2 consecutive quadrupoles.	2-13
150 2.7	Absorbed dose in the CMS cavern after an integrated luminosity of 3000 fb. R is the 151 transverse distance from the beamline and Z is the distance along the beamline from 152 the Interaction Point at Z=0.	2-14
153 2.8	A quadrant of the muon system, showing DTs (yellow), RPCs (light blue), and CSCs 154 (green). The locations of new forward muon detectors for Phase-II are contained 155 within the dashed box and indicated in red for GEM stations (ME0, GE1/1, and 156 GE2/1) and dark blue for improved RPC (iRPC) stations (RE3/1 and RE4/1).	2-15
157 2.9	RMS of the multiple scattering displacement as a function of muon p_T for the pro- 158 posed forward muon stations. All of the electromagnetic processes such as bremsstrahlung 159 and magnetic field effect are included in the simulation.	2-16
160 3.1	Different phases of the avalanche development in the RPC gas volume subjected to 161 a constant electric field E_0 . a) An avalanche is initiated by the primary ionisation 162 caused by the passage of a charged particle through the gas volume. b) Due to 163 its growing size, the avalanche starts to locally influence the electric field. c) The 164 electrons, lighter than the cations reach the anode first. d) The ions reach the cathode. 165 While the charges have not recombined, the electric field in the small region around 166 the avalanche stays affected and locally blind the detector.	3-2
167 3.2	Effeciency (circles and stars with 30 mV and 100 mV thresholds respectively) and 168 streamer probability (opened circles) as function of the operating voltatge of a 2 mm 169 single gap HPL RPC flushed with a gas mixture containing (a) 5%, (b) 2%, (c) 1% 170 and (d) no SF_6 [33].	3-3

171	3.3 Movement of the charge carriers in an RPC. Figure 3.3a: Voltage across an RPC whose electrode have a relative permittivity of 5 at the moment the tension s applied. Figure 3.3b: After the charge carriers moved, the electrodes are charged and there is no voltage drop over the electrodes anymore. The full potential is applied on the gas gap only. Figure 3.3c: The streamer discharge initiated by a charged particle transports electrons and cations towards the anode and cathode respectively.	3-5
172		
173		
174		
175		
176		
177	3.4 Typical oscilloscope pulses in streamer mode (Figure 3.4a) and avalanche mode(Figure 3.4b). In the case of streamer mode, the very small avalanche signal is visible.	3-5
178		
179		
180		
181		
182	3.5 Rate capability comparison for the streamer and avalanche mode of operation. An order of magnitude in rate capability for a maximal efficiency drop of 10% is gained by using the avalanche mode over the streamer mode.	3-6
183		
184		
185		
186		
187		
188	3.6 Possible double-gap RPC layouts: a) "standard" 1D double-gap RPC, as used in CMS experiment, where the anodes are facing each other and a 1D read-out plane is sandwiched in between them, b) double read-out double-gap RPC as used in AT-LAS experiment, where the cathodes are facing each other and 2 read-out planes are used on the outer surfaces. This last layout can offer the possibility to use a 2D reconstruction by using orthogonal read-out planes.	3-7
189		
190		
191	3.7 Comparison of performance of CMS double and single gap RPCs using cosmic muons [44]. Figure 3.7a: Comparison of efficiency sigmoids. Figure 3.7b: Voltage distribution at 95% of maximum efficiency. Figure 3.7c: $\Delta_{10\%}^{90\%}$ distribution. . . .	3-7
192		
193		
194		
195	3.8 Presentation of ALICE MRPC using 250 μm gas gaps, 620 μm outer glass electrodes and 550 μm inner floating electrodes. More details on the labels are given in [45]. . .	3-8
196		
197		
198	3.9 Particle identification applied to electrons in the STAR experiment. The identification is performed combining ToF and dE/dx measurements [50].	3-9
199		
200		
201	3.10 Comparison of the detector performance of ALICE ToF MRPC [51] at fixed applied voltage (in blue) and at fixed effective voltage (in red). The effective voltage is kept fixed by increasing the applied voltage accordingly to the current drawn by the detector.	3-9
202		
203		
204		
205	3.11 Ratio between total induced and drifting charge have been simulated for single gap, double-gap and multigap layouts [52]. The total induced charge for a double-gap RPC is a factor 2 higher than for a multigap.	3-10
206		
207		
208	3.12 Charge spectra have been simulated for single gap, double-gap and multigap layouts [52]. It appears that when single gap shows a decreasing spectrum, double and multigap layouts exhibit a spectrum whose peak is detached from the origin. The detachment gets stronger as the number of gaps increases.	3-11
209		
210		
211		
212	3.13 The maximal theoretical efficiency is simulated for single gap, double-gap and multi-gap layouts [52] at a constant gap thickness of 2 mm and using an effective Townsend coefficient of 9 mm^{-1}	3-11
213		
214		
215		
216		
217		
218		
219		
220		
221		
222		
223		
224		
225		
226		
227		
228		
229		
230		
231		
232		
233		
234		
235		
236		
237		
238		
239		
240		
241		
242		
243		
244		
245		
246		
247		
248		
249		
250		
251		
252		
253		
254		
255		
256		
257		
258		
259		
260		
261		
262		
263		
264		
265		
266		
267		
268		
269		
270		
271		
272		
273		
274		
275		
276		
277		
278		
279		
280		
281		
282		
283		
284		
285		
286		
287		
288		
289		
290		
291		
292		
293		
294		
295		
296		
297		
298		
299		
300		
301		
302		
303		
304		
305		
306		
307		
308		
309		
310		
311		
312		
313		
314		
315		
316		
317		
318		
319		
320		
321		
322		
323		
324		
325		
326		
327		
328		
329		
330		
331		
332		
333		
334		
335		
336		
337		
338		
339		
340		
341		
342		
343		
344		
345		
346		
347		
348		
349		
350		
351		
352		
353		
354		
355		
356		
357		
358		
359		
360		
361		
362		
363		
364		
365		
366		
367		
368		
369		
370		
371		
372		
373		
374		
375		
376		
377		
378		
379		
380		
381		
382		
383		
384		
385		
386		
387		
388		
389		
390		
391		
392		
393		
394		
395		
396		
397		
398		
399		
400		
401		
402		
403		
404		
405		
406		
407		
408		
409		
410		
411		
412		
413		
414		
415		
416		
417		
418		
419		
420		
421		
422		
423		
424		
425		
426		
427		
428		
429		
430		
431		
432		
433		
434		
435		
436		
437		
438		
439		
440		
441		
442		
443		
444		
445		
446		
447		
448		
449		
450		
451		
452		
453		
454		
455		
456		
457		
458		
459		
460		
461		
462		
463		
464		
465		
466		
467		
468		
469		
470		
471		
472		
473		
474		
475		
476		
477		
478		
479		
480		
481		
482		
483		
484		
485		
486		
487		
488		
489		
490		
491		
492		
493		
494		
495		
496		
497		
498		
499		
500		
501		
502		
503		
504		
505		
506		
507		
508		
509		
510		
511		
512		
513		
514		
515		
516		
517		
518		
519		
520		
521		
522		
523		
524		
525		
526		
527		
528		
529		
530		
531		
532		
533		
534		
535		
536		
537		
538		
539		
540		
541		
542		
543		
544		
545		

212	4.2	Description of the principle of a CFD. A comparison of threshold triggering (left) 213 and constant fraction triggering (right) is shown in Figure 4.2a. Constant fraction 214 triggering is obtained thanks to zero-crossing technique as explained in Figure 4.2b. 215 The signal arriving at the input of the CFD is split into three components. A first 216 one is delayed and connected to the inverting input of a first comparator. A sec- 217 ond component is connected to the noninverting input of this first comparator. A 218 third component is connected to the noninverting input of another comparator along 219 with a threshold value connected to the inverting input. Finally, the output of both 220 comparators is fed through an AND gate.	4-4
221	4.3	(4.3a) Extrapolation from 2016 data of single hit rate per unit area in the barrel 222 region. (4.3b) Extrapolation from 2016 data of single hit rate per unit area in the 223 endcap region.	4-6
224	4.4	Background Fluka simulation compared to 2016 Data at $L = 10^{34} \text{ cm}^{-2} \cdot \text{s}^{-1}$ in 225 the fourth endcap disk region. A mismatch in between simulation and data can be 226 observed. [To be understood.]	4-7
227	4.5	Layout of the test beam zone called X5c GIF at CERN. Photons from the radioactive 228 source produce a sustained high rate of random hits over the whole area. The zone is 229 surrounded by 8 m high and 80 cm thick concrete walls. Access is possible through 230 three entry points. Two access doors for personnel and one large gate for material. 231 A crane allows installation of heavy equipment in the area.	4-8
232	4.6	^{137}Cs decays by β^- emission to the ground state of ^{137}Ba (BR = 5.64%) and via the 233 662 keV isomeric level of ^{137}Ba (BR = 94.36%) whose half-life is 2.55 min.	4-9
234	4.7	Floor plan of the GIF++ facility. When the facility downstream of the GIF++ takes 235 electron beam, a beam pipe is installed along the beam line (z-axis). The irradiator 236 can be displaced laterally (its center moves from $x = 0.65$ m to 2.15 m), to increase 237 the distance to the beam pipe.	4-9
238	4.8	Simulated unattenuated current of photons in the xz plane (Figure 4.8a) and yz plane 239 (Figure 4.8b) through the source at $x = 0.65$ m and $y = 0$ m. With angular correction 240 filters, the current of 662 keV photons is made uniform in xy planes.	4-10
241	4.9	Description of the RPC setup. Dimensions are given in mm. A tent containing RPCs 242 is placed at 1720 mm from the source container. The source is situated in the center 243 of the container. RE-4-2-BARC-161 chamber is 160 mm inside the tent. This way, 244 the distance between the source and the chambers plan is 2060 mm. Figure 4.9a 245 provides a side view of the setup in the xz plane while Figure 4.9b shows a top view 246 in the yz plane.	4-11
247	4.10	RE-4-2-BARC-161 chamber is inside the tent as described in Figure 4.9. In the top 248 right, the two scintillators used as trigger can be seen. This trigger system has an 249 inclination of 10° relative to horizontal and is placed above half-partition B2 of the 250 RPCs. PMT electronics are shielded thanks to lead blocks placed in order to protect 251 them without stopping photons from going through the scintillators and the chamber.	4-12
252	4.11	Hit distributions over all 3 partitions of RE-4-2-BARC-161 chamber is showed on 253 these plots. Top, middle and bottom figures respectively correspond to partitions A, 254 B, and C. These plots show that some events still occur in other half-partitions than 255 B2, which corresponds to strips 49 to 64, in front of which the trigger is placed, con- 256 tributing to the inefficiency of detection of cosmic muons. In the case of partitions 257 A and C, the very low amount of data can be interpreted as noise. On the other hand, 258 it is clear that a little portion of muons reach the half-partition B1, corresponding to 259 strips 33 to 48.	4-13

260	4.12 Results are derived from data taken on half-partition B2 only. On the 18 th of June 261 data has been taken on chamber RE-2-BARC-161 at building 904 (Prevessin 262 Site) with cosmic muons providing us a reference efficiency plateau of $(97.54 \pm$ 263 $0.15)\%$ represented by a black curve. A similar measurement has been done at GIF 264 on the 21 st of July with the same chamber giving a plateau of $(78.52 \pm 0.94)\%$ 265 represented by a red curve.	4-14
266	4.13 Representation of the layout used for the simulations of the test setup. The RPC is 267 represented as a yellow trapezoid while the two scintillators as blue cuboids looking 268 at the sky. A green plane corresponds to the muon generation plane within the sim- 269 ulation. Figure 4.9a shows a global view of the simulated setup. Figure 4.9b shows 270 a zommed view that allows to see the 2 scintillators as well as the full RPC plane.	4-15
271	4.14 γ flux $F(D)$ is plot using values from table 4.1. As expected, the plot shows similar 272 attenuation behaviours with increasing distance for each absorption factors.	4-18
273	4.15 Figure 4.15a shows the linear approximation fit done via formulae 4.7 on data from 274 table 4.2. Figure 4.15b shows a comparison of this model with the simulated flux 275 using a and b given in figure 4.15a in formulae 4.4 and the reference value $D_0 =$ 276 50cm and the associated flux for each absorption factor F_0^{ABS} from table 4.1	4-20
277	4.16 Dose measurements has been done in a plane corresponding to the tents front side. 278 This plan is 1900 mm away from the source. As explained in the first chapter, a 279 lens-shaped lead filter provides a uniform photon flux in the vertical plan orthogonal 280 to the beam direction. If the second line of measured fluxes is not taken into account 281 because of lower values due to experimental equipments in the way between the 282 source and the tent, the uniformity of the flux is well showed by the results.	4-22
283	4.17	4-23
284	4.18 Evolution of the maximum efficiency for RE2 (4.18a) and RE4 (4.18b) chambers 285 with increasing extrapolated γ rate per unit area at working point. Both irradiated 286 (blue) and non irradiated (red) chambers are shown.	4-25
287	4.19 Evolution of the working point for RE2 (4.19a) and RE4 (4.19b) with increasing 288 extrapolated γ rate per unit area at working point. Both irradiated (blue) and non 289 irradiated (red) chambers are shown.	4-25
290	4.20 Evolution of the maximum efficiency at HL-LHC conditions, i.e. a background hit 291 rate per unit area of 300Hz/cm^2 , with increasing integrated charge for RE2 (4.20a) 292 and RE4 (4.20b) detectors. Both irradiated (blue) and non irradiated (red) chambers 293 are shown. The integrated charge for non irradiated detectors is recorded during test 294 beam periods and stays small with respect to the charge accumulated in irradiated 295 chambers.	4-26
296	4.21 Comparison of the efficiency sigmoid before (triangles) and after (circles) irradiation 297 for RE2 (4.21a) and RE4 (4.21b) detectors. Both irradiated (blue) and non irradiated 298 (red) chambers are shown.	4-26
299	4.22 Evolution of the Bakelite resistivity for RE2 (4.22a) and RE4 (4.22b) detectors. Both 300 irradiated (blue) and non irradiated (red) chambers are shown.	4-27
301	4.23 Evolution of the noise rate per unit area for the irradiated chamber RE2-2-BARC-9 302 only.	4-27
303	A.1 (A.1a) View of the front panel of a V1190A TDC module [58]. (A.1b) View of the 304 front panel of a V1718 Bridge module [59]. (A.1c) View of the front panel of a 6U 305 6021 VME crate [60].	A-3
306	A.2 Module V1190A <i>Trigger Matching Mode</i> timing diagram [58].	A-4

307	A.3 Structure of the ROOT output file generated by the DAQ. The 5 branches (<code>EventNumber</code> ,	A-10
308	<code>number_of_hits</code> , <code>Quality_flag</code> , <code>TDC_channel</code> and <code>TDC_TimeStamp</code>) are visible on	
309	the left panel of the ROOT browser. On the right panel is visible the histogram cor-	
310	responding to the variable <code>nHits</code> . In this specific example, there were approximately	
311	50k events recorded to measure the gamma irradiation rate on the detectors. Each	
312	event is stored as a single entry in the <code>TTree</code>	
313	A.4 The effect of the quality flag is explained by presenting the content of <code>TBranch</code>	
314	<code>number_of_hits</code> of a data file without <code>Quality_flag</code> in Figure A.4a and the con-	
315	tent of the same <code>TBranch</code> for data corresponding to a <code>Quality_flag</code> where all TDCs	
316	were labelled as <code>GOOD</code> in Figure A.4b taken with similar conditions. It can be noted	
317	that the number of entries in Figure A.4b is slightly lower then in Figure A.4a due	
318	to the excluded events.	A-12
319	A.5 Using the same data as previously showed in Figure A.4, the effect of the quality	
320	flag is explained by presenting the reconstructed hit multiplicity of a data file with-	
321	out <code>Quality_flag</code> in Figure A.5a and the reconstructed content of the same RPC	
322	partition for data corresponding to a <code>Quality_flag</code> where all TDCs were labelled as	
323	<code>GOOD</code> in Figure A.5b taken with similar conditions. The artificial high content of bin	
324	0 is completely suppressed.	A-12
325	A.6 WebDCS DAQ scan page. On this page, shifters need to choose the type of scan	
326	(Rate, Efficiency or Noise Reference scan), the gamma source configuration at the	
327	moment of data taking, the beam configuration, and the trigger mode. These in-	
328	formation will be stored in the DAQ ROOT output. Are also given the minimal	
329	measurement time and waiting time after ramping up of the detectors is over before	
330	starting the data acquisition. Then, the list of HV points to scan and the number of	
331	triggers for each run of the scan are given in the table underneath.	A-14
332	B.1 Example of expected hit time distributions in the cases of efficiency (Figure B.1a)	
333	and noise/gamma rate per unit area (Figure B.1b) measurements as extracted from	
334	the raw ROOT files. The unit along the x-axis corresponds to ns. The fact that	
335	"the" muon peak is not well defined in Figure B.1a is due to the contribution of all	
336	the RPCs being tested at the same time that don't necessarily have the same signal	
337	arrival time. Each individual peak can have an offset with the ones of other detectors.	
338	The inconsistancy in the first 100 ns of both time distributions is an artefact of the	
339	TDCs and are systematically rejected during the analysis.	B-16
340	B.2 The effect of the quality flag is explained by presenting the reconstructed hit multi-	
341	plicity of a data file without <code>Quality_flag</code> . The artificial high content of bin 0 is the	
342	effect of corrupted data.	B-19
343	B.3 Display of the masking tool page on the webDCS. The window on the left allows the	
344	shifter to edit <code>ChannelsMapping.csv</code> . To mask a channel, it only is needed to set the	
345	3rd field corresponding to the strip to mask to 0. It is not necessary for older mapping	
346	file formats to add a 1 for each strip that is not masked as the code is versatile and	
347	the default behaviour is to consider missing mask fields as active strips. The effect	
348	of the mask is directly visible for noisy channels as the corresponding bin turns red.	
349	The global effect of masking strips will be an update of the rate value showed on the	
350	histogram that will take into consideration the rejected channels.	B-24

List of Tables

351

352	3.1	Properties of the most used electrode materials for RPCs.	3-4
353	4.1	Total photon flux ($E\gamma \leq 662$ keV) with statistical error predicted considering a ^{137}Cs activity of 740 GBq at different values of the distance D to the source along the x-axis of irradiation field [55].	4-17
354	4.2	Correction factor c is computed thanks to formulae 4.5 taking as reference $D_0 = 50$ cm and the associated flux F_0^{ABS} for each absorption factor available in table 4.1.	4-19
355	4.3	The data at D_0 in 1997 is taken from [55]. In a second step, using Equations 4.8 and 4.9, the flux at D can be estimated in 1997. Then, taking into account the attenuation of the source activity, the flux at D can be estimated at the time of the tests in GIF in 2014. Finally, assuming a sensitivity of the RPC to γ $s = 2 \cdot 10^{-3}$, an estimation of the hit rate per unit area is obtained.	4-21
363	A.1	Inter-process communication cycles in between the webDCS and the DAQ through file string signals.	A-19
364			

List of Acronyms

365

366

List of Acronyms

367

368

A

369

370

371 AFL

Almost Full Level

372

373

B

374

375

376 BARC

Bhabha Atomic Research Centre

377 BLT

Block Transfer

378 BNL

Brookhaven National Laboratory

379 BR

Branching Ratio

380

381

C

382

383

384 CAEN

Costruzioni Apparecchiature Elettroniche Nucleari S.p.A.

385 CERN

European Organization for Nuclear Research

386 CFD

Constant Fraction Discriminator

387 CMS

Compact Muon Solenoid

388 CSC

Cathode Strip Chamber

389

390

D

391

392

393 DAQ

Data Acquisition

394 DCS

Detector Control Software

395 DQM

Data Quality Monitoring

396 DT

Drift Tube

397

398

F

399

400

401	FEE	Front-End Electronics
402	FEB	Front-End Board
403		
404		
405	G	
406		
407	GE-/-	Find a good description
408	GE1/1	Find a good description
409	GE2/1	Find a good description
410	GEANT	GEometry ANd Tracking - a series of software toolkit platforms developed by CERN
411		
412	GEM	Gas Electron Multiplier
413	GIF	Gamma Irradiation Facility
414	GIF++	new Gamma Irradiation Facility
415		
416		
417	H	
418		
419	HL-LHC	High Luminosity LHC
420	HPL	High-pressure laminate
421	HV	High Voltage
422		
423		
424	I	
425		
426	iRPC	improved RPC
427	IRQ	Interrupt Request
428	ISR	Intersecting Storage Rings
429		
430		
431	L	
432		
433	LEIR	Low Energy Ion Ring
434	LEP	Large Electron-Positron
435	LHC	Large Hadron Collider
436	LS1	First Long Shutdown
437	LS3	Third Long Shutdown
438	LV	Low Voltage
439	LVDS	Low-Voltage Differential Signaling
440		
441		
442	M	
443		
444	MC	Monte Carlo

445	MCNP	Monte Carlo N-Particle
446	ME-/	Find good description
447	ME0	Find good description
448	MRPC	Multigap RPC
449		
450		
451	N	
452		
453	NIM	Nuclear Instrumentation Module logic signals
454		
455		
456	P	
457		
458	PS	Proton Synchrotron
459	PMT	PhotoMultiplier Tube
460		
461		
462	Q	
463		
464	QCD	Quantum Chromodynamics
465	QED	Quantum Electrodynamics
466		
467		
468	R	
469		
470	RE-/	Find a good description
471	RE2/2	Find a good description
472	RE3/1	Find a good description
473	RE3/2	Find a good description
474	RE4/1	Find a good description
475	RE4/2	Find a good description
476	RE4/3	Find a good description
477	RMS	Root Mean Square
478	ROOT	a framework for data processing born at CERN
479	RPC	Resistive Plate Chamber
480		
481		
482	S	
483		
484	SC	Synchrocyclotron
485	SLAC	Stanford Linear Accelerator Center
486	SM	Standard Model
487	SPS	Super Proton Synchrotron

488

489

490

491

T

- 492 TDC Time-to-Digital Converter
493 ToF Time-of-flight

494

495

496

W

497

- 498 webDCS Web Detector Control System

1

Introduction

499

500

⁵⁰¹ **1.1 A story of High Energy Physics**

⁵⁰² **1.2 Organisation of this study**

2

503

504

Investigating the TeV scale

505 „We may regard the present state of the universe as the effect of the
506 past and the cause of the future. An intellect which at any given mo-
507 ment knew all of the forces that animate nature and the mutual posi-
508 tions of the beings that compose it, if this intellect were vast enough
509 to submit the data to analysis, could condense into a single formula
510 the movement of the greatest bodies of the universe and that of the
511 lightest atom; for such an intellect nothing could be uncertain and
512 the future just like the past would be present before its eyes.”

513

514 - Pierre Simon de Laplace, *A Philosophical Essay on Probabilities*, 1814

515 Throughout history, physics experiment became more and more powerful in order to investigate
516 finer details of nature and helped understanding the elementary blocks of matter and the fundamental
517 interactions that bond them in the microscopic world. Nowadays, the Standard Model (SM) of
518 particle physics is the most accurate theory designed to explain the behaviour of particles and was
519 able to make very precise predictions that are constantly verified, although some hints of new physics
520 are visible as bricks are still missing to have a global comprehension of the Universe.

521 To highlight the limits of the SM and test the different alternative theories, ever more powerful
522 machines are needed. This is in this context that the Large Hadron Collider (LHC) has been thought
523 and built to accelerate and collide particles at energies exceeding anything that had been done before.
524 Higher collision energies and high pile-up imply the use of enormous detectors to measure the
525 properties of the interaction products. The Compact Muon Solenoid (CMS) is a multipurpose ex-
526 periment that have been designed to study the proton-proton collisions of the LHC and give answers
527 on various high energy physics scenari. Nevertheless, the luminosity delivered by the collider will
528 in the future be increased to levels beyond the original plans to improve its discovery potential giv-
529 ing no choice to experiments such as CMS to upgrade their technologies to cope with the increased
530 radiation levels and detection rates.

531 **2.1 The Standard Model of Particle Physics**

532 In this early 21st century it is now widely accepted that matter is made of elementary blocks referred
533 to as *elementary particles*. The physics theory that classifies and describes the best the behaviour
534 and interaction of such elementary particles is the so called Standard Model that formalizes 3 of
535 the 4 fundamental interactions (electromagnetic, weak and strong interactions). It's development
536 took place during the 20th century thanks to a strong collaboration in between the theoretical and
537 experimental physicists.

538 **2.1.1 A history of particle physics**

539 The idea that nature is composed of elementary bricks, called *atomism*, is not contemporary as it
540 was already discussed by Indian or Greek philosophers during antiquity. In Greece, atomism has
541 been rejected by Aristotelianism as the existance of *atoms* would imply the existance of a void that
542 would violate the physical principles of Aristotle philosophy. Aristotelianism has been considered
543 as a reference in the european area until the 15th century and the italian *Rinascimento* where antic
544 text and history started to be more deeply studied. The re-discovery of Platon's philosophy would
545 allow to open the door to alternative theories and give a new approach to natural sciences where
546 experimentation would become central. A new era of knowledge was starting. By the begining of
547 the 17th century, atomism was re-discovered by philosophers and the very first attempt to estimate
548 an *atom* size would be provided by Magnetus in 1646. Although his *atoms* correspond to what would
549 nowadays be called *molecules*, Magnetus achieved feats by calculating that the number of molecules
550 in a grain of incense would be of the order of 10^{18} simply by considering the time necessary to smell
551 it everywhere in a large church after the stick was lit on. It is now known that this number only falls
552 short by 1 order of magnitude.

553 An alternative philosophy to atomism popularized by Descartes was corpuscularianism. Built on
554 ever divisible corpuscles, contrary to atoms, it's principles would be mainly used by alchemists like
555 Newton who would later develop a corpuscular theory of light. Boyle would combine together ideas
556 of both atomism or corpuscularianism leading to mechanical philosophy. The 18th century have

seen the development of engineering providing philosophical thought experiments with repeatable demonstration and a new point of view to explain the composition of matter and Lavoisier would greatly contribute to chemistry and atomism by publishing in 1789 a list of 33 chemical elements corresponding to what is now called *atoms*. In the early 19th century Dalton would summarize the knowledge on composition of matter and Fraunhofer would invent the spectrometer and discover the spectral lines. The rise of atomic physics, chemistry and mathematical formalism would unravel the different atomic elements and ultimately, the 20th century would see the very first sub-atomic particles.

Discovery of the inner structure of the atom and of the neutrino

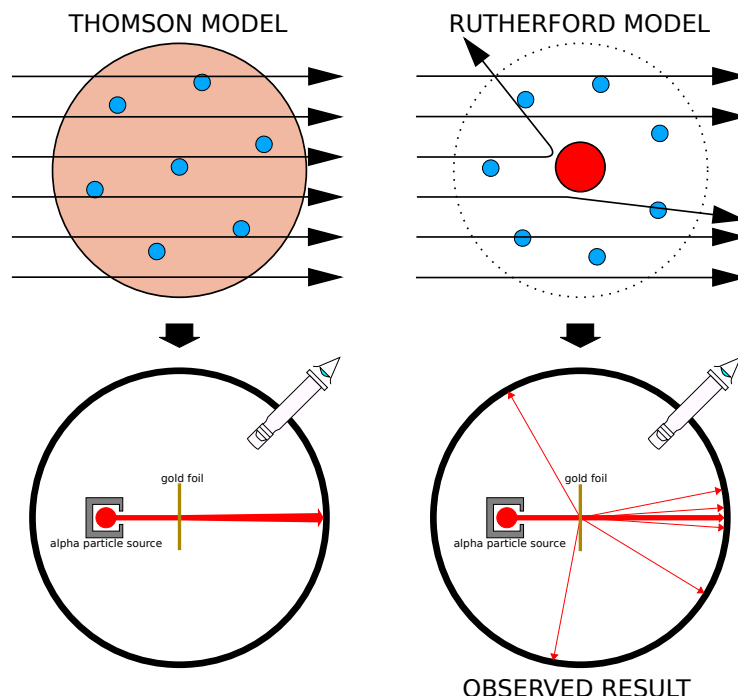


Figure 2.1: Through the gold foil experiment Rutherford could show that most of the mass of atoms was contained in a positively charged nucleus and could then propose a more accurate atomic model than that of Thomson.

The negative *electron* would be the first to be discovered in 1897 by Thomson after 3 decades of research on cathode rays by proving that the electrification observed in an electroscope, as reported by Perrin, was due to the rays themselves and that they had to be composed of electrically charged particles. In 1900, Becquerel would show the *beta rays* emitted by radium had the same charge over mass ratio than what measured by Thomson for cathode rays, pointing to electrons as a constituent of atoms. In 1907, Rutherford and Royds showed that *alpha* particles, once captured in a tube and subjected to an electric spark causing an electron avalanche, where helium ions as they could combine with 2 electrons to form a ${}^4\text{He}$. This discovery was directly followed by the constraint of the atom structure in 1909 through the gold foil experiment in which the deflection angle of alpha particles fired at a very thin gold foil was measured and highlighted atoms where mainly empty with

576 nearly all its mass contained into a tiny positively charged *nucleus*. With these two observations,
 577 he could formulate the Rutherford model of the atom in 1911, shown together with the Thomson
 578 plum pudding model in Figure 2.1. The link in between atomic number and number of positive and
 579 negative charges contained into the atoms would fast be understood and the different kind of element
 580 transmutation appeared to be purely nuclear processes making clear that the electromagnetic nature
 581 of chemical transformation could not possibly change nuclei. Thus a new branch in physics appeared
 582 to study nuclei exclusively: the nuclear physics.

583 Moreover, in 1913 quantum physics would be introduced into the atomic model by Bohr based
 584 on the assumptions of Plank to explain spectral lines, and other observed quantum effects. The same
 585 year, Moseley would confirm Borh's model and Debye would extend it by introducing elliptical
 586 orbits.

587 By studying alpha emission and the product of their interaction with nitrogen gas, Rutherford
 588 reported in 1919 the very first nuclear reaction leading to the discovery that the hydrogen nucleus was
 589 composed of a single positively charged particle that was later baptised *proton*. This idea came from
 590 1815 Prout's hypothesis proposing that all atoms are composed of "protyles" (i.e. hydrogen atoms).
 591 By using scintillation detectors, Rutherford could highlight typical hydrogen nuclei signature and
 592 understand that the impact of alpha particles with nitrogen would knock out an hydrogen nucleus
 593 and produce an oxygen 17, as explicated in Formula 2.1 and would then postulate that protons are
 594 building bricks of all elements.



595 With this assumption and the discovery of isotopes together with Aston, elements with identical
 596 atomic number but different masses, Rutherford would propose that all elements' nuclei but hydrogen's are composed of both charged particles, protons, and of chargeless particles, which he called
 597 *neutrons*, and that these neutral particles would help maintaining nuclei as one, as charged protons
 598 were likely to electrostatically repulse each other, and introduced the idea of a new force, a *nuclear*
 599 force. Though the first idea concerning neutrons was a bond state of protons and electrons as it was
 600 known that the beta decay, emitting electrons, was taking place in the nucleus, it was then showed
 601 that such a model would hardly be possible due to Heisenberg's uncertainty principle and by the
 602 recently measured *spin* of both protons and electrons. The spin, discovered through the study of
 603 the emission spectrum of alkali metals, would be understood as a "two-valued quantum degree of
 604 freedom" and formalized by Pauli and extended by Dirac, to take the relativist case into account.
 605 Measured to be $\frac{1}{2}\hbar$ for both, it was impossible to arrange an odd number of half integer spins and
 606 obtain a global nucleus spin that would be integer. Finally, in 1932, following the discovery of a new
 607 neutral radiation, Chadwick could discover the neutron as an uncharged particle with a mass similar
 608 to that of the proton whose half integer spin would reveal to be the solution to explain the nuclear
 609 spin.

610 Thanks to the neutron, Fermi could explain in 1934 the beta radiations through the beta decay
 611 process in which the neutron decays into a proton by emitting an electron. Though the missing
 612 energy observed during this process triggered a huge debate about the apparent non conservation of
 613 energy, momentum and spin of the process, Fermi, as Pauli before him, proposed that the missing
 614 energy was due to a neutral not yet discovered particle that would then be baptised *neutrino*. The im-
 615 possibility to detect such a particle would leave some members of the scientific community sceptical,
 616 but hints of energy conservation and of the existence of the neutrino were provided by measuring the
 617 energy spectrum of electrons emitted through beta decay, as there was a strict limit on their energy.

619 It's only 30 years later in 1953 that it would be discovered by the team of Cowan and Reines using
 620 the principle of inverse beta decay described through Formula 2.2. The experiment consisted in plac-
 621 ing water tanks sandwiched in between liquid scintillators near a nuclear reactor with an estimated
 622 neutrino flux of $5 \times 10^{13} \text{ s}^{-1} \text{ cm}^{-2}$. However, in order to explain the absence of come reactions in
 623 the experiment of Cowan and Reines, and constraint the beta decay theory of Fermi and extend it to
 624 the case of the muon, Konopinski and Mahmoud proposed in 1953 that the muon decay would eject
 625 a particle similar to the neutrino and thus predicted the existence of a muon neutrino that would be
 626 different than the one involved in the beta decay, related to the electron. With this, the idea of lepton
 627 number would arise. The muon would successfully be detected in 1962 by Lederman, Schwartz and
 628 Steinberger.

$$\bar{\nu} + p \rightarrow n + e^+ \quad (2.2)$$

629 **Development of the Quantum Electrodynamics, of the Weak interaction and the Electroweak
 630 unification**

631 Historically, the development of the quantum theory revolved around the question of emission and
 632 absorption of discrete amount of energy through light. Einstein used the initial intuition of Plank
 633 about the black-body radiation to develop in 1905 a model to explain the photoelectric effect in
 634 which light was described by discrete quanta now called *photons*. For this model, Einstein introduced
 635 the concept of wave-particle duality as classical theory was not able to describe the phenomenon.
 636 With the new understanding of atoms and of their structure, classical theories also proved unable
 637 to explain atoms stability. Indeed, using classical mechanics, electrons orbiting around a nucleus
 638 should radiate an energy proportionnal to their angular momentum and thus loose energy through
 639 time and the spectrum of energy emission should then be continuous, but it was known since the
 640 19th century and the discovery of spectral lines that the emission spectrum of material was discrete.

641 This was Bohr who first suggested that a quantum description of the atom was necessary in 1913.
 642 Using the correspondence principle stating that at large enough numbers the quantum calculations
 643 should give the same results than the classical theory, he proposed the very first quantum model
 644 of the hydrogen atom explaining the line spectrum by introducing the principal quantum number
 645 n describing the electron shell. This model would then be improved by Sommerfeld that would
 646 quantize the z-component of the angular momentum, leading to the second and third quantum
 647 numbers, or azimuthal and magnetic quantum number, l and m defining for the second the orbital
 648 angular momentum of the electrons on their shells and thus, the shape of the orbital, and for the third
 649 the available orbital on the subshell for each electron. Nevertheless, although the model was not only
 650 limited to spherical orbitals anymore, making the atom more realistic, the Zeeman effect couldn't be
 651 completely explained by just using n , l and m . A solution would be brought after the discovery of
 652 Pauli in 1924, as Uhlenbeck, Goudsmit, and Krong proposed in 1925 the idea of intrinsic rotation
 653 of the electron, introducing a new angular momentum vector associated to the particle itself, and
 654 not to the orbital, and associated to a new quantic number s , the *spin* projection quantum number
 655 explaining the lift of degeneracy to an even number of energy levels.

656 The introduction of the *spin* happened 1 year after another attempt of improvement of the theory
 657 was made by De Broglie in his PhD thesis. The original formulation of the quantum theory only
 658 considered photons as energy quanta behaving as both waves and particles. De Broglie proposed
 659 that all matter are described by waves and that their momentum is proportional to the oscillation of
 660 quantized electromagnetic field oscillators. This interpretation was able to reproduce the previous

661 version of the quantum energy levels by showing that the quantum condition involves an integer
 662 multiple of 2π , as shown by Formula 2.3.

$$p = \hbar k \Leftrightarrow \int pdx = \hbar \int kdx = 2\pi\hbar n \quad (2.3)$$

663 Although the intuition of De Broglie about the wave-particle duality of all matter, his interpretation
 664 was semiclassical and it's in 1926 that the first fully quantum mechanical wave-equation would
 665 be introduced by Schrödinger to describe electron-like particles, reproducing the previous semiclassi-
 666 cal formulation without inconsistencies. This complexe equation describes the evolution of the
 667 wave function Ψ of the quantum system, defined by it's position vector \mathbf{r} and time t as an energy
 668 conservation law, in which the hamiltonian of the system \hat{H} is explicit, by solving the Equation 2.4.

$$i\hbar \frac{\partial}{\partial t} |\Psi(\mathbf{r}, t)\rangle = \hat{H} |\Psi(\mathbf{r}, t)\rangle \quad (2.4)$$

669 In 1927, Dirac would go further in his paper about emission and absorption of radiation by
 670 proposing a quantization not only of the physical process at play but also of the electromagnetic
 671 field, leading to the first formulation of *Quantum Electrodynamics (QED)*.

672 Development of the Higgs mechanism

673 Development of the quark model and Quantum Chromodynamics

674 To explain the nuclear force that holds *nucleons* (protons and neutrons) together, Yukawa theoreti-
 675 cally proposed in 1934 the existence of a force carrier called *meson* due to it's predicted mass in
 676 the range in between the electron and nucleon masses. Discovered in 1936 by Anderson and Ned-
 677 dermeyer, and confirmed using bubble chambers in 1937 by Street and Stevenson, a first meson
 678 candidate was observed in the decay products of cosmic rays. Assuming it had the same electric
 679 charge than electrons and protons, this particle was observed to have a curvature due to magnetic
 680 field that was sharper than protons but smoother than electrons resulting in a mass in between that
 681 of electrons and protons. But its properties were not compatible with Yukawa's theory, which was
 682 emphasized by the discovery of a new candidate in 1947, again in cosmic ray products using photo-
 683 graphic emulsions.

684 This new candidate, although it had a similar mass than the already believed *meson*, would rather
 685 decay into it. For distinction, the first candidate would then be renamed "mu meson" when the second
 686 would be the "pi meson". The mu meson was behaving like a heavy electron and didn't participate
 687 in the strong interaction whereas the pion was believed to be the carrier of the nuclear interaction.
 688 This lead to classify the mu in a new category of particles called *leptons* together with the electron
 689 that shared similar properties and the neutrino, and be renamed *muon*. The pi meson was finally
 690 found to be a triplet of particles: a positively charged, a negatively charged, and a neutral particle.
 691 The neutral pi meson has been more difficult to identify as it wouldn't leave tracks on emulsions nor
 692 on bubble chambers and needed to be studied via it's decay products. It was ultimately identified in
 693 University of California's cyclotron in 1950 through the observation of its decay into 2 photons.

694 Also discovered in 1947 but in cloud chamber photographs, the *K meson* as also been an im-
 695 portant step towards the establishment of the Standard Model. A triplet of particle, 2 charged and a
 696 neutral, with a mass roughly half that of a proton, were reported. These particles were baptised *K*
 697 *meson* in contrast to the "light" *pi* and *mu* "L-mesons". The particularity of the *K* were there very
 698 slow decays with a typical lifetime of the order of 10^{-10} s much greater than the 10^{-23} s of *pi*-proton

699 reactions. The concept of *strangeness*, a new quantum number was then introduced by Pais as an
700 attempt to explain this phenomenon as *strange* particles appeared as a pair production of a strange
701 and anti-strange particle.

702 With the development of synchrotrons, the particle *zoo* would grow to several dozens during the
703 1950s as higher energies were reachable through acceleration. In 1961, a first classification system,
704 called Eightfold Way, was proposed by Gell-Mann and finding its roots in the Gell-Mann–Nishijima
705 formula, which relates the electric charge Q , the third component of the isospin I_3 , the *baryon*
706 number B and the strangeness S , as explicitated in Formula 2.5. The isospin was a quantum number
707 introduced in 1932 to explain symmetries of the newly discovered neutron using representation
708 theory of SU(2). The baryon number, was introduced by Nishijima as a quantum number for baryons,
709 i.e. particles of the same family as nucleons. The mesons were classified in an octet and baryons of
710 spin $\pm \frac{1}{2}$ and $\pm \frac{3}{2}$ were respectively classified into an octet and a decuplet, as shown in Figure 2.2. To
711 complete the baryon decuplet, Gell-Mann predicted the existence of baryon Ω^- which would later
712 be discovered in 1964.

$$Q = I_3 + \frac{1}{2}(B + S) \quad (2.5)$$

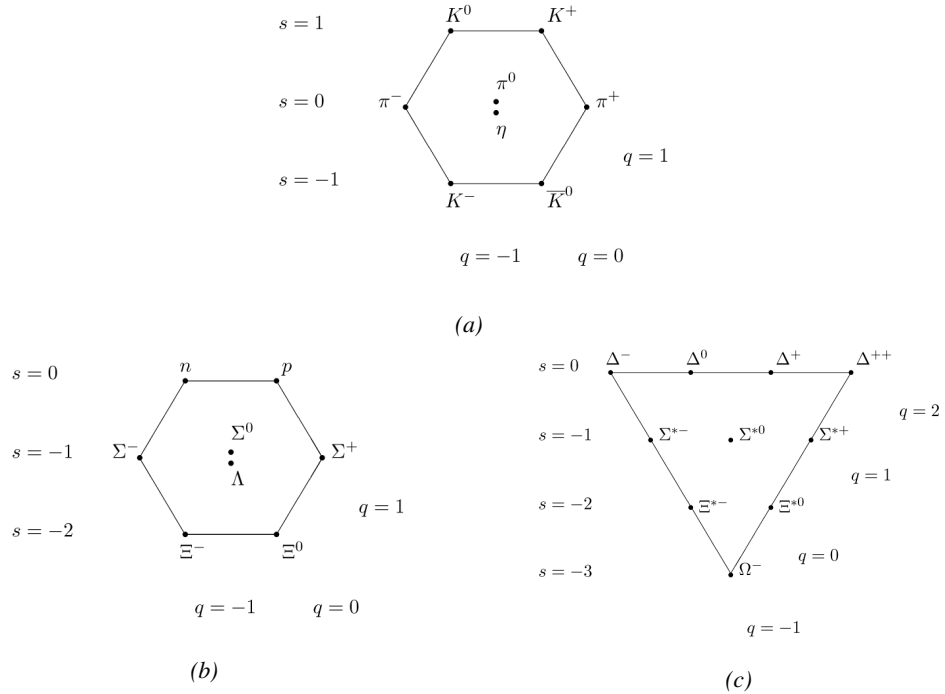


Figure 2.2: Figure 2.2a: Meson octet. Figure 2.2b: Baryon octet. Figure 2.2c: Baryon decuplet.

713 Strong of this classification using an SU(3) flavor symmetry, Gell-Mann, and independently
714 Zweig, would propose a full theoretical model in which *hadrons* (strongly interacting particles, i.e.
715 mesons and baryons) were not elementary particles anymore. They would rather be composed with
716 3 flavors of particles called *quarks* and there anti-particles. The 3 flavors were called *up*, *down* and
717 *strange*. *Up* and *down* would be used to explain the nucleons and non-strange mesons, while *strange*

would come into the composition of hadrons showing strangeness. *Up* and *down* flavors would be discovered in 1968 thanks to the deep inelastic scattering experiments conducted at the Stanford Linear Accelerator Center (SLAC), and *strange* could only be indirectly validated even though it provided a robust explanation to *kaon* (K) and *pion* (π). However, in the decade following the Gell-Mann-Zweig quark model proposition, several improvements to the model were brought, first by Glashow and Bjorken the same year that predicted the existence of a fourth quark flavor, the *charm*, that would equalize the then known number of quarks and leptons and finally in 1973 by Kobayashi and Maskawa that would increase the number of quarks to 6 to explain the experimental observation of CP violation. These two quarks were referred to as *top* and *bottom* for the first time in 1975. It's only after these additions to the quark model that finally the *charm* was discovered in 1974 at both SLAC and Brookhaven National Laboratory (BNL). A meson where the *charm* was bound with an *anti-charm*, called J/ψ , would help convince the physics community of the validity of the model. The *top* was discovered soon after in 1977 in Fermilab and indicate the existence of the *bottom* that would resist discovery until Fermilab's experiments CDF and D \emptyset in 1995 due to its very large mass and the energy needed to produce it.

As remarked by Struminsky, the original quark model proposal composed of 3 quarks should possess an additional quantum number due to mesons such as Ω^- or Δ^{++} . Indeed, these mesons are composed of 3 identical quarks, respectively 3 *strange* and *up* quark, with parallel spins, which should be forbidden by the exclusion principle. Independently, Greenberg and Han-Nambu proposed an additional SU(3) degree of freedom possessed by the quarks, that would later be referred to as *color charge gauge*, that could interact through *gluons*, the gauge boson octet corresponding to this degree of freedom. Nevertheless, as observing free quarks proved to be impossible, two visions of the quarks were argued mainly due to the failures to observe these particles free to prove their existence. On one side, Gell-Mann proposed to see quarks as mathematical construct instead of real particles, as they are always confined, implying that quantum field theory would not describe entirely the strong interaction. Opposed to this vision, Feynman on the contrary argued that quarks were real particles, that he would call *partons*, that should be described as all other particles by a distribution of position and momentum. The implications of quarks as point-like particles would be verified at SLAC and the concept of *color* would be added to the quark model in 1973 by Fritzsch and Leutwyler together with Gell-Mann to propose a description of the strong interaction through the theory of Quantum Chromodynamics (QCD). The discovery the same year of asymptotic freedom within the QCD by Gross, Politzer and Wilczek, allowed for very precise predictions thanks to the perturbation theory. Nowadays, the confinement of quarks is studied in experiments such as ALICE, through exploration of the quark-gluon plasma.

2.1.2 Construction and test of the model [TO SEE IF KEPT - MAYBE TOO COMPLEX]

$$\mathcal{L}_{QCD} = \bar{\psi}_i (i(\gamma^\mu D_\mu)_{ij} - m\delta_{ij}) \psi_j - \frac{1}{4} G_{\mu\nu}^a G_a^{\mu\nu} \quad (2.6)$$

The QCD Lagrangian is given in Formula 2.6, where $\psi_i(x)$ is the quark field in the fundamental representation of the SU(3) gauge group, D_μ is the gauge covariant derivative, the γ^μ are Dirac matrices. $G_{\mu\nu}^a$ represents the gauge invariant gluon field strength tensor, analogous to the electromagnetic field strength tensor, $F^{\mu\nu}$, in QED and is described by Formula 2.7.

$$G_{\mu\nu}^a = \partial_\mu A_\nu^a - \partial_\nu A_\mu^a + g f^{abc} A_\mu^b A_\nu^c \quad (2.7)$$

⁷⁵⁸ $A_\mu^a(x)$ are the gluon fields, in the adjoint representation of the SU(3) gauge group, and f_{abc} are
⁷⁵⁹ the structure constants of SU(3). Finally, the variables m and g correspond to the quark mass and
⁷⁶⁰ coupling of the theory, respectively, which are subject to renormalization.

⁷⁶¹ 2.1.3 Investigating the TeV scale

⁷⁶² 2.2 The Large Hadron Collider & the Compact Muon Solenoid

⁷⁶³ Throughout its history, CERN has played a leading role in high energy particle physics. Large re-
⁷⁶⁴ gional facilities such as CERN were thought after the second world war in an attempt to increase
⁷⁶⁵ international scientific collaboration and allows scientists to share the forever increasing costs of
⁷⁶⁶ experiment facilties required due to the need for increasing the energy in the center of mass to
⁷⁶⁷ deeper probe matter. The construction of the first accelerators at the end of the 50s, the Synchro-
⁷⁶⁸ cyclotron (SC) and the Proton Synchrotron (PS), was directly followed by the first observation of
⁷⁶⁹ antinuclei in 1965 [1]. Strong from the experience of the Intersecting Storage Rings (ISR), the very
⁷⁷⁰ first proton-proton collider that showed hints that protons are not elementary particles, the Super
⁷⁷¹ Proton Synchrotron (SPS) was built in the 70s to investigate the structure of protons, the preference
⁷⁷² for matter over antimatter, the state of matter in the early universe or exotic particles, and lead to
⁷⁷³ the discovery in 1983 of the W and Z bosons [2–5]. These newly discovered particles and the elec-
⁷⁷⁴ troweak interaction would then be studied in details by the Large Electron-Positron (LEP) collider
⁷⁷⁵ that will help to prove in 1989 that there only are three generations of elementary particles [6]. The
⁷⁷⁶ LEP would then be dismantled in 2000 to allow for the LHC to be constructed in the existing tunnel.

⁷⁷⁷ 2.2.1 LHC, the most powerful particle accelerator

⁷⁷⁸ The LHC has always been considered as an option to the future of CERN. At the moment of the
⁷⁷⁹ construction of the LEP beneath the border between France and Switzerland, the tunnel was built in
⁷⁸⁰ order to accomodate what would be a Large Hadron Collider with a dipole field of 10 T and a beam
⁷⁸¹ energy in between 8 and 9 TeV [7] directly followed in 1985 with the creation of a 'Working Group
⁷⁸² on the Scientific and Technological Future of CERN' to investigate such a collider [8]. The decision
⁷⁸³ was finally taken almost 10 years later, in 1994, to construct the LHC in the LEP tunnel [9] and the
⁷⁸⁴ approval of the 4 main experiments that would take place at the 4 interaction points would come in
⁷⁸⁵ 1997 [10] and 1998 [11]:

- ⁷⁸⁶ • ALICE [12] has been designed in the purpose of studying quark-gluon plasma that is believed
⁷⁸⁷ to have been a state of matter that existed in the very first moment of the universe.
- ⁷⁸⁸ • ATLAS [13] and CMS [14] are general purpose experiments that have been designed with
⁷⁸⁹ the goal of continuing the exploration of the Standard Model and investigate new physics.
- ⁷⁹⁰ • LHCb [15] has been designed to investigate the preference of matter over antimatter in the
⁷⁹¹ universe through the CP violation.

⁷⁹² These large scale experiments, as well as the full CERN accelerator complex, are displayed on
⁷⁹³ Figure 2.3.

CERN's Accelerator Complex

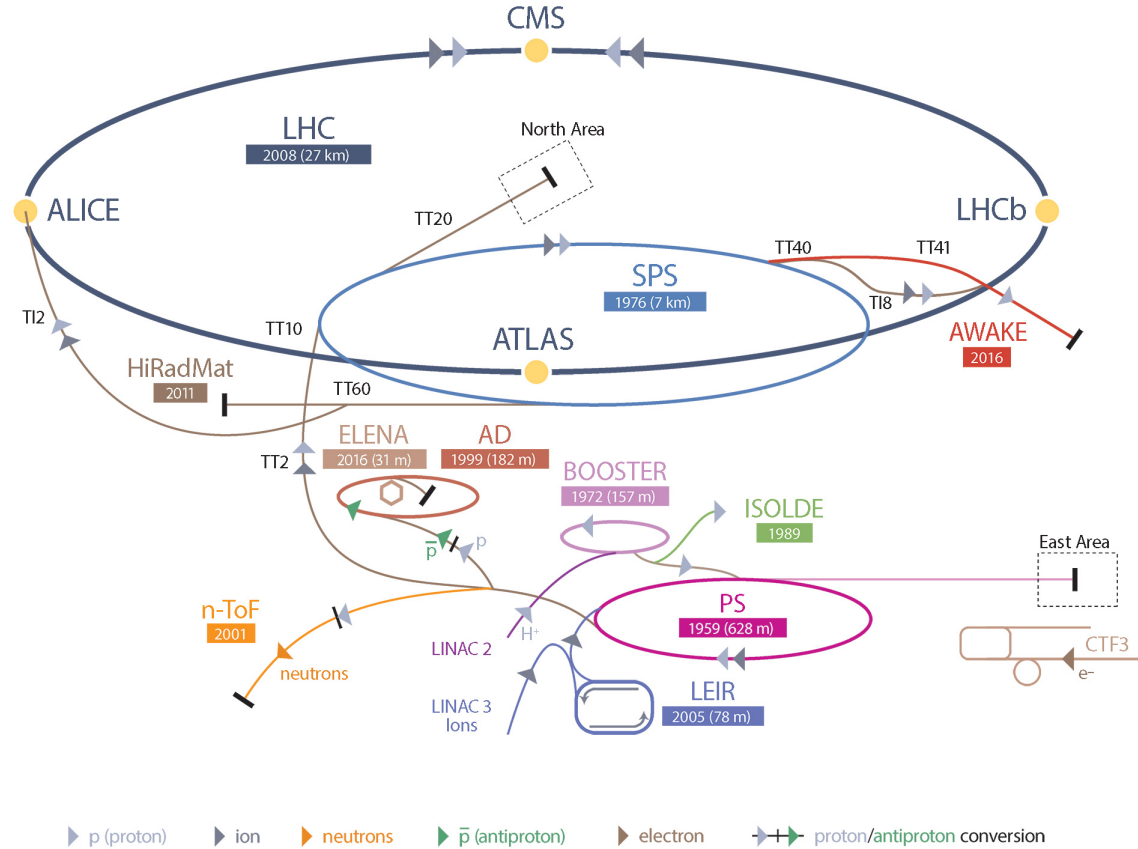


Figure 2.3: CERN accelerator complex.

The LHC is a 27 km long hadron collider and the most powerful accelerator used for particle physics since 2008 [16]. The LHC was originally designed to collide protons at a center-of-mass energy of 14 TeV and luminosity of $10^{34} \text{ cm}^{-2}\text{s}^{-1}$, as well as Pb ions at a center-of-mass energy of 2.8 TeV/A with a peak luminosity of $10^{27} \text{ cm}^{-2}\text{s}^{-1}$. Run 1 of LHC, when the center-of-mass energy only was half of the nominal LHC energy, was enough for both CMS and ATLAS to discover the Higgs boson [17] and for LHCb to discover pentaquarks [18] and confirm the existence of tetraquarks [19]. Nevertheless, after the Third Long Shutdown (LS3) (2024-2026), the accelerator will be in the so called High Luminosity LHC (HL-LHC) configuration [20], increasing its instantaneous luminosity to $10^{35} \text{ cm}^{-2}\text{s}^{-1}$ for pp collisions and to $4.5 \times 10^{27} \text{ cm}^{-2}\text{s}^{-1}$, boosting the discovery potential of the LHC.

2.2.1.1 Particle acceleration

The LHC is the last of a long series of accelerating devices. Before being accelerated by the LHC, the particles need to pass through different acceleration stages. All these acceleration stages are

807 visible on Figure 2.3 and pictures of the accelerators are showed in Figure 2.4.

808

809 The story of accelerated protons at CERN starts with a bottle of hydrogen gas injected into the
810 source chamber of the linear particle accelerator *LINAC 2* in which a strong electric field strips the
811 electron off the hygrogen molecules only to keep their nuclei, the protons. The cylindrical conductors,
812 alternatively positively or negatively charged by radiofrequency cavities, accelerate protons by
813 pushing them from behing and pulling them from the front and ultimately give them an energy of
814 50 MeV, increasing their mass by 5% in the process.

815

816 When exiting the LINAC 2, the protons are divided into 4 bunches and injected into the 4 su-
817 perimposed synchrotron rings of the *Booster* where they are then accelerated to reach an energy of
818 1.4 GeV before being injected into the *PS*. Before the Booster was operational in 1972, the protons
819 were directly injected into the PS from the LINAC 2 but the low injection energy limited the amount
820 of protons that could be accelerated at once by the PS. With the Booster, the PS accepts approxi-
821 mately 100 times more particles.

822

823 The 4 proton bunches are thus sent as one to the PS where their energy eventually reaches
824 26 GeV. Since the 70s, the main goal of this 628 m circumference synchrotron has been to sup-
825 ply other machines with accelerated particles. Nowadays, not only the PS accelerates protons, it also
826 accelerates heavy ions from the *Low Energy Ion Ring (LEIR)*. Indeed, the LHC experiments are not
827 only designed to study *pp*-collisions but also *Pb*-collisions. Lead is first injected into the dedicated
828 linear collider *LINAC 3*, that accelerate the ions using the same principle than LINAC 2. Electrons
829 are striped off the lead ions all along the acceleration process and eventually, only bare nuclei are
830 injected in the LEIR whose goal is to transform the long ion pulses received into short dense bunches
831 for LHC. Ions injected and stored in the PS were aceelerated by the LEIR from 4.2 MeV to 72 MeV.

832

833 Directly following the PS, is finally the last acceleration stage before the LHC, the 7 km long
834 *SPS*. The SPS accelerates the protons to 450 GeV and inject proton in both LHC accelerator rings
835 that will increase their energy up to 7 TeV. When the LHC runs with heavy lead ions for ALICE
836 and LHCb, ions are injected and accelerated to reach the energy of 2.8 TeV/A.

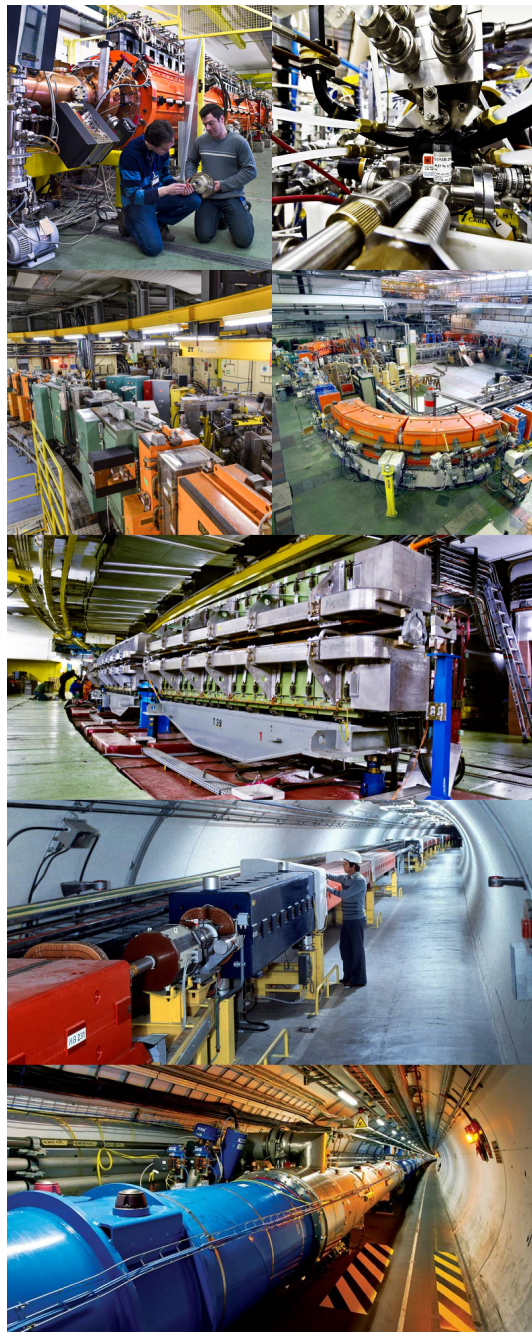


Figure 2.4: Pictures of the different accelerators. From top to bottom: first the LINAC 2 and the Pb source of LINAC 3. Then the Booster and the LEIR. Finally, the PS, the SPS and the LHC.

837 The LHC beams are not continuous and are rather organised in bunches of particles. When in pp -
 838 collision mode, the beams are composed of 2808 bunches of 1.15×10^{11} protons separated by 25 ns.
 839 When in Pb collision mode, the 592 Pb bunches are on the contrary composed of 2.2×10^8 ions
 840 separated by 100 ns. The two parallel proton beams of the LHC are contained in a single twin-

bore magnet due to the space restriction in the LEP tunnel. Indeed, building 2 completely separate accelerator rings next to each other was impossible. The dipoles of the 1232 twin-bore magnets are showed in Figure 2.5 alongside the magnetic field generated along the dipole section to accelerate the particles. The dipoles generate a nominal field of 8.33 T, needed to give protons and lead nucleons their nominal energy. Some 392 quadrupoles, presented in Figure 2.6, are also used to focus the beams, as well as other multipoles to correct smaller imperfections.

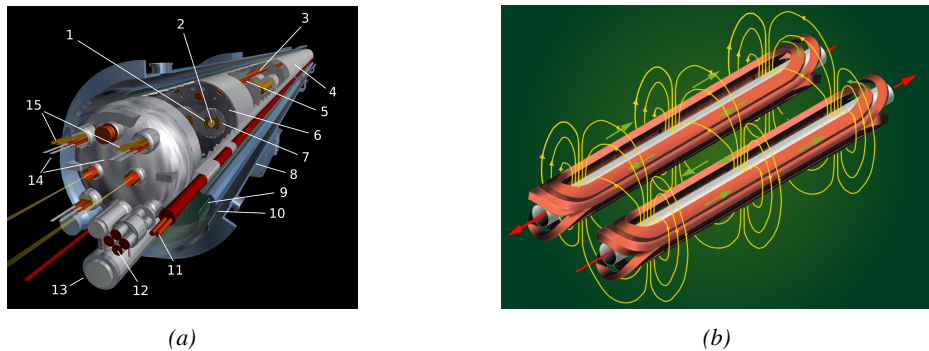


Figure 2.5: Figure 2.5a: schematics of the LHC cryodipoles. 1: Superconducting Coils, 2: Beam pipe, 3: Heat exchanger Pipe, 4: Helium-II Vessel, 5: Superconducting Bus-bar, 6: Iron Yoke, 7: Non-Magnetic Collars, 8: Vacuum Vessel, 9: Radiation Screen, 10: Thermal Shield, 11: Auxiliary Bus-bar Tube, 12: Instrumentation Feed Throughs, 13: Protection Diode, 14: Quadrupole Bus-bars, 15: Spool Piece Bus-bars. Figure 2.5b: magnetic field and resulting motion force applied on the beam particles.

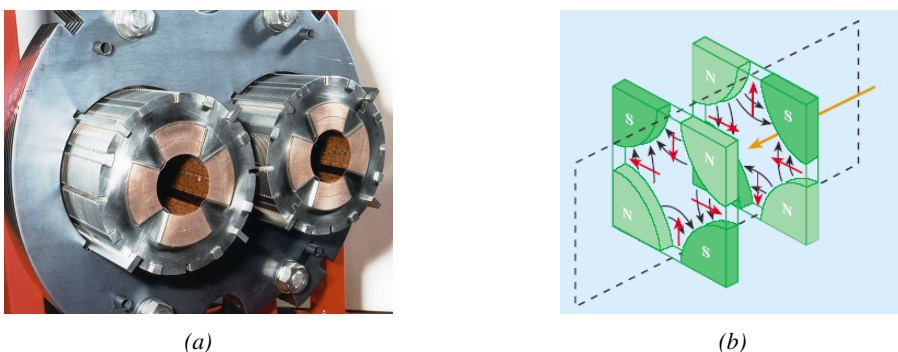


Figure 2.6: Figure 2.6a: picture of the LHC quadrupoles. Figure 2.6b: magnetic fields and resulting focussing force applied on the beam by 2 consecutive quadrupoles.

847 2.2.1.2 LHC discoveries and LHC physics program

848 The very first proton beam successfully circulated in the LHC in September 2008 directly followed
849 by an incident leading to mechanical damage that would delay the LHC program for a year until
850 November 2009.

851 **2.2.1.3 High Luminosity LHC**

852 **2.2.2 CMS, a multipurpose experiment**

853 **2.3 Muon Phase-II Upgrade**

854 After the more than two years lasting First Long Shutdown (LS1), the Large Hadron Collider (LHC)
 855 delivered its very first Run-II proton-proton collisions early 2015. LS1 gave the opportunity to the
 856 LHC and to the its experiments to undergo upgrades. The accelerator is now providing collisions
 857 at center-of-mass energy of 13 TeV and bunch crossing rate of 40 MHz, with a peak luminosity
 858 exceeding its design value. During the first and upcoming second LHC Long Shutdown, the Compact
 859 Muon Solenoid (CMS) detector is also undergoing a number of upgrades to maintain a high system
 860 performance [21].

861 From the LHC Phase-2 or High Luminosity LHC (HL-LHC) period onwards, i.e. past the Third
 862 Long Shutdown (LS3), the performance degradation due to integrated radiation as well as the average
 863 number of inelastic collisions per bunch crossing, or pileup, will rise substantially and become a
 864 major challenge for the LHC experiments, like CMS that are forced to address an upgrade program
 865 for Phase-II [22]. Simulations of the expected distribution of absorbed dose in the CMS detector
 866 under HL-LHC conditions, show in figure 4.16 that detectors placed close to the beamline will have
 867 to withstand high irradiation, the radiation dose being of the order of a few tens of Gy.

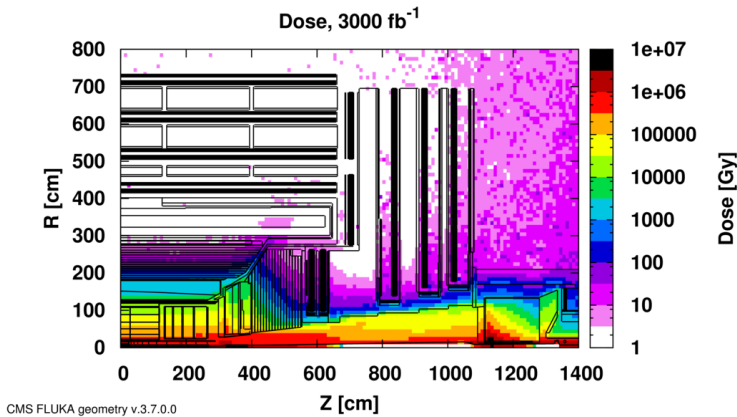


Figure 2.7: Absorbed dose in the CMS cavern after an integrated luminosity of 3000 fb. R is the transverse distance from the beamline and Z is the distance along the beamline from the Interaction Point at Z=0.

868 The measurement of small production cross-section and/or decay branching ratio processes, such
 869 as the Higgs boson coupling to charge leptons or the $B_s \rightarrow \mu^+ \mu^-$ decay, is of major interest and
 870 specific upgrades in the forward regions of the detector will be required to maximize the physics
 871 acceptance on the largest possible solid angle. To ensure proper trigger performance within the
 872 present coverage, the muon system will be completed with new chambers. In figure 2.8 one can
 873 see that the existing Cathode Strip Chambers (CSCs) will be completed by Gas Electron Multipliers
 874 (GEMs) and Resistive Plate Chambers (RPCs) in the pseudo-rapidity region $1.6 < |\eta| < 2.4$ to
 875 complete its redundancy as originally scheduled in the CMS Technical Proposal [23].

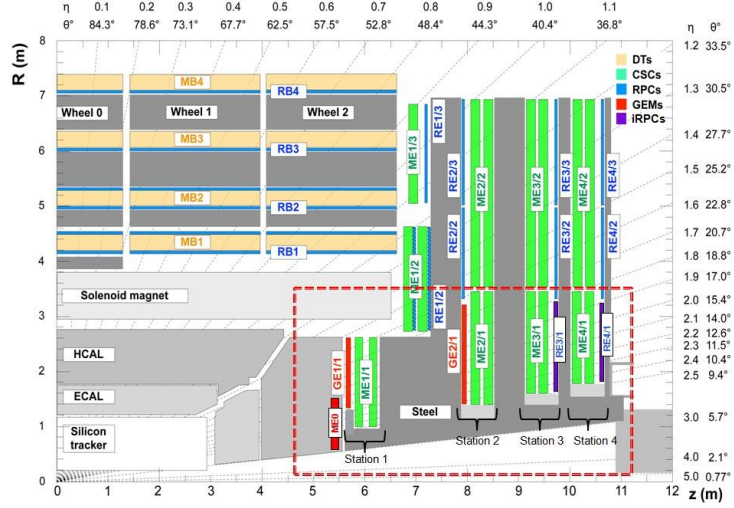


Figure 2.8: A quadrant of the muon system, showing DTs (yellow), RPCs (light blue), and CSCs (green). The locations of new forward muon detectors for Phase-II are contained within the dashed box and indicated in red for GEM stations (ME0, GE1/1, and GE2/1) and dark blue for improved RPC (iRPC) stations (RE3/1 and RE4/1).

876 RPCs are used by the CMS first level trigger for their good timing performances. Indeed, a very
 877 good bunch crossing identification can be obtained with the present CMS RPC system, given their
 878 fast response of the order of 1 ns. In order to contribute to the precision of muon momentum mea-
 879 surements, muon chambers should have a spatial resolution less or comparable to the contribution
 880 of multiple scattering [21]. Most of the plausible physics is covered only considering muons with
 881 $p_T < 100$ GeV thus, in order to match CMS requirements, a spatial resolution of $\mathcal{O}(\text{few mm})$ the
 882 proposed new RPC stations, as shown by the simulation in figure 2.9. According to preliminary
 883 designs, RE3/1 and RE4/1 readout pitch will be comprised between 3 and 6 mm and 5 η -partitions
 884 could be considered.

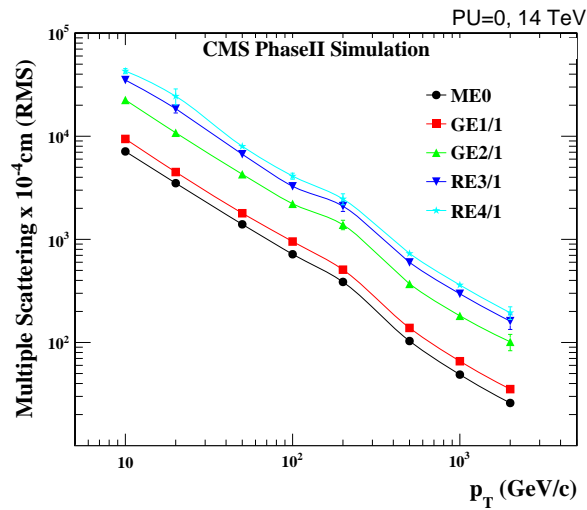


Figure 2.9: RMS of the multiple scattering displacement as a function of muon p_T for the proposed forward muon stations. All of the electromagnetic processes such as bremsstrahlung and magnetic field effect are included in the simulation.

3

885

886

Physics of Resistive plate chambers

887 A Resistive Plate Chamber (RPC) is a gaseous detector using the same physical processes described
888 in Chapter 3. It has been developed in 1981 by Santonico and Cardarelli [24], under the name of
889 *Resistive Plate Counter*, as an alternative to the local-discharge spark counters proposed in 1978
890 by Pestov and Fedotovich [25, 26]. Working with spark chambers implied using high-pressure gas
891 and high mechanical precision which the RPC simplified by formerly using a gas mixture of argon
892 and butane flowed at atmospheric pressure and a constant and uniform electric field propagated
893 in between two parallel electrode plates. Moreover, a significant increase in rate capability was
894 introduced by the use of electrode plate material with high bulk resistivity, preventing the discharge
895 from growing throughout the whole gas gap. Indeed, the effect of using resistive electrodes is that
896 the constant electric field is locally canceled out by the development of the discharge, limiting its
897 growth.

898 Through its development history, different operating modes [27–29] and new detector designs [30–
899 32] have been discovered, leading to further improvement of the rate capability of such a detector.
900 Moreover, the addition of SF_6 into the gas mix improved the stability of operation of the RPC [33,
901 34].

902 The low developing costs and easily achievable large detection areas offered by RPCs, as well as
903 the wide range of possible designs, made them a natural choice to as muon chambers and/or trigger
904 detectors in multipurpose experiments such as CMS [21] or ATLAS [35], time-of-flight detectors in
905 ALICE [36], calorimeter with CALICE [37] or even detectors for volcanic muography with ToMu-
906 Vol [38].

907 3.1 Principle

908 RPCs are ionisation detectors composed of two parallel resistive plate electrodes in between which
909 a constant electric field is set. The space in between the electrodes, referred as *gap*, is filled with a
910 dense gas that is used to generate primary ionization into the gas volume. The free charge carriers
911 (electrons and cations) created by the ionization of the gas molecules are then accelerated towards

912 the electrodes by the electric field, as shown in Figure 3.1 [39].

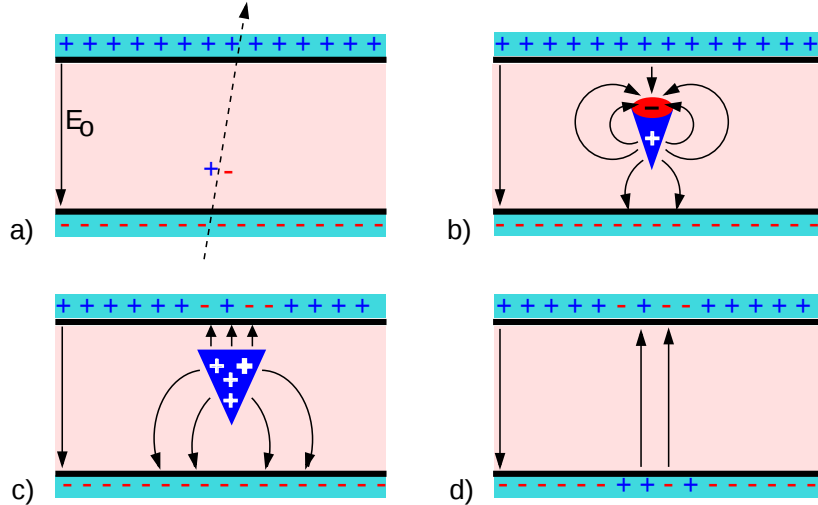


Figure 3.1: Different phases of the avalanche development in the RPC gas volume subjected to a constant electric field E_0 . a) An avalanche is initiated by the primary ionisation caused by the passage of a charged particle through the gas volume. b) Due to its growing size, the avalanche starts to locally influence the electric field. c) The electrons, lighter than the cations reach the anode first. d) The ions reach the cathode. While the charges have not recombined, the electric field in the small region around the avalanche stays affected and locally blind the detector.

913 RPCs being passive detectors, a current on pick-up copper read-out placed outside of the gas
 914 volume is induced by the charge accumulation during the growth of the avalanche. As a result,
 915 the time resolution of the detector is substantially increased as the output signal is generated while
 916 the electrons are still in movement. The advantage of a constant electric field, over multi-wire
 917 proportional chambers, is that the electrons are being fully accelerated from the moment charge
 918 carriers are freed and feel the full strength of the electric field that doesn't depend on the distance to
 919 the readout and that the output signal doesn't need for the electrons to be physically collected.

920 The typical gas mixture RPCs are operated with is generally composed of 3 gas compounds.

- 921 ● Tetrafluoroethane ($C_2F_4H_2$), also referred to as *Freon*, is the principal compound of the RPC
 922 gas mixtures, with a typical fraction above 90%. It is used for it's high effective Townsend
 923 coefficient and the great average fast charge that allows to operate the detector with a high
 924 threshold with respect to argon, for example, that has similar effective Townsend coefficient
 925 but suffers from a lower fast charge. To operate with similar conditions, argon would require a
 926 higher electric field leading to a higher fraction of streamers, thus limiting the rate capability
 927 of the detector [40].
- 928 ● Isobutane (i- C_4H_{10}), only present in a few percent in the gas mixtures, is used for its UV
 929 quenching properties [41] helping to prevent streamers due to UV photon emission during the
 930 avalanche growth.
- 931 ● Sulfur hexafluoride, (SF_6), referred to simply as *SF6*, is used in very little quantities for its
 932 high electronegativity. Excess of electrons are being absorbed by the compound and streamers

are suppressed [34]. Nevertheless, a fraction of SF_6 higher than 1% will not bring any extra benefit in terms of streamer cancelation power but will lead to higher operating voltage [33], as can be understood through Figure 3.2.

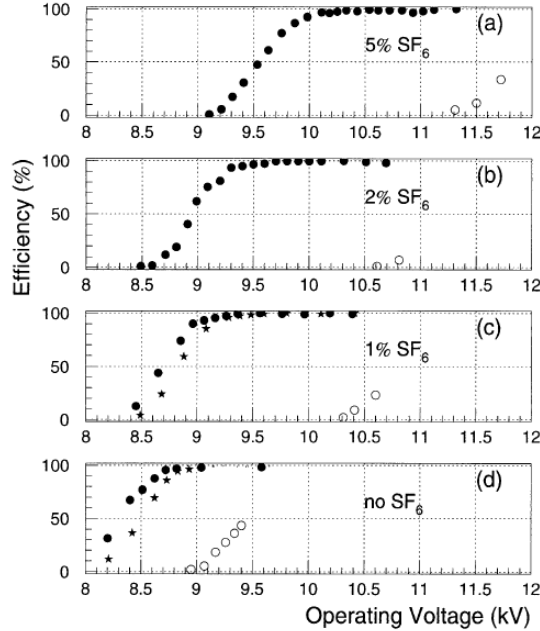


Figure 3.2: Effeciency (circles and stars with 30 mV and 100 mV thresholds respectively) and streamer probability (opened circles) as function of the operating voltatge of a 2 mm single gap HPL RPC flushed with a gas mixture containing (a) 5%, (b) 2%, (c) 1% and (d) no SF_6 [33].

After an avalanche developed in the gas, a time long compared to the development of a discharge is needed to recombine the charge carriers in the electrode material due to their resistivity. This property has the advantage of affecting the local electric field and avoiding sparks in the detector but, on the other hand, the rate capability is intrinsically limited by the time constant τ_{RPC} of the detector. Using a quasi-static approximation of Maxwell's equations for weakly conducting media, it can be shown that the time constant τ_{RPC} necessary to the charge recombination at the interface in between the electrode and the gas volume is given by the Formula 3.1 [42].

$$\tau_{RPC} = \frac{\epsilon_{electrode} + \epsilon_{gas}}{\sigma_{electrode} + \sigma_{gas}} \quad (3.1)$$

A gas can be assimilated to vacuum, leading to $\epsilon_{gas} = \epsilon_0$ and $\sigma_{gas} = 0$, and the electrodes permittivity and conductivity can be written as $\epsilon_{electrode} = \epsilon_r \epsilon_0$ and $\sigma_{electrode} = 1/\rho_{electrode}$, showing the strong dependence of the time constant to the electrodes resistivity in Formula 3.2.

$$\tau_{RPC} = (\epsilon_r + 1)\epsilon_0 \times \rho_{electrode} \quad (3.2)$$

Very few materials with a low enough resistivity exist in nature. The resistivity targeted to build RPCs ranges from 10^9 to $10^{12} \Omega \cdot \text{cm}$. The most common RPC electrode materials are displayed in Table 3.1. When the doped glass and ceramics can offer short time constants of the order of 1 ms,

949 the developing cost of such materials is quite high due to the very low demand. Thus, High-pressure
 950 laminate (HPL) is often the choice for high rate experiments using very large RPC detection areas.
 951 Other experiments working at cosmic muon fluxes can safely operate with ordinary float glass.

Material	$\rho_{electrode}$ ($\Omega \cdot \text{cm}$)	ϵ_r	τ_{RPC} (ms)
Float glass	10^{12}	~ 7	~ 700
High-pressure laminate	10^{10} to 10^{12}	~ 6	~ 6 to 600
Doped glass (LR S)	10^9 to 10^{11}	~ 10	~ 1 to 100
Doped ceramics (SiN/SiC)	10^9	~ 8.5	~ 1
Doped ceramics (Ferrite)	10^8 to 10^{12}	~ 20	~ 0.2 to 2000

Table 3.1: Properties of the most used electrode materials for RPCs.

952 3.1.1 Electron drift velocity

953 Talk about the electron drift velocity and mention the time resolution of RPCs.

954 3.2 Rate capability and time resolution of Resistive Plate Cham- 955 bers

956 As already previously discussed, the electrode material plays a key role in the max intrinsic rate
 957 capability of RPCs. R&D is being done to develop at always cheaper costs material with lower
 958 resistivity. Nevertheless, the amount of charge released, i.e. the size of the discharge, if reduced
 959 leads to a smaller blind area in the detector, increasing the rate capability of the detector.

960 3.2.1 Operation modes

961 RPCs where developed early 1980s. At that time it was using an operating mode now referred to
 962 as *streamer mode*. Streamers are large discharges that develop in between the 2 electrodes enough
 963 to locally discharge the electrodes. If the electric field inside of the gas volume is strong enough,
 964 with electrons being fast compared to ions, a large and dense cloud of positive ions will develop
 965 nearby the anode and extend toward the cathode while the electrons are being collected, eventually
 966 leading to a streamer discharge due to the increase of field seen at the cathode. the field is then strong
 967 enough so that electrons are pulled out of the cathode. Electrodes, though they are a unique volume
 968 of resistive material, can be assimilated to capacitors. At the moment an electric field is applied in
 969 between their outer surfaces, the charge carriers inside of the volume will start moving leading to
 970 a situation where there is no voltage across the electrodes and a higher density of negative charges,
 971 i.e. electrons, on the inner surface of the cathode. Finally, when a streamer discharge occurs, these
 972 electrons are partially released in the gas volume contributing to increase the discharge strength until
 973 the formation of a conductive plasma, the streamer. This can be understood through Figure 3.3 [27].
 974 Streamer signals are very convenient in terms of read-out as no amplification is required with output
 975 pulses amplitudes of the order of a few tens to few hundreds of mV as can be seen on Figure 3.4.

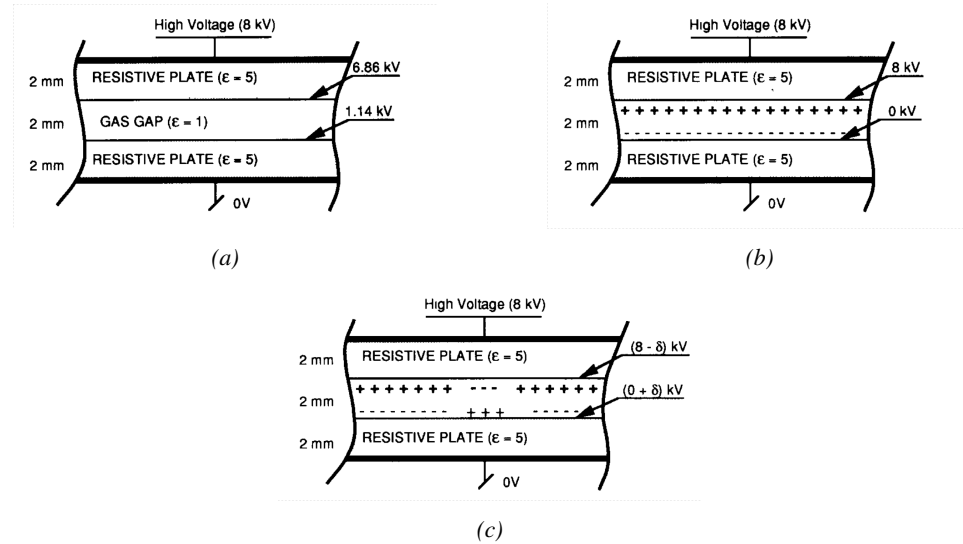


Figure 3.3: Movement of the charge carriers in an RPC. Figure 3.3a: Voltage across an RPC whose electrode have a relative permittivity of 5 at the moment the tension is applied. Figure 3.3b: After the charge carriers moved, the electrodes are charged and there is no voltage drop over the electrodes anymore. The full potential is applied on the gas gap only. Figure 3.3c: The streamer discharge initiated by a charged particle transports electrons and cations towards the anode and cathode respectively.

When the electric field is reduced though, the electronic gain is small until the electrons get close enough to the anode and the positive ion cloud is much smaller. The electric field cannot rise to the point a field emission of electrons on the cathode is possible. The resulting signal is weak, of the order of a few mv as shown on Figure 3.4, and requires amplification. This is the *avalanche mode* of RPC operation.

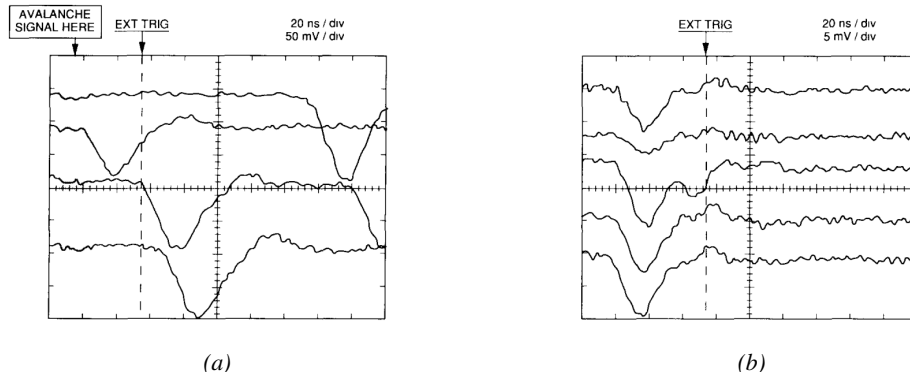


Figure 3.4: Typical oscilloscope pulses in streamer mode (Figure 3.4a) and avalanche mode (Figure 3.4b). In the case of streamer mode, the very small avalanche signal is visible.

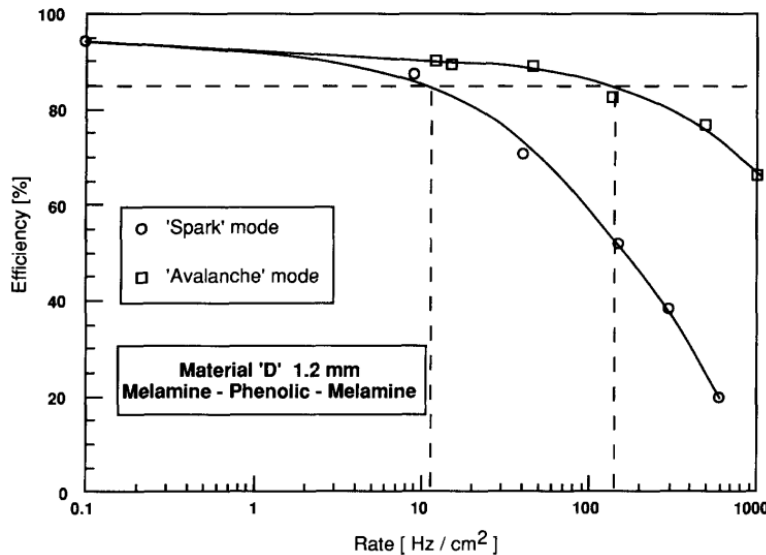


Figure 3.5: Rate capability comparison for the streamer and avalanche mode of operation. An order of magnitude in rate capability for a maximal efficiency drop of 10% is gained by using the avalanche mode over the streamer mode.

This mode offers a higher rate capability by providing smaller discharges that don't affect the electrodes charge and are more locally contained in the gas volume as was demonstrated by Crotty with Figure 3.5 [27]. The detector only stays locally blind the time the charge carriers are recombined and there is no need for electrode recharge which is a long process affecting a large portion of the detector. Another advantage of avalanche signals over streamer is the great time consistency. Figure 3.4 shows very clearly that avalanche signals have a very small time jitter. This is a natural choice for high rate experiments.

3.2.2 Detector designs and performance

Different RPC design have been used and each of them present its own advantages. Historically, the first type of RPC to have been developed is what is referred now to *narrow gap* RPC [24, 43]. After the avalanche mode has been discovered [27], it has been proven that increasing the width of the gas gap lead to higher rate capability, due to lower charge deposition per avalanche, and lower power dissipation [43]. Nevertheless, by increasing the gas gap width, the time resolution of the detector decreases. This is a natural result if the increase of active gas volume in the detector is taken into account. Indeed, for a given threshold, only the small fraction of gas closest to the cathode will provide enough gain to have a detectable signal. In the case of a wider gas volume, the active region is then larger and a larger time jitter is introduced with the variation of starting position of the avalanche, as discussed in [30]. To solve improve both the time resolution and the rate capability, different methods were used trying to get advantages of both narrow and wide gap RPCs.

3.2.2.1 Double-gap RPC

Double-gap RPCs are made out of 2 narrow RPC detectors. The 2 RPC gaps are stacked on top of each other as shown in Figure 3.6. This detector layout, popularized by the two multipurpose experiments CMS [21] and ATLAS [35] at LHC, can be used as an OR system in which each individual chamber participates in the output signal. The gain of such a detector is greatly reduced with respect to single-gap RPCs with an efficiency plateau reached at lower voltage, as visible on Figure 3.7.

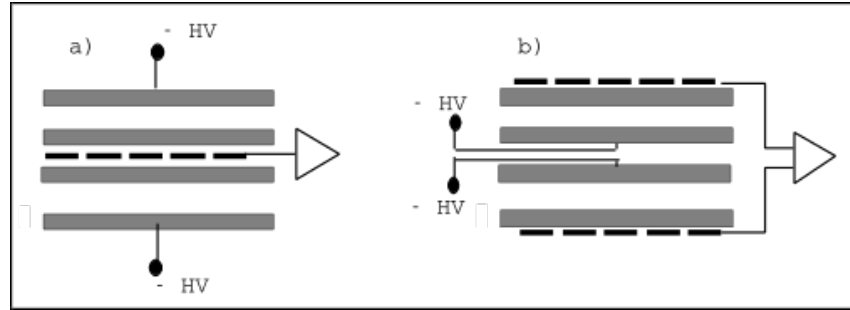


Figure 3.6: Possible double-gap RPC layouts: a) "standard" 1D double-gap RPC, as used in CMS experiment, where the anodes are facing each other and a 1D read-out plane is sandwiched in between them, b) double read-out double-gap RPC as used in ATLAS experiment, where the cathodes are facing each other and 2 read-out planes are used on the outer surfaces. This last layout can offer the possibility to use a 2D reconstruction by using orthogonal read-out planes.

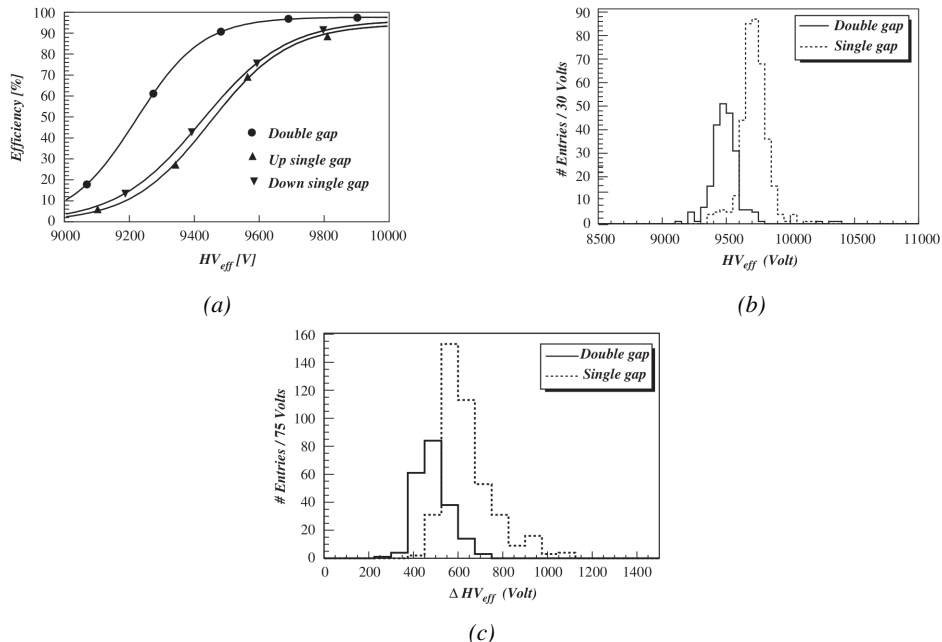


Figure 3.7: Comparison of performance of CMS double and single gap RPCs using cosmic muons [44]. Figure 3.7a: Comparison of efficiency sigmoids. Figure 3.7b: Voltage distribution at 95% of maximum efficiency. Figure 3.7c: $\Delta_{10\%}^{90\%}$ distribution.

3.2.2.2 Multigap RPC (MRPC)

MRPCs are layouts in which floating sub electrode plates are placed into a wide gap RPC to divide the gas volume and create a sum of narrow gaps [30, 31]. The time resolution of such a detector can reach of few tens of ps, with gas gaps of the order of a few hundred μm as shown in Figure 3.8 representing ALICE Time-of-flight (ToF) MRPCs.

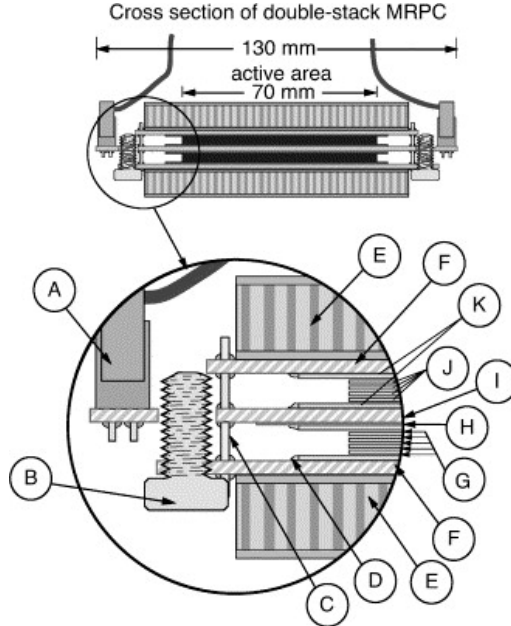


Figure 3.8: Presentation of ALICE MRPC using $250 \mu\text{m}$ gas gaps, $620 \mu\text{m}$ outer glass electrodes and $550 \mu\text{m}$ inner floating electrodes. More details on the labels are given in [45].

Sometimes used as a double multigap RPC, taking advantage of the OR of double gap RPCs, the MRPC is mainly used as ToF detector [45–49] due to its excellent timing properties that allow to perform particle identification as explained by Williams in [50]. The principle of particle identification using ToF is simply the measurement of the velocity of a particle. Indeed, particles are defined by their mass (for the parameter of interest here, their electric charge being measured using the bending angle of the particles traveling through a magnetic field) and this mass can be calculated by measuring the velocity β and momentum of the particle:

$$\beta = \frac{p}{\sqrt{p^2 + m^2}} \quad (3.3)$$

Intuitively, it is trivial to understand that 2 different particles having the same momentum will have a different velocity due to the mass difference and thus a different flight time T_1 and T_2 through the detector and this is used to separate and identify particles. The better the time resolution of the ToF system used, the stronger will the separation be:

$$T = \frac{L}{v} = \frac{L}{c \cdot \beta}, \quad \Delta T = T_1 - T_2 = \frac{L}{c} \left(\sqrt{1 + m_1^2/p^2} - \sqrt{1 + m_2^2/p^2} \right) \cong (m_1^2 - m_2^2) \frac{L}{2cp^2} \quad (3.4)$$

1022 An example of particle identification is given for the case of STAR experiment in Figure 3.9.

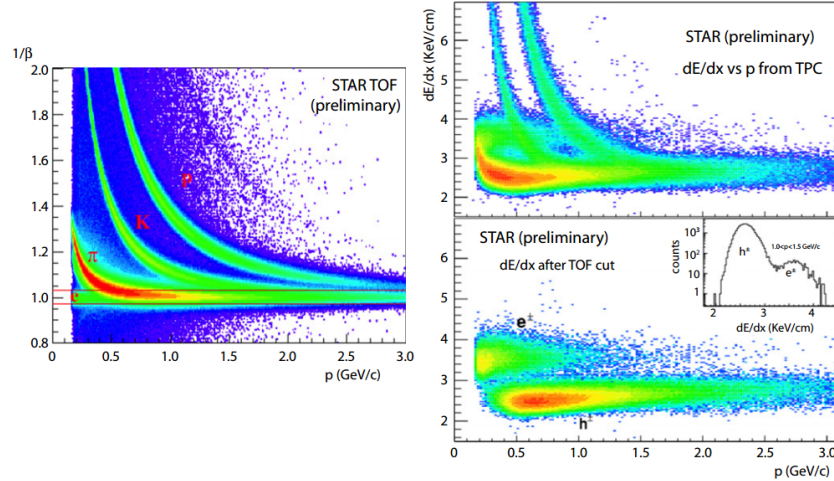


Figure 3.9: Particle identification applied to electrons in the STAR experiment. The identification is performed combining ToF and dE/dx measurements [50].

1023 Another benefice of using such small gas gaps is the strong reduction of the average avalanche
1024 volume and thus of the blind spot on MRPCs leading to an improved rate capability. Multigaps can
1025 sustain backgrounds of several kHz/cm² as demonstrated in Figure 3.10.

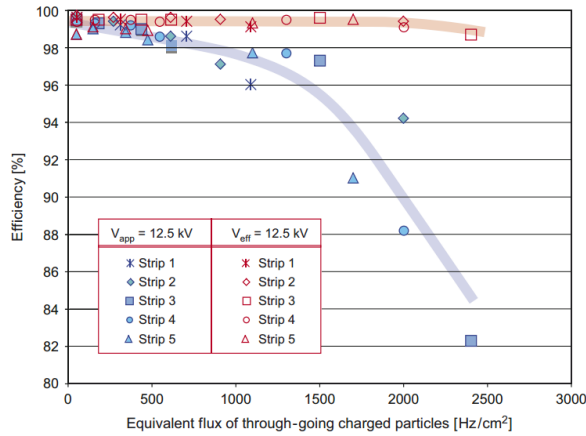


Figure 3.10: Comparison of the detector performance of ALICE ToF MRPC [51] at fixed applied voltage (in blue) and at fixed effective voltage (in red). The effective voltage is kept fixed by increasing the applied voltage accordingly to the current drawn by the detector.

1026 3.2.2.3 Charge distribution and performance limitations

1027 The direct consequence of the different RPC layouts is a variation of intrinsic time resolution of the
1028 RPC as the gap size decreases. An advantage is given to multigaps whose design use sub-millimeter
1029 gas volumes providing very consistent signals.

1030 On the charge spectrum point of view, each layout has its own advantages. When the double-gap
 1031 has the highest induced over drifting charge ratio, as seen in Figure 3.11, the multigap has a charge
 1032 spectrum strongly detached from the origin, as visible in Figure 3.12. A high induced over drifting
 1033 charge ratio means that the double gap can be safely operated at high threshold or that at similar
 1034 threshold it can be operated with a twice smaller drifting charge, meaning a higher rate capability.
 1035 On the other hand, the strong detachment of the charge spectrum from the origin in the MRPC case
 1036 allows to reach a higher efficiency with increasing threshold as most of the induced charge is not low
 1037 due to the convolution of several single gap spectra. The range of stable efficiency increases with
 1038 the number of gap, as presented in Figure 3.13.

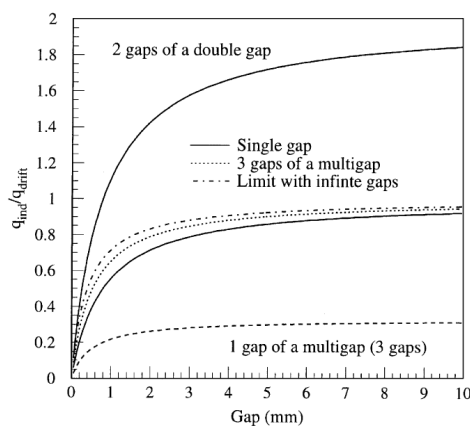


Figure 3.11: Ratio between total induced and drifting charge have been simulated for single gap, double-gap and multigap layouts [52]. The total induced charge for a double-gap RPC is a factor 2 higher than for a multigap.

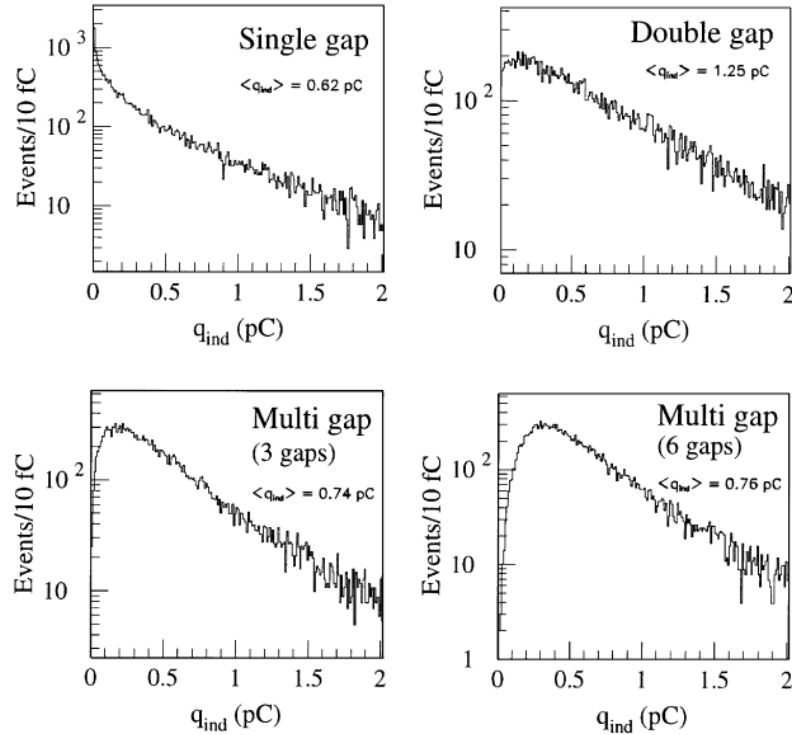


Figure 3.12: Charge spectra have been simulated for single gap, double-gap and multigap layouts [52]. It appears that when single gap shows a decreasing spectrum, double and multigap layouts exhibit a spectrum whose peak is detached from the origin. The detachment gets stronger as the number of gaps increases.

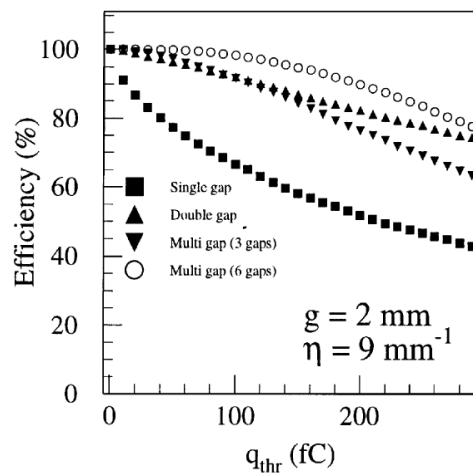


Figure 3.13: The maximal theoretical efficiency is simulated for single gap, double-gap and multigap layouts [52] at a constant gap thickness of 2 mm and using an effective Townsend coefficient of 9 mm^{-1} .

¹⁰³⁹ **3.3 Signal formation**

¹⁰⁴⁰ **3.4 Gas transport parameters**

4

1041

1042

1043

Longevity studies and Consolidation of the present CMS RPC subsystem

1044

4.1 Resistive Plate Chambers at CMS

1045

4.1.1 Overview

1046

The Resistive Plate Chambers (RPC) system, located in both barrel and endcap regions, provides a fast, independent muon trigger with a looser p_T threshold over a large portion of the pseudorapidity range ($|\eta| < 1.6$) [add reconstruction].

1047

During High-Luminosity LHC (HL-LHC) operations the expected conditions in terms of background and pile-up will make the identification and correct P_T assignment a challenge for the Muon system. The goal of RPC upgrade is to provide additional hits to the Muon system with precise timing. All these informations will be elaborated by the trigger system in a global way enhancing the performance of the trigger in terms of efficiency and rate control. The RPC Upgrade is based on two projects: an improved Link Board System and the extension of the RPC coverage up to $|\eta| = 2.4$. [FIXME 2.4 or 2.5?]

1048

The Link Board system, that will be described in section xxx, is responsible to process, synchronize and zero-suppress the signals coming from the RPC front end boards. The Link Board components have been produced between 2006 and 2007 and will be subjected to aging and failure in the long term. The upgraded Link Board system will overcome the aging problems described in section xxx and will allow for a more precise timing information to the RPC hits from 25 to 1 ns [ref section xxx].

1049

The extension of the RPC system up to $|\eta| = 2.1$ was already planned in the CMS TDR [ref cmstdr] and staged because of budget limitations and expected background rates higher than the rate capability of the present CMS RPCs in that region. An extensive R&D program has been done in order to develop an improved RPC that fulfills the CMS requirements. Two new RPC layers in the innermost ring of stations 3 and 4 will be added with benefits to the neutron-induced background

1050

1051

1052

1053

1054

1055

1056

1057

1058

1059

1060

1061

1062

1063

1064

1065

1066

1067

1068 reduction and efficiency improvement for both trigger and offline reconstruction.

1069 4.1.2 The present RPC system

1070 The RPC system is organized in 4 stations called RB1 to RB4 in the barrel region, and RE1 to RE4
 1071 in the endcap region. The innermost barrel stations, RB1 and RB2, are instrumented with 2 layers
 1072 of RPCs facing the innermost (RB1in and RB2in) and outermost (RB1out and RB2out) sides of the
 1073 DT chambers. Every chamber is then divided from the read-out point of view into 2 or 3 η partitions
 1074 called “rolls”. The RPC system consist of 480 barrel chambers and 576 endcap chambers. Details
 1075 on the geometry are discussed in the paper [ref to geo paper].

1076 The CMS RPC chamber is a double-gap, operated in avalanche mode to ensure reliable operation
 1077 at high rates. Each RPC gap consists of two 2-mm-thick resistive High-Pressure Laminate (HPL)
 1078 plates separated by a 2-mm-thick gas gap. The outer surface of the HPL plates is coated with a thin
 1079 conductive graphite layer, and a voltage is applied. The RPCs are operated with a 3-component,
 1080 non-flammable gas mixture consisting of 95.2% freon ($C_2H_2F_4$, known as R134a), 4.5% isobutane
 1081 ($i-C_4H_{10}$), and 0.3% sulphur hexafluoride (SF_6) with a relative humidity of 40% - 50%. Readout
 1082 strips are aligned in η between the 2 gas gaps. [\[Add a sentence on FEBs.\]](#)

1083 The discriminated signals coming from the Front End boards feed via twisted cables (10 to 20 m
 1084 long) the Link Board System located in UXC on the balconies around the detector. The Link System
 1085 consist of the 1376 Link Boards (LBs) and the 216 Control Boards (CBs), placed in 108 Link Boxes.
 1086 The Link Box is a custom crate (6U high) with 20 slots (for two CBs and eighteen LBs). The Link
 1087 Box contains custom backplane to which the cables from the chambers are connected, as well as the
 1088 cables providing the LBs and CBs power supply and the cables for the RPC FEBs control with use
 1089 of the I2C protocol (trough the CB). The backplane itself contains only connectors (and no any other
 1090 electronic devices).

1091 The Link Board has 96 input channels (one channel corresponds to one RPC strip). The input
 1092 signals are the ~ 100 ns binary pulses which are synchronous to the RPC hits, but not to the LHC
 1093 clock (which drives the entire CMS electronics). Thus the first step of the FEB signals processing
 1094 is synchronization, i.e. assignment of the signals to the BXes (25 ns periods). Then the data are
 1095 compressed with a simple zero-suppressing algorithm (the input channels are grouped into 8 bit
 1096 partitions, only the partitions with at least one nonzero bit are selected for each BX). Next, the non-
 1097 empty partitions are time-multiplexed i.e. if there are more than one such partition in a given BX,
 1098 they are sent one-by-one in consecutive BXes. The data from 3 neighbouring LBs are concentrated
 1099 by the middle LB which contains the optical transmitter for sending them to the USC over a fiber at
 1100 1.6 Gbps.

1101 The Control Boards provide the communication of the control software with the LBs via the
 1102 FEC/CCU system. The CBs are connected into token rings, each ring consists of 12 CBs of one
 1103 detector tower and a FEC mezzanine board placed on the CCS board located in the VME crate in
 1104 the USC. In total, there are 18 rings in the entire Link System. The CBs also perform automatic
 1105 reloading of the LB's firmware which is needed in order to avoid accumulation of the radiation
 1106 induced SEUs in the LBs firmware.

1107 Both LBs and CB are based on the Xilinx Spartan III FPGAs, the CB additionally contains
 1108 radiation-tolerant (FLASH based) FPGA Actel ProAsicPlus.

1109 The High Voltage power system is located in USC, not exposed to radiation and easily accessible
 1110 for any reparation. A single HV channel powers 2 RPC chambers both in the barrel and endcap
 1111 regions. The Low Voltage boards are located in UXC on the balconies and provide the voltage to the

¹¹¹² front end electronics.

¹¹¹³ 4.1.3 Pulse processing of CMS RPCs

¹¹¹⁴ Signals induced by cosmic particle in the RPC strips are shaped by standard CMS RPC Front-End
¹¹¹⁵ Electronics (FEE) following the scheme of Figure 4.1. On a first stage, analogic signals are amplified
¹¹¹⁶ and then sent to the Constant Fraction Discriminator (CFD) described in Figure 4.2. At the end of
¹¹¹⁷ the chain, 100 ns long pulses are sent in the LVDS output. These output signal are sent on one side to
¹¹¹⁸ a V1190A Time-to-Digital Converter (TDC) module from CAEN and on the other to an OR module
¹¹¹⁹ to count the number of detected signals. Trigger and hit coïncidences are monitored using scalers.
¹¹²⁰ The TDC is used to store the data into ROOT files. These files are thus analysed to understand the
¹¹²¹ detectors performance.

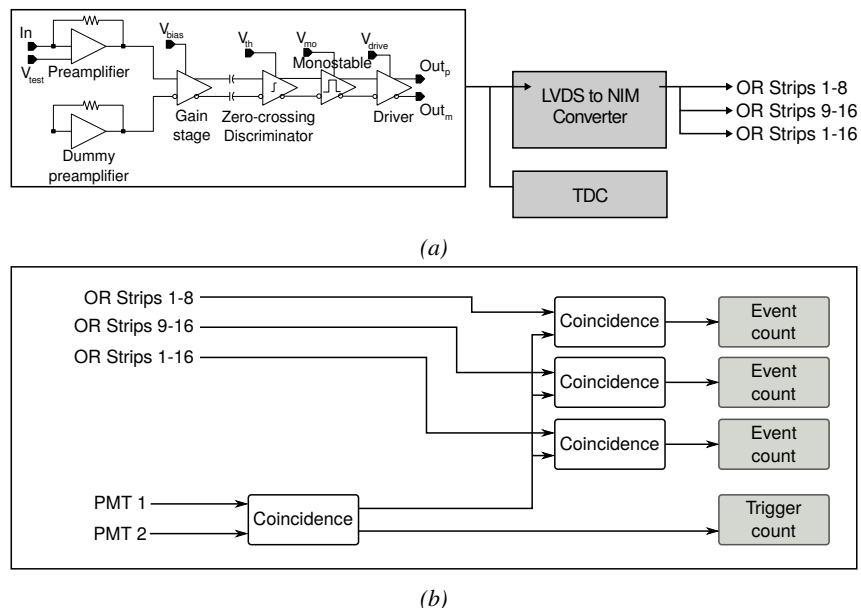


Figure 4.1: Signals from the RPC strips are shaped by the FEE described on Figure 4.1a. Output LVDS signals are then read-out by a TDC module connected to a computer or converted into NIM and sent to scalers. Figure 4.1b describes how these converted signals are put in coincidence with the trigger.

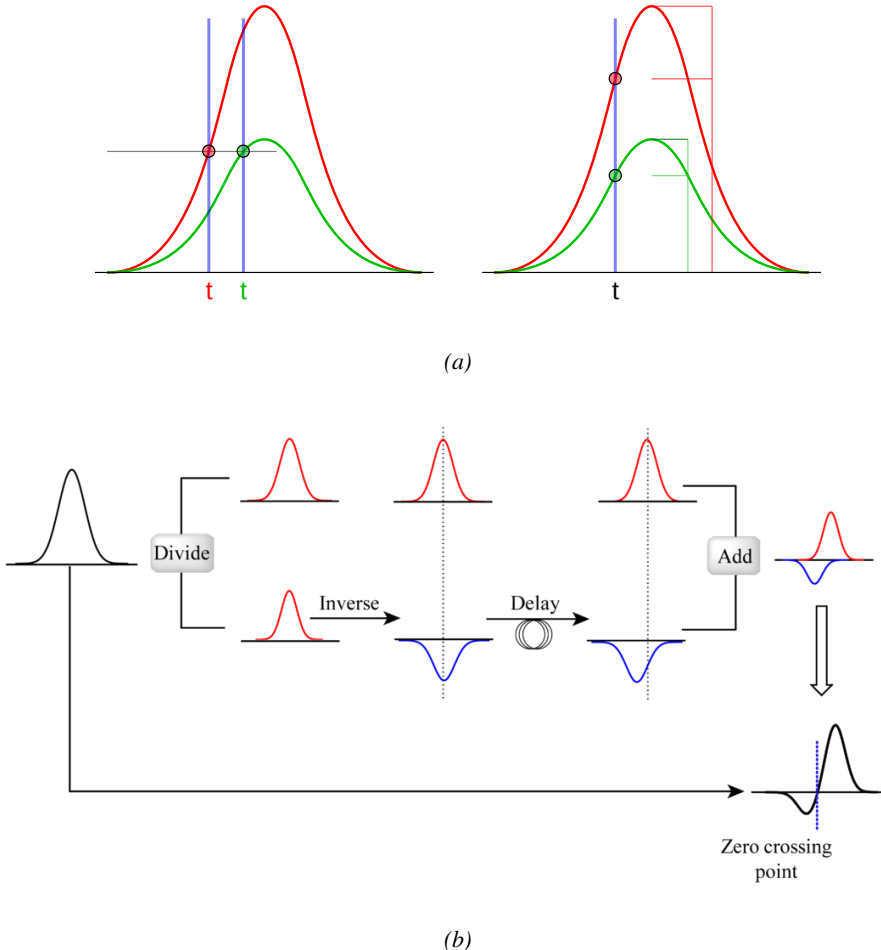


Figure 4.2: Description of the principle of a CFD. A comparison of threshold triggering (left) and constant fraction triggering (right) is shown in Figure 4.2a. Constant fraction triggering is obtained thanks to zero-crossing technique as explained in Figure 4.2b. The signal arriving at the input of the CFD is split into three components. A first one is delayed and connected to the inverting input of a first comparator. A second component is connected to the noninverting input of this first comparator. A third component is connected to the noninverting input of another comparator along with a threshold value connected to the inverting input. Finally, the output of both comparators is fed through an AND gate.

4.2 Testing detectors under extreme conditions

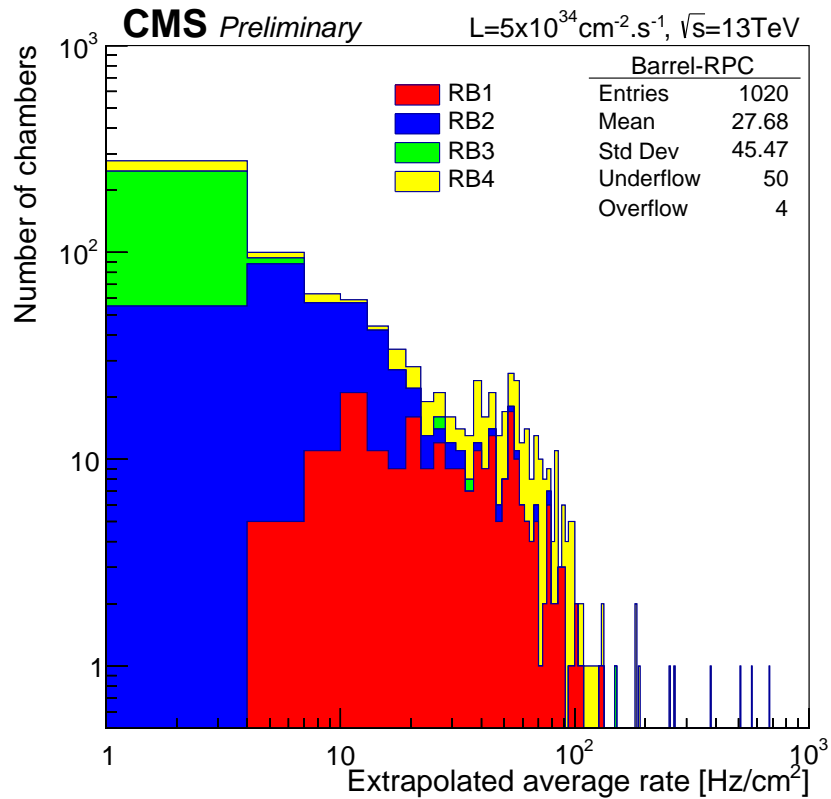
The upgrade from LHC to HL-LHC will increase the peak luminosity from $10^{34} \text{ cm}^{-2} \text{ s}^{-1}$ to reach $5 \times 10^{34} \text{ cm}^{-2} \text{ s}^{-1}$, increasing in the same way the total expected background to which the RPC system will be subjected to. Composed of low energy gammas and neutrons from $p\text{-}p$ collisions, low momentum primary and secondary muons, puch-through hadrons from calorimeters, and particles produced in the interaction of the beams with collimators, the background will mostly affect the regions of CMS that are the closest to the beam line, i.e. the RPC detectors located in the endcaps.

[To update.]

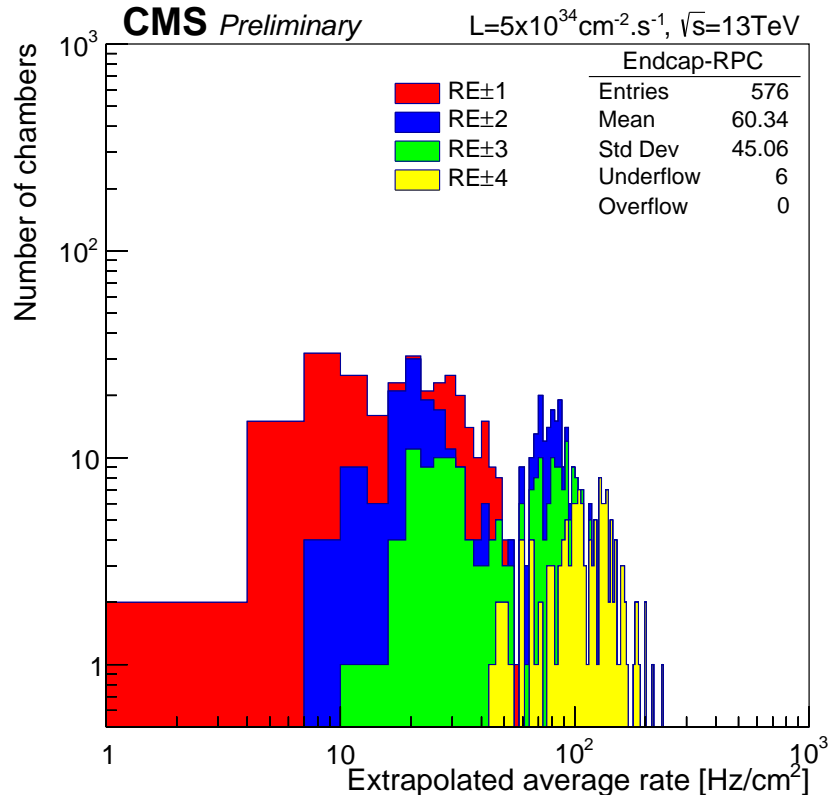
1130

1131 The 2016 data allowed to study the values of the background rate in all RPC system. In Fig-
1132 ure 4.3, the distribution of the chamber background hit rate per unit area is shown at a luminosity
1133 of $5 \times 10^{34} cm^{-2}.s^{-1}$ linearly extrapolating from data collected in 2016 [ref mentioning the linear
1134 dependency of rate vs lumi]. The maximum rate per unit area at HL-LHC conditions is expected to
1135 be of the order of $600 Hz/cm^2$ (including a safety factor 3). Nevertheless, Fluka simulations have
1136 conducted in order to understand the background at HL-LHC conditions. The comparison to the
1137 data has shown, in Figure 4.4, a discrepancy of a factor 2 even though the order of magnitude is
1138 consistent. [Understand mismatch.]

1139



(a)



(b)

Figure 4.3: (4.3a) Extrapolation from 2016 data of single hit rate per unit area in the barrel region. (4.3b) Extrapolation from 2016 data of single hit rate per unit area in the endcap region.

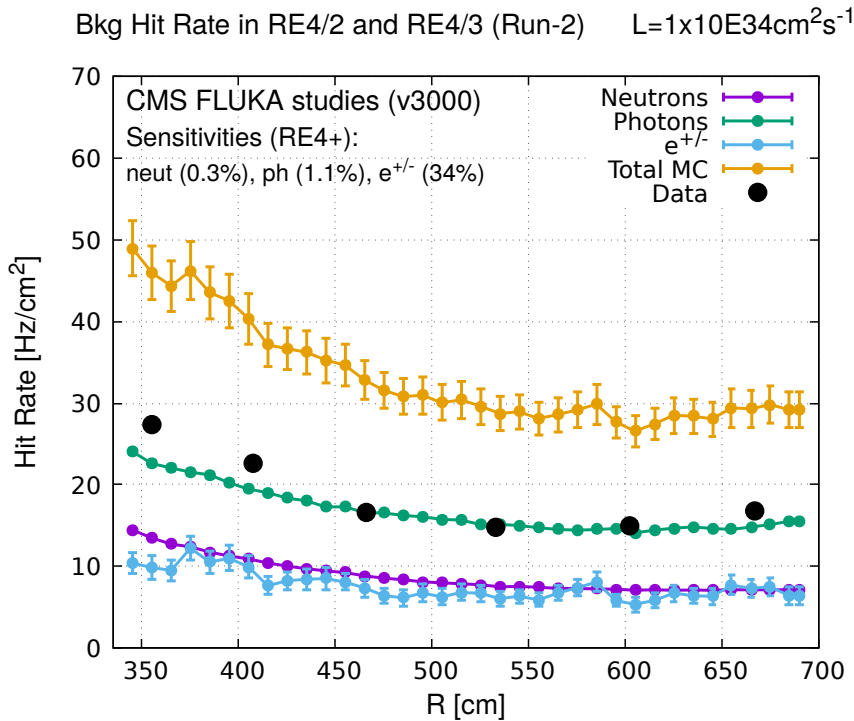


Figure 4.4: Background Fluka simulation compared to 2016 Data at $L = 10^{34} \text{ cm}^{-2} \cdot \text{s}^{-1}$ in the fourth endcap disk region. A mismatch in between simulation and data can be observed. [\[To be understood.\]](#)

In the past, extensive long-term tests were carried out at several gamma and neutron facilities certifying the detector performance. Both full size and small prototype RPCs have been irradiated with photons up to an integrated charge of $\sim 0.05 \text{ C}/\text{cm}^2$ and $\sim 0.4 \text{ C}/\text{cm}^2$, respectively [53, 54]. During Run-I, the RPC system provided stable operation and excellent performance and did not show any aging effects for integrated charge of the order of $0.01 \text{ C}/\text{cm}^2$. Projections on currents from 2016 Data, has allowed to determine that the total integrated charge, by the end of HL-LHC, would be of the order of $1 \text{ C}/\text{cm}^2$ (including a safety factor 3). [\[Corresponding figure needed.\]](#)

1147

1148 4.2.1 The Gamma Irradiation Facilities

1149 4.2.1.1 GIF

1150 Located in the SPS West Area at the downstream end of the X5 test beam, the Gamma Irradiation
 1151 Facility (GIF) was a test area in which particle detectors were exposed to a particle beam in presence
 1152 of an adjustable gamma background [55]. Its goal was to reproduce background conditions these
 1153 detectors would suffer in their operating environment at LHC. GIF layout is shown in Figure 4.5.
 1154 Gamma photons are produced by a strong ^{137}Cs source installed in the upstream part of the zone
 1155 inside a lead container. The source container includes a collimator, designed to irradiate a $6 \times 6 \text{ m}^2$
 1156 area at 5 m maximum to the source. A thin lens-shaped lead filter helps providing with a uniform
 1157 outcoming flux in a vertical plane, orthogonal to the beam direction. The principal collimator hole
 1158 provides a pyramidal aperture of $74^\circ \times 74^\circ$ solid angle and provides a photon flux in a pyramidal vol-

ume along the beam axis. The photon rate is controled by further lead filters allowing the maximum rate to be limited and to vary within a range of four orders of magnitude. Particle detectors under test are then placed within the pyramidal volume in front of the source, perpendicularly to the beam line in order to profit from the homogeneous photon flux. Adjusting the background flux of photons can then be done by using the filters and choosing the position of the detectors with respect to the source.

1164

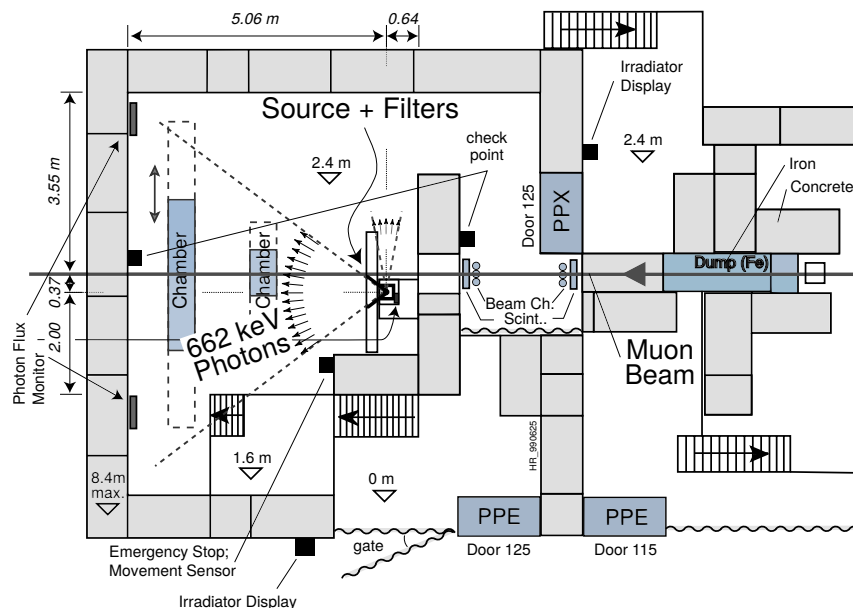


Figure 4.5: Layout of the test beam zone called X5c GIF at CERN. Photons from the radioactive source produce a sustained high rate of random hits over the whole area. The zone is surrounded by 8 m high and 80 cm thick concrete walls. Access is possible through three entry points. Two access doors for personnel and one large gate for material. A crane allows installation of heavy equipment in the area.

As described on Figure 4.6, the ^{137}Cs source emits a 662 keV photon in 85% of the decays. An activity of 740 GBq was measured on the 5th March 1997. To estimate the strength of the flux in 2014, it is necessary to consider the nuclear decay through time assiciated to the Cesium source whose half-life is well known ($t_{1/2} = (30.05 \pm 0.08)$ y). The GIF tests where done in between the 20th and the 31st of August 2014, i.e. at a time $t = (17.47 \pm 0.02)$ y resulting in an attenuation of the activity from 740 GBq in 1997 to 494 GBq in 2014.

1171

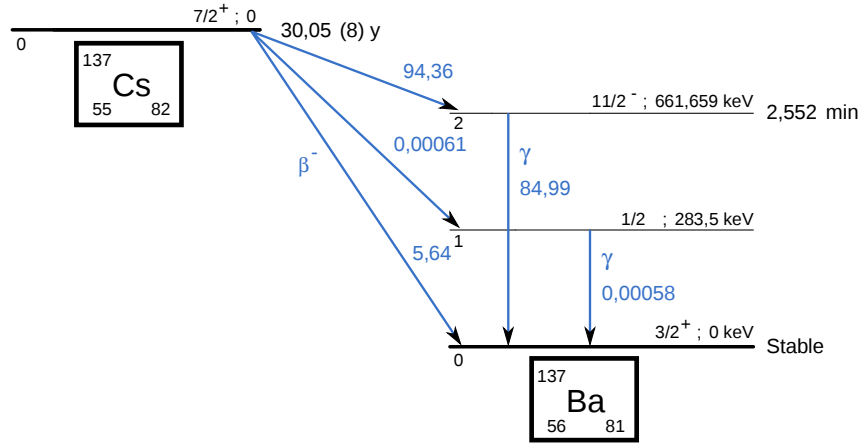


Figure 4.6: ^{137}Cs decays by β^- emission to the ground state of ^{137}Ba ($BR = 5.64\%$) and via the 662 keV isomeric level of ^{137}Ba ($BR = 94.36\%$) whose half-life is 2.55 min.

4.2.1.2 GIF++

The new Gamma Irradiation Facility (GIF++), located in the SPS North Area at the downstream end of the H4 test beam, has replaced its predecessor during LS1 and has been operational since spring 2015 [56]. Like GIF, GIF++ features a ^{137}Cs source of 662 keV gamma photons, their fluence being controlled with a set of filters of various attenuation factors. The source provides two separated large irradiation areas for testing several full-size muon detectors with continuous homogeneous irradiation, as presented in Figure 4.7.

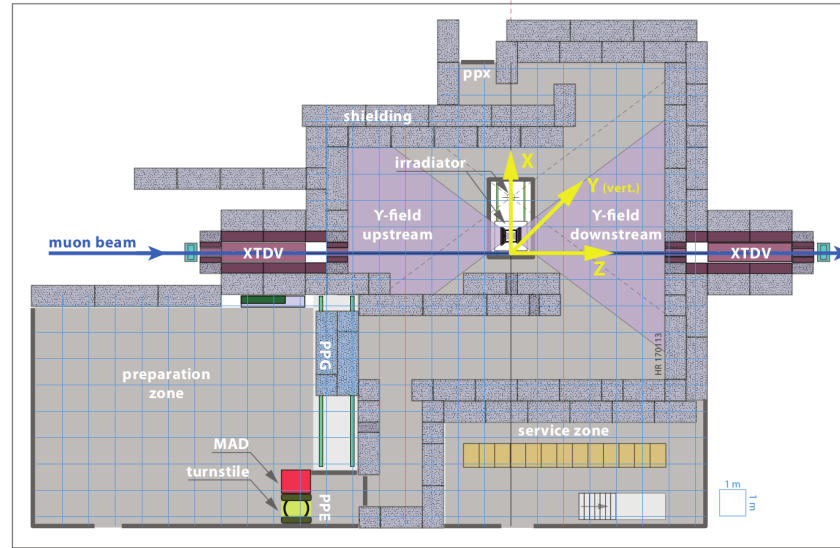


Figure 4.7: Floor plan of the GIF++ facility. When the facility downstream of the GIF++ takes electron beam, a beam pipe is installed along the beam line (z -axis). The irradiator can be displaced laterally (its center moves from $x = 0.65 \text{ m}$ to 2.15 m), to increase the distance to the beam pipe.

1180 The source activity was measured to be about 13.5 TBq in March 2016. The photon flux being
 1181 far greater than HL-LHC expectations, GIF++ provides an excellent facility for accelerated aging
 1182 tests of muon detectors.

1183

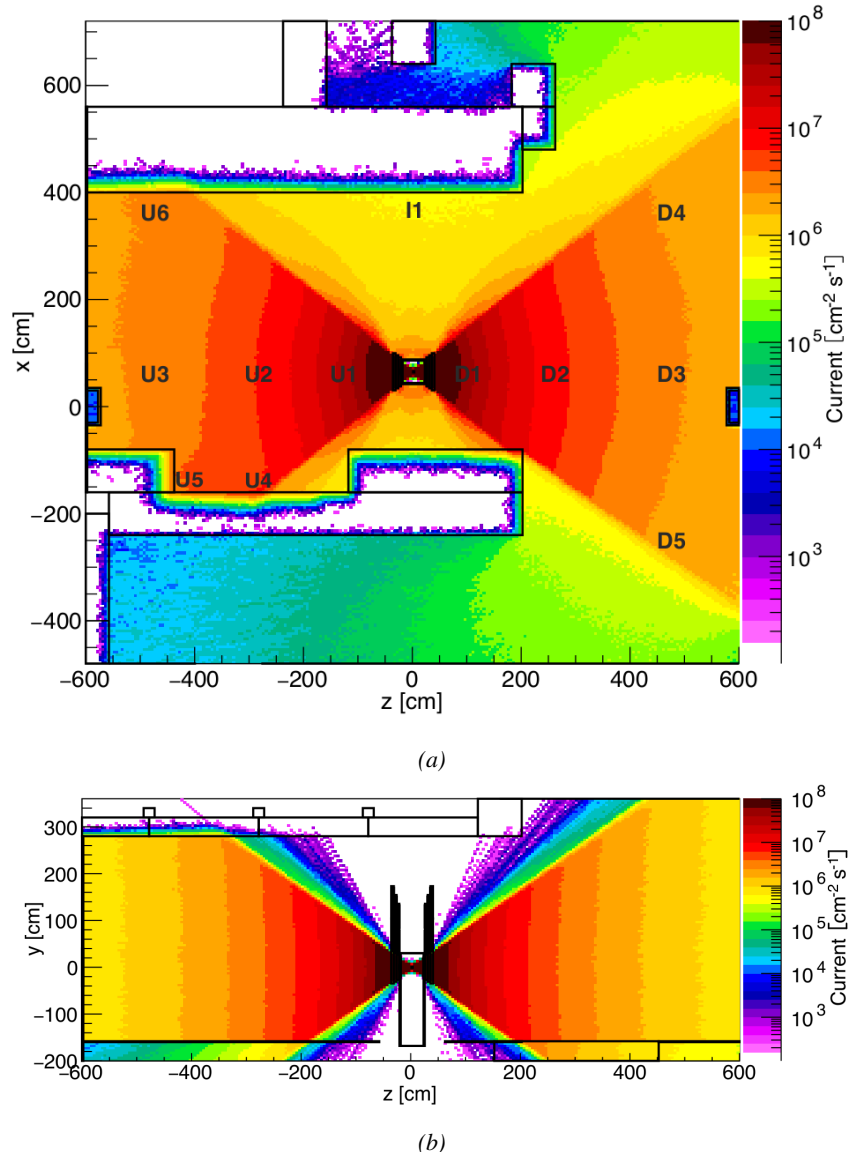


Figure 4.8: Simulated unattenuated current of photons in the xz plane (Figure 4.8a) and yz plane (Figure 4.8b) through the source at $x = 0.65$ m and $y = 0$ m. With angular correction filters, the current of 662 keV photons is made uniform in xy planes.

1184 The source is situated in the muon beam line with the muon beam being available a few times a
 1185 year. The H4 beam, composed of muons with a momentum of about 150 GeV/c, passes through the
 1186 GIF++ zone and is used to study the performance of the detectors. Its flux is of 104 particles/ cm^2

1187 focused in an area similar to $10 \times 10 \text{ cm}^2$. Therefore, with properly adjusted filters, one can imitate
 1188 the HL-LHC background and study the performance of muon detectors with their trigger/readout
 1189 electronics in HL-LHC environment.

1190

1191 4.3 Preliminary tests at GIF

1192 4.3.1 Resistive Plate Chamber test setup

1193 During summer 2014, preliminary tests have been conducted in the GIF area on a newly produced
 1194 RE4/2 chamber labelled RE-4-2-BARC-161. This chamber has been placed into a trolley covered
 1195 with a tent. The position of the RPC inside the tent and of the tent related to the source is described
 1196 in Figure 4.9. To test this CMS RPC, three different absorber settings were used. First of all,
 1197 measurements were done with fully opened source. Then, to complete this preliminary study, the
 1198 gamma flux has been attenuated from a factor 2 and a factor 5. The expected gamma flux at the level
 1199 of our detector will be discussed in subsection ??.

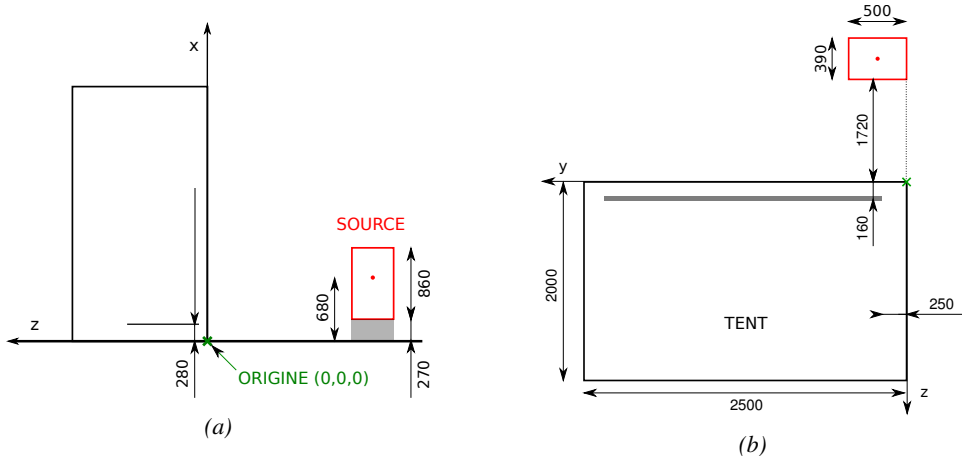


Figure 4.9: Description of the RPC setup. Dimensions are given in mm. A tent containing RPCs is placed at 1720 mm from the source container. The source is situated in the center of the container. RE-4-2-BARC-161 chamber is 160 mm inside the tent. This way, the distance between the source and the chambers plan is 2060 mm. Figure 4.9a provides a side view of the setup in the xz plane while Figure 4.9b shows a top view in the yz plane.



Figure 4.10: RE-4-2-BARC-I61 chamber is inside the tent as described in Figure 4.9. In the top right, the two scintillators used as trigger can be seen. This trigger system has an inclination of 10° relative to horizontal and is placed above half-partition B2 of the RPCs. PMT electronics are shielded thanks to lead blocks placed in order to protect them without stopping photons from going through the scintillators and the chamber.

1200 At the time of the tests, the beam not being operationnal anymore, a trigger composed of 2 plastic
 1201 scintillators has been placed in front of the setup with an inclination of 10 deg with respect to the
 1202 detector plane in order to look at cosmic muons. Using this particular trigger layout, shown on Fig-
 1203 ure 4.10, leads to a cosmic muon hit distribution into the chamber similar to the one in Figure 4.11.
 1204 Measured without gamma irradiation, two peaks can be seen on the profil of partition B, centered
 1205 on strips 52 and 59. Section ?? will help us understand that these two peaks are due respectively to
 1206 forward and backward coming cosmic particles where forward coming particles are first detected by
 1207 the scintillators and then the RPC while the backward coming muons are first detected in the RPC.

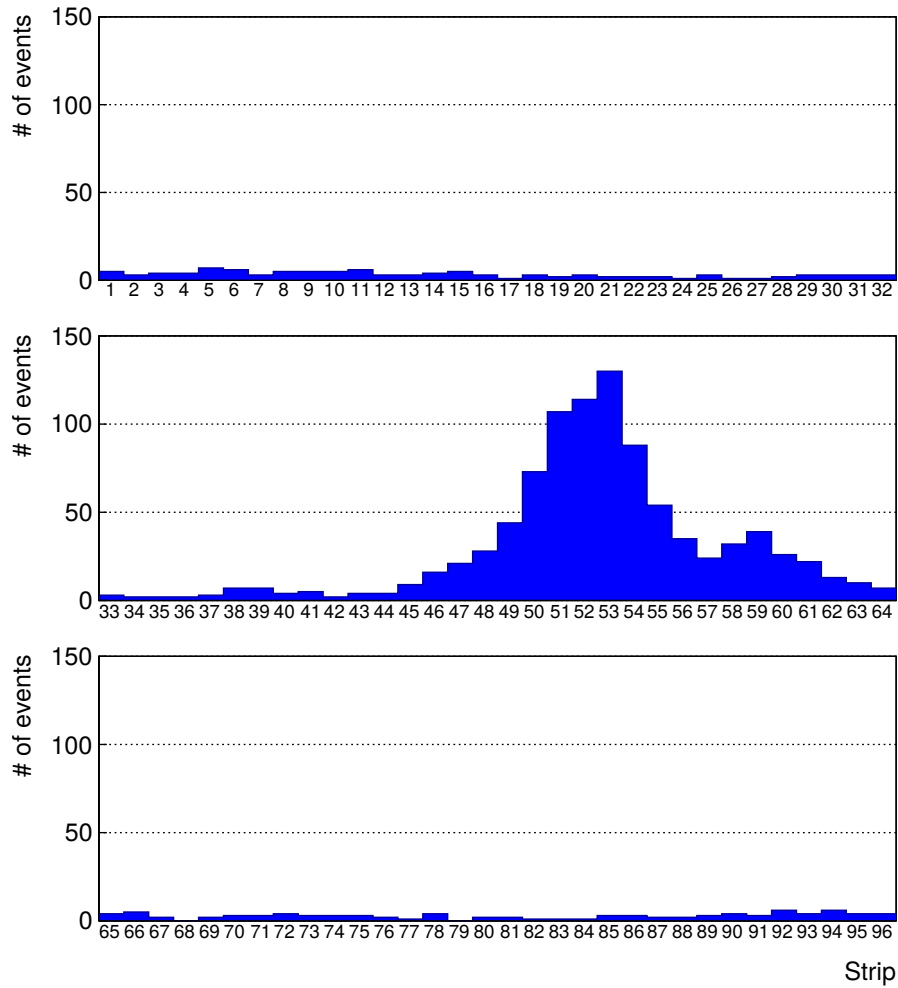


Figure 4.11: Hit distributions over all 3 partitions of RE-4-2-BARC-161 chamber is showed on these plots. Top, middle and bottom figures respectively correspond to partitions A, B, and C. These plots show that some events still occur in other half-partitions than B2, which corresponds to strips 49 to 64, in front of which the trigger is placed, contributing to the inefficiency of detection of cosmic muons. In the case of partitions A and C, the very low amount of data can be interpreted as noise. On the other hand, it is clear that a little portion of muons reach the half-partition B1, corresponding to strips 33 to 48.

1208 **4.3.2 Data Acquisition**

1209 **4.3.3 Geometrical acceptance of the setup layout to cosmic muons**

1210 In order to profit from a constant gamma irradiation, the detectors inside of the GIF bunker need
 1211 to be placed in a plane orthogonal to the beam line. The muon beam that used to be available was
 1212 meant to test the performance of detectors under test. This beam not being active anymore, another
 1213 solution to test detector performance had to be used. Thus, it has been decided to use cosmic muons
 1214 detected through a telescope composed of two scintillators. Lead blocks were used as shielding to

protect the photomultipliers from gammas as can be seen from Figure 4.10.

An inclination has been given to the cosmic telescope to maximize the muon flux. A good compromise had to be found between good enough muon flux and narrow enough hit distribution to be sure to contain all the events into only one half partitions as required from the limited available readout hardware. Nevertheless, a consequence of the misplaced trigger, that can be seen as a loss of events in half-partition B1 in Figure 4.11, is an inefficiency. Nevertheless, the inefficiency of approximately 20 % highlighted in Figure 4.12 by comparing the performance of chamber BARC-161 in 904 and at GIF without irradiation seems too important to be explained only by the geometrical acceptance of the setup itself. Simulations have been conducted to show how the setup brings inefficiency.

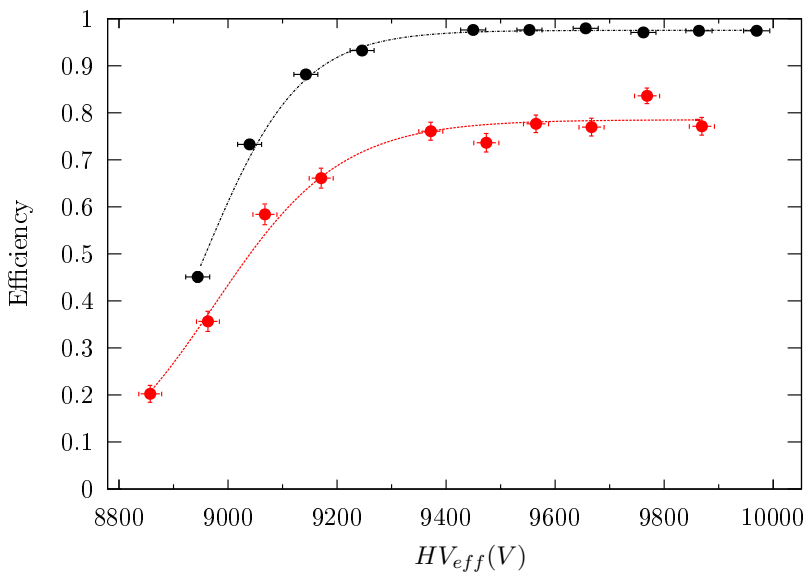


Figure 4.12: Results are derived from data taken on half-partition B2 only. On the 18th of June 2014, data has been taken on chamber RE-2-BARC-161 at building 904 (Prevessin Site) with cosmic muons providing us a reference efficiency plateau of $(97.54 \pm 0.15)\%$ represented by a black curve. A similar measurement has been done at GIF on the 21st of July with the same chamber giving a plateau of $(78.52 \pm 0.94)\%$ represented by a red curve.

4.3.3.1 Description of the simulation layout

The layout of GIF setup has been reproduced and incorporated into a Monte Carlo (MC) simulation to study the influence of the disposition of the telescope on the final distribution measured by the RPC. A 3D view of the simulated layout is given into Figure 4.13. Muons are generated randomly in a horizontal plane located at a height corresponding to the lowest point of the PMTs. This way, the needed size of the plane in order to simulate events happening at very big azimuthal angles (i.e. $\theta \approx \pi$) can be kept relatively small. The muon flux is designed to follow the usual $\cos^2\theta$ distribution for cosmic particle. The goal of the simulation is to look at muons that pass through the muon telescope composed of the two scintillators and define their distribution onto the RPC plane. During the reconstruction, the RPC plane is then divided into its strips and each muon track is assigned to a strip.

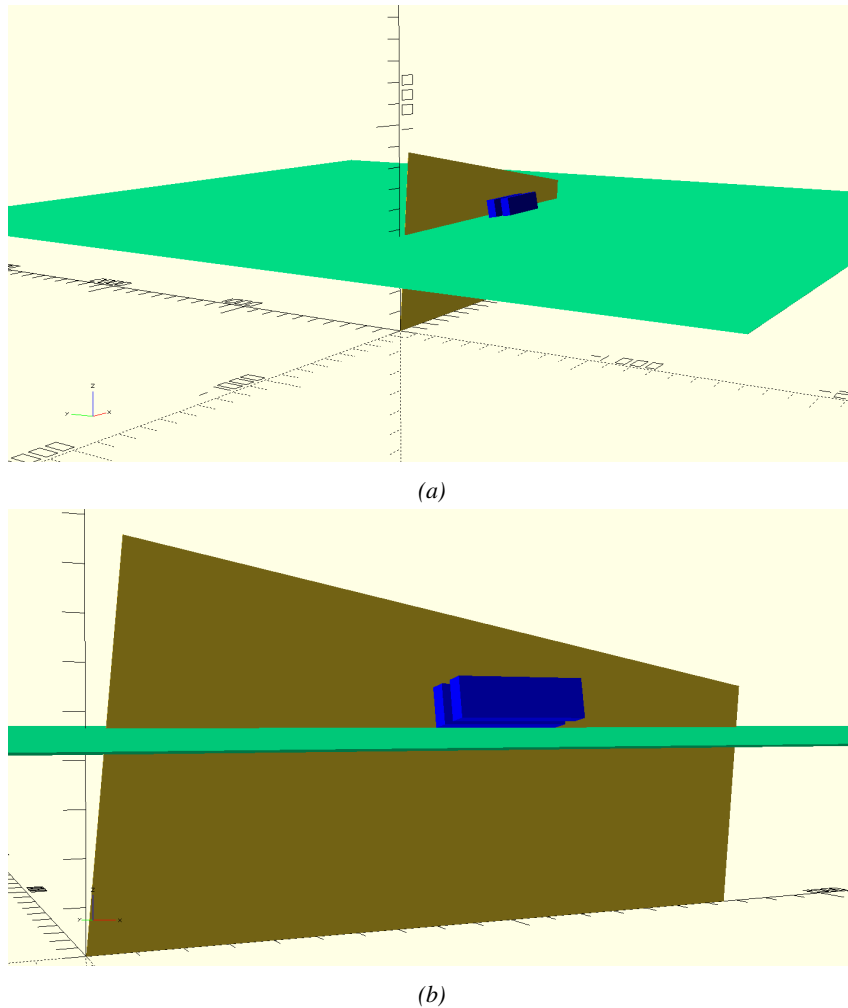


Figure 4.13: Representation of the layout used for the simulations of the test setup. The RPC is represented as a yellow trapezoid while the two scintillators as blue cuboids looking at the sky. A green plane corresponds to the muon generation plane within the simulation. Figure 4.9a shows a global view of the simulated setup. Figure 4.9b shows a zoomed view that allows to see the 2 scintillators as well as the full RPC plane.

1236 In order to further refine the quality of the simulation and understand deeper the results the
 1237 dependance of the distribution has been studied for a range of telescope inclinations. Moreover,
 1238 the threshold applied on the PMT signals has been included into the simulation in the form of a
 1239 cut. In the approximation of uniform scintillators, it has been considered that the threshold can be
 1240 understood as the minimum distance particles need to travel through the scintillating material to give
 1241 a strong enough signal. Particles that travel a distance smaller than the set "threshold" are thus not
 1242 detected by the telescope and cannot trigger the data taking. Finally, the FEE threshold also has
 1243 been considered in a similar way. The mean momentum of horizontal cosmic rays is higher than
 1244 those of vertical ones but the stopping power of matter for momenta ranging from 1 GeV to 1 TeV
 1245 stays comparable. It is then possible to assume that the mean number of primary e^- /ion pairs per
 1246 unit length will stay similar and thus, depending on the applied discriminator threshold, muons with

1247 the shortest path through the gas volume will deposit less charge and induce a smaller signal on the
 1248 pick-up strips that could eventually not be detected. These two thresholds also restrain the overall
 1249 geometrical acceptance of the system.

1250 **4.3.3.2 Simulation procedure**

1251 The simulation software has been designed using C++ and the output data is saved into ROOT
 1252 histograms. Simulations start for a threshold T_{scint} varying in a range from 0 to 45 mm in steps
 1253 of 5 mm, where $T_{scint} = 0$ mm corresponds to the case where there isn't any threshold apply on
 1254 the input signal while $T_{scint} = 45$ mm, which is the scintillator thickness, is the case where muons
 1255 cannot arrive orthogonally onto the scintillator surface. For a given T_{scint} , a set of RPC thresholds
 1256 are considered. The RPC threshold, T_{RPC} varies from 2 mm, the thickness of the gas volume, to
 1257 3 mm in steps of 0.25 mm. For each $(T_{scint}; T_{RPC})$ pair, $N_\mu = 10^8$ muons are randomly generated
 1258 inside the muon plane described in the previous paragraph with an azimuthal angle θ chosen to follow
 1259 a $\cos^2\theta$ distribution.

1260 Planes are associated to each surface of the scintillators. Knowing muon position into the muon
 1261 plane and its direction allows us, by assuming that muons travel in a straight line, to compute the
 1262 intersection of the muon track with these planes. Applying conditions to the limits of the surfaces
 1263 of the scintillator faces then gives us an answer to whether or not the muon passed through the
 1264 scintillators. In the case the muon has indeed passed through the telescope, the path through each
 1265 scintillator is computed and muons whose path was shorter than T_{scint} are rejected and are thus
 1266 considered as having not interacted with the setup.

1267 On the contrary, if the muon is labeled as good, its position within the RPC plane is computed
 1268 and the corresponding strip, determined by geometrical tests in the case the distance through the
 1269 gas volume was enough not to be rejected because of T_{RPC} , gets a hit and several histograms
 1270 are filled in order to keep track of the generation point on the muon plane, the intersection points
 1271 of the reconstructed muons within the telescope, or on the RPC plane, the path traveled through
 1272 each individual scintillator or the gas volume, as well as other histograms. Moreover, muons fill
 1273 different histograms whether they are forward or backward coming muons. They are discriminated
 1274 according to their direction components. When a muon is generated, an (x, y, z) position is assigned
 1275 into the muon plane as well as a $(\theta; \phi)$ pair that gives us the direction it's coming from. This way,
 1276 muons satisfying the condition $0 \leq \phi < \pi$ are designated as backward coming muons while muons
 1277 satisfying $\pi \leq \phi < 2\pi$ as forward coming muons.

1278 This simulation is then repeated for different telescope inclinations ranging in between 4 and 20°
 1279 and varying in steps of 2° . Due to this inclination and to the vertical position of the detector under
 1280 test, the muon distribution reconstructed in the detector plane is asymmetrical. The choice as been
 1281 made to chose a skew distribution formula to fit the data built as the multiplication of gaussian and
 1282 sigmoidal curves together. A typical gaussian formula is given as 4.1 and has three free parameters
 1283 as A_g , its amplitude, \bar{x} , its mean value and σ , its root mean square. Sigmoidal curves as given by
 1284 formula 4.2 are functions converging to 0 and A_s as x diverges. The inflection point is given as x_i
 1285 and λ is proportional to the slope at $x = x_i$. In the limit where $\lambda \rightarrow \infty$, the sigmoid becomes a
 1286 step function.

$$g(x) = A_g e^{-\frac{(x-\bar{x})^2}{2\sigma^2}} \quad (4.1)$$

$$s(x) = \frac{A_s}{1 + e^{-\lambda(x-x_i)}} \quad (4.2)$$

Finally, a possible representation of a skew distribution is given by formula 4.3 and is the product of 4.1 and 4.2. Naturally, here $A_{sk} = A_g \times A_s$ and represents the theoretical maximum in the limit where the skew tends to a gaussian function.

$$sk(x) = g(x) \times s(x) = A_{sk} \frac{e^{\frac{-(x-\bar{x})^2}{2\sigma^2}}}{1 + e^{-\lambda(x-x_i)}} \quad (4.3)$$

4.3.3.3 Results

Influence of T_{scint} on the muon distribution

Influence of T_{RPC} on the muon distribution

Influence of the telescope inclination on the muon distribution

Comparison to data taken at GIF without irradiation

4.3.4 Photon flux at GIF

4.3.4.1 Expectations from simulations

In order to understand and evaluate the γ flux in the GIF area, simulations had been conducted in 1999 and published by S. Agosteo et al [55]. Table 4.1 presented in this article gives us the γ flux for different distances D to the source. This simulation was done using GEANT and a Monte Carlo N-Particle (MCNP) transport code, and the flux F is given in number of γ per unit area and unit time along with the estimated error from these packages expressed in %.

Nominal ABS	Photon flux F [$s^{-1}cm^{-2}$]			
	at $D = 50$ cm	at $D = 155$ cm	at $D = 300$ cm	at $D = 400$ cm
1	$0.12 \cdot 10^8 \pm 0.2\%$	$0.14 \cdot 10^7 \pm 0.5\%$	$0.45 \cdot 10^6 \pm 0.5\%$	$0.28 \cdot 10^6 \pm 0.5\%$
2	$0.68 \cdot 10^7 \pm 0.3\%$	$0.80 \cdot 10^6 \pm 0.8\%$	$0.25 \cdot 10^6 \pm 0.8\%$	$0.16 \cdot 10^6 \pm 0.6\%$
5	$0.31 \cdot 10^7 \pm 0.4\%$	$0.36 \cdot 10^6 \pm 1.2\%$	$0.11 \cdot 10^6 \pm 1.2\%$	$0.70 \cdot 10^5 \pm 0.9\%$

Table 4.1: Total photon flux ($E\gamma \leq 662$ keV) with statistical error predicted considering a ^{137}Cs activity of 740 GBq at different values of the distance D to the source along the x -axis of irradiation field [55].

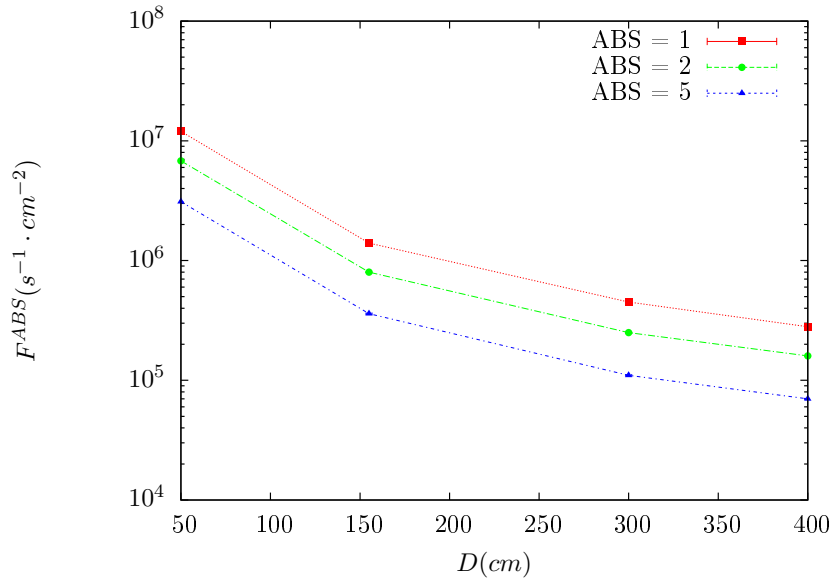


Figure 4.14: γ flux $F(D)$ is plot using values from table 4.1. As expected, the plot shows similar attenuation behaviours with increasing distance for each absorption factors.

The simulation doesn't directly provide us with an estimated flux at the level of our RPC. First of all, it is needed to extract the value of the flux from the available data contained in the original paper and then to estimate the flux in 2014 at the time the experimentation took place. Figure 4.14 that contains the data from Table 4.1. In the case of a pointlike source emitting isotropic and homogeneous gamma radiations, the gamma flux F at a distance D to the source with respect to a reference point situated at D_0 where a known flux F_0 is measured will be expressed like in Equation 4.4, assuming that the flux decreases as $1/D^2$, where c is a fitting factor.

$$F^{ABS} = F_0^{ABS} \times \left(\frac{cD_0}{D} \right)^2 \quad (4.4)$$

By rewriting Equation 4.4, it comes that :

$$c = \frac{D}{D_0} \sqrt{\frac{F^{ABS}}{F_0^{ABS}}} \quad (4.5)$$

$$\Delta c = \frac{c}{2} \left(\frac{\Delta F^{ABS}}{F^{ABS}} + \frac{\Delta F_0^{ABS}}{F_0^{ABS}} \right) \quad (4.6)$$

Finally, using Equation 4.5 and the data in Table 4.1 with $D_0 = 50$ cm as reference point, we can build Table 4.2. It is interesting to note that c for each value of D doesn't depend on the absorption factor.

Nominal ABS	Correction factor c		
	at $D = 155$ cm	at $D = 300$ cm	at $D = 400$ cm
1	$1.059 \pm 0.70\%$	$1.162 \pm 0.70\%$	$1.222 \pm 0.70\%$
2	$1.063 \pm 1.10\%$	$1.150 \pm 1.10\%$	$1.227 \pm 0.90\%$
5	$1.056 \pm 1.60\%$	$1.130 \pm 1.60\%$	$1.202 \pm 1.30\%$

Table 4.2: Correction factor c is computed thanks to formulae 4.5 taking as reference $D_0 = 50$ cm and the associated flux F_0^{ABS} for each absorption factor available in table 4.1.

1313 For the range of D/D_0 values available, it is possible to use a simple linear fit to get the evolution
 1314 of c . The linear fit will then use only 2 free parameters, a and b , as written in Equation 4.7. This gives
 1315 us the results showed in Figure 4.15. Figure 4.15b confirms that using only a linear fit to extract c is
 1316 enough as the evolution of the rate that can be obtained superimposes well on the simulation points.

$$c \left(\frac{D}{D_0} \right) = a \frac{D}{D_0} + b \quad (4.7)$$

$$F^{ABS} = F_0^{ABS} \left(a + \frac{b D_0}{D} \right)^2 \quad (4.8)$$

$$\Delta F^{ABS} = F^{ABS} \left[\frac{\Delta F_0^{ABS}}{F_0^{ABS}} + 2 \frac{\Delta a + \Delta b \frac{D_0}{D}}{a + \frac{b D_0}{D}} \right] \quad (4.9)$$

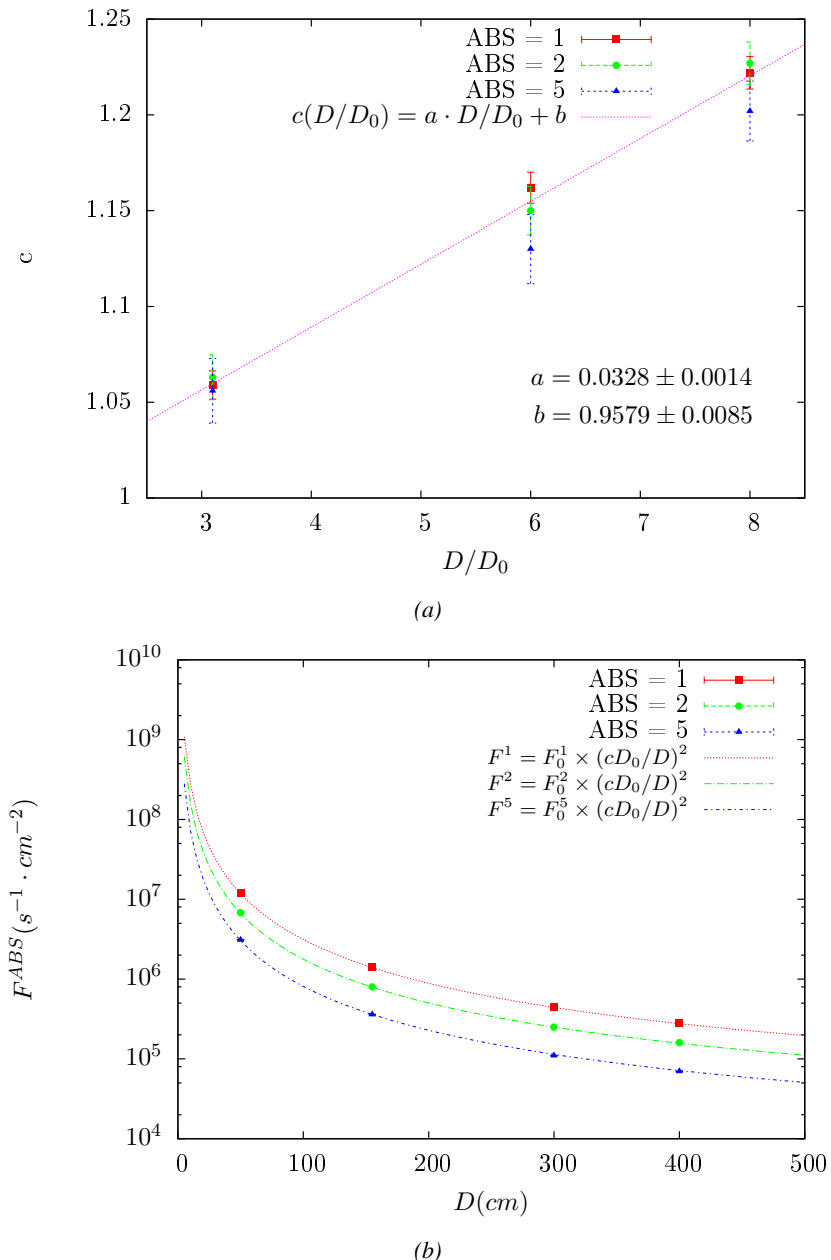


Figure 4.15: Figure 4.15a shows the linear approximation fit done via formulae 4.7 on data from table 4.2. Figure 4.15b shows a comparison of this model with the simulated flux using a and b given in figure 4.15a in formulae 4.4 and the reference value $D_0 = 50\text{cm}$ and the associated flux for each absorption factor F_0^{ABS} from table 4.1

In the case of the 2014 GIF tests, the RPC plane is located at a distance $D = 206$ cm to the source. Moreover, to estimate the strength of the flux in 2014, it is necessary to consider the nuclear decay through time associated to the Cesium source whose half-life is well known ($t_{1/2} = (30.05 \pm 0.08)$ y). The very first source activity measurement has been done on the 5th of March 1997 while the GIF

1321 tests where done in between the 20th and the 31st of August 2014, i.e. at a time $t = (17.47 \pm 0.02)$ y
 1322 resulting in an attenuation of the activity from 740 GBq in 1997 to 494 GBq in 2014. All the needed
 1323 information to extrapolate the flux through our detector in 2014 has now been assembled, leading
 1324 to the Table 4.3. It is interesting to note that for a common RPC sensitivity to γ of $2 \cdot 10^{-3}$, the
 1325 order of magnitude of the estimated hit rate per unit area is of the order of the kHz for the fully
 1326 opened source. Moreover, taking profit of the two working absorbers, it will be possible to scan
 1327 background rates at 0 Hz, ~ 300 Hz as well as ~ 600 Hz. Without source, a good estimate of the
 1328 intrinsic performance will be available. Then at 300 Hz, the goal will be to show that the detectors
 1329 fulfill the performance certification of CMS RPCs. Then a first idea of the performance of the
 1330 detectors at higher background will be provided with absorption factors 2 (~ 600 Hz) and 1 (no
 1331 absorption). *[Here I will also put a reference to the plot showing the estimated background rate at
 1332 the level of RE3/1 in the case of HL-LHC but this one being in another chapter, I will do it later.]*

Nominal ABS	Photon flux F [$s^{-1}cm^{-2}$]			Hit rate/unit area [$Hz cm^{-2}$] at $D^{2014} = 206$ cm
	at $D_0^{1997} = 50$ cm	at $D^{1997} = 206$ cm	at $D^{2014} = 206$ cm	
1	$0.12 \cdot 10^8 \pm 0.2\%$	$0.84 \cdot 10^6 \pm 0.3\%$	$0.56 \cdot 10^6 \pm 0.3\%$	1129 ± 32
2	$0.68 \cdot 10^7 \pm 0.3\%$	$0.48 \cdot 10^6 \pm 0.3\%$	$0.32 \cdot 10^6 \pm 0.3\%$	640 ± 19
5	$0.31 \cdot 10^7 \pm 0.4\%$	$0.22 \cdot 10^6 \pm 0.3\%$	$0.15 \cdot 10^6 \pm 0.3\%$	292 ± 9

Table 4.3: The data at D_0 in 1997 is taken from [55]. In a second step, using Equations 4.8 and 4.9, the flux at D can be estimated in 1997. Then, taking into account the attenuation of the source activity, the flux at D can be estimated at the time of the tests in GIF in 2014. Finally, assuming a sensitivity of the RPC to γ $s = 2 \cdot 10^{-3}$, an estimation of the hit rate per unit area is obtained.

1333 **4.3.4.2 Dose measurements**

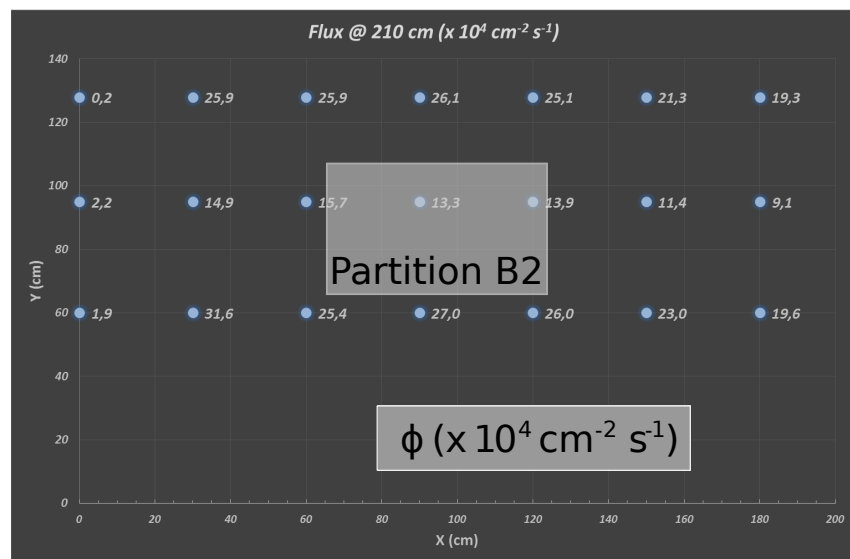


Figure 4.16: Dose measurements has been done in a plane corresponding to the tents front side. This plan is 1900 mm away from the source. As explained in the first chapter, a lens-shaped lead filter provides a uniform photon flux in the vertical plan orthogonal to the beam direction. If the second line of measured fluxes is not taken into account because of lower values due to experimental equipments in the way between the source and the tent, the uniformity of the flux is well showed by the results.

¹³³⁴ **4.3.5 Results and discussions**

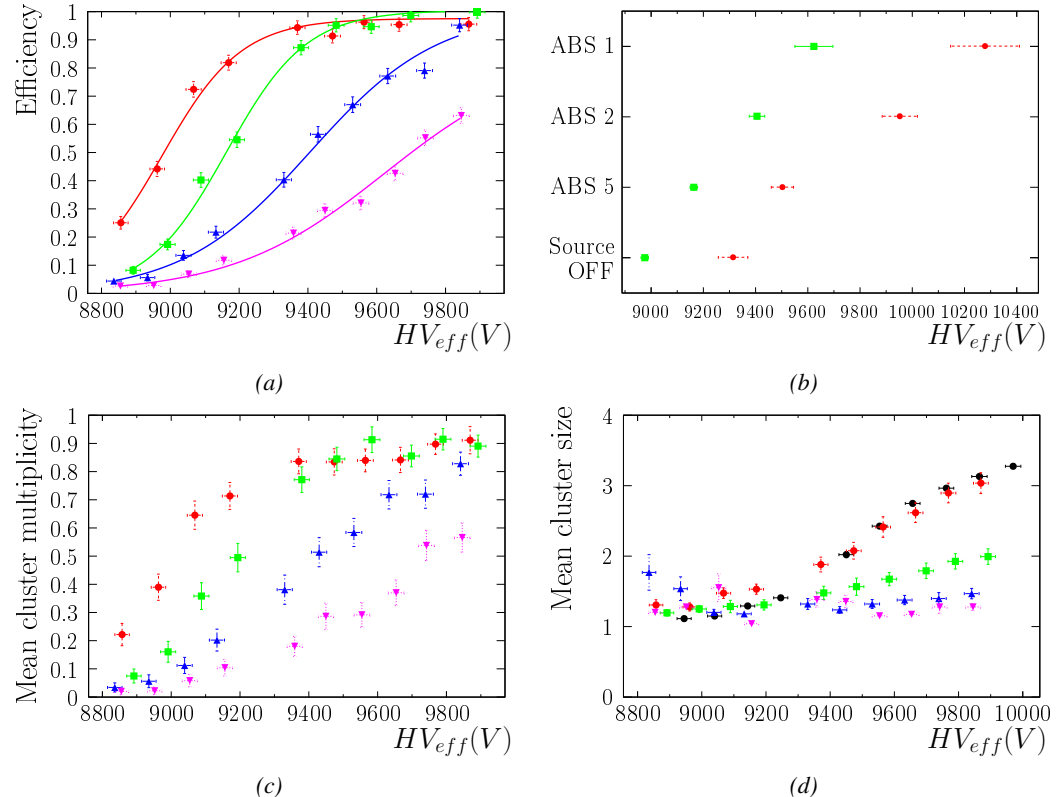


Figure 4.17

¹³³⁵ 4.4 Longevity tests at GIF++

¹³³⁶ Longevity studies imply a monitoring of the performance of the detectors probed using a high inten-
¹³³⁷ sity muon beam in a irradiated environment by periodically measuring their rate capability, the dark
¹³³⁸ current running through them and the bulk resistivity of the Bakelite composing their electrodes.
¹³³⁹ GIF++, with its very intense ^{137}Cs source, provides the perfect environment to perform such kind
¹³⁴⁰ of tests. Assuming a maximum acceleration factor of 3, it is expected to accumulate the equivalent
¹³⁴¹ charge in 1.7 years.

¹³⁴² As the maximum background is found in the endcap, the choice naturally was made to focus the
¹³⁴³ GIF++ longevity studies on endcap chambers. Most of the RPC system was installed in 2007. Nev-
¹³⁴⁴ ertheless, the large chambers in the fourth endcap (RE4/2 and RE4/3) have been installed during
¹³⁴⁵ LS1 in 2014. The Bakelite of these two different productions having different properties, four spare
¹³⁴⁶ chambers of the present system were selected, two RE2,3/2 spares and two RE4/2 spares. Having
¹³⁴⁷ two chambers of each type allows to always keep one of them non irradiated as reference, the per-
¹³⁴⁸ formance evolution of the irradiated chamber being then compared through time to the performance
¹³⁴⁹ of the non irradiated one.

¹³⁵⁰ The performance of the detectors under different level of irradiation is measured periodically dur-
¹³⁵¹ ing dedicated test beam periods using the H4 muon beam. In between these test beam periods, the
¹³⁵² two RE2,3/2 and RE4/2 chambers selected for this study are irradiated by the ^{137}Cs source in order
¹³⁵³ to accumulate charge and the gamma background is monitored, as well as the currents. The two
¹³⁵⁴ remaining chambers are kept non-irradiated as reference detectors. Due to the limited gas flow in
¹³⁵⁵ GIF++, the RE4 chamber remained non-irradiated until end of November 2016 where a new mass
¹³⁵⁶ flow controller has been installed allowing for bigger volumes of gas to flow in the system.

¹³⁵⁷ Figures 4.18 and 4.19 give us for different test beam periods, and thus for increasing integrated
¹³⁵⁸ charge through time, a comparison of the maximum efficiency, obtained using a sigmoid-like func-
¹³⁵⁹ tion, and of the working point of both irradiated and non irradiated chambers [**SIGMOID2005**]. No
¹³⁶⁰ aging is yet to see from this data, the shifts in γ rate per unit area in between irradiated and non
¹³⁶¹ irradiated detectors and RE2 and RE4 types being easily explained by a difference of sensitivity due
¹³⁶² to the various Bakelite resistivities of the HPL electrodes used for the electrode production.

¹³⁶³ Collecting performance data at each test beam period allows us to extrapolate the maximum effi-
¹³⁶⁴ ciency for a background hit rate of 300 Hz/cm^2 corresponding to the expected HL-LHC conditions.
¹³⁶⁵ Aging effects could emerge from a loss of efficiency with increasing integrated charge over time,
¹³⁶⁶ thus Figure 4.20 helps us understand such degradation of the performance of irradiated detectors in
¹³⁶⁷ comparison with non irradiated ones. The final answer for an eventual loss of efficiency is given in
¹³⁶⁸ Figure 4.21 by comparing for both irradiated and non irradiated detectors the efficiency sigmoids
¹³⁶⁹ before and after the longevity study. Moreover, to complete the performance information, the Bake-
¹³⁷⁰ lite resistivity is regularly measured thanks to Ag scans (Figure 4.22) and the noise rate is monitored
¹³⁷¹ weekly during irradiation periods (Figure 4.23). At the end of 2016, no signs of aging were observed
¹³⁷² and further investigation is needed to get closer to the final integrated charge requirements proposed
¹³⁷³ for the longevity study of the present CMS RPC sub-system.

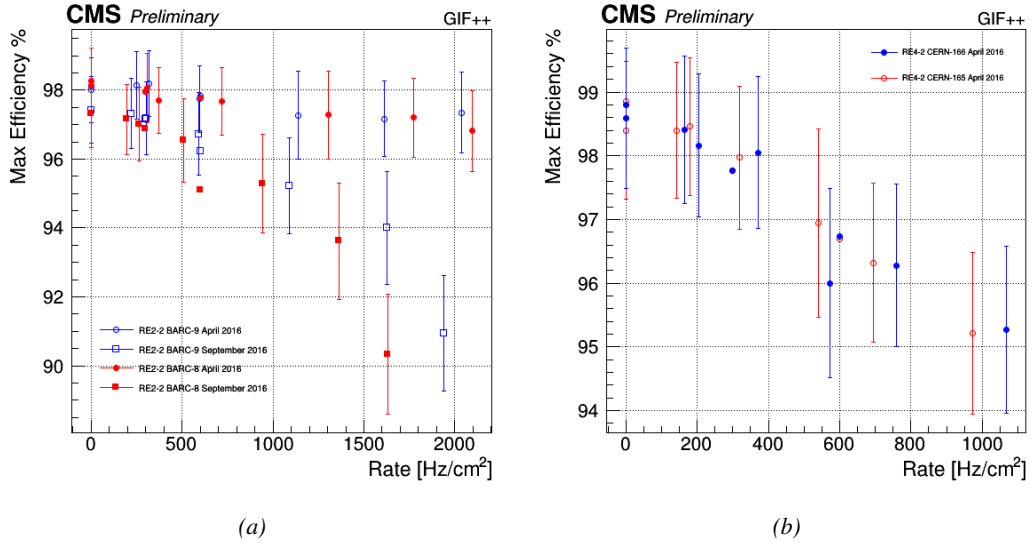


Figure 4.18: Evolution of the maximum efficiency for RE2 (4.18a) and RE4 (4.18b) chambers with increasing extrapolated γ rate per unit area at working point. Both irradiated (blue) and non irradiated (red) chambers are shown.

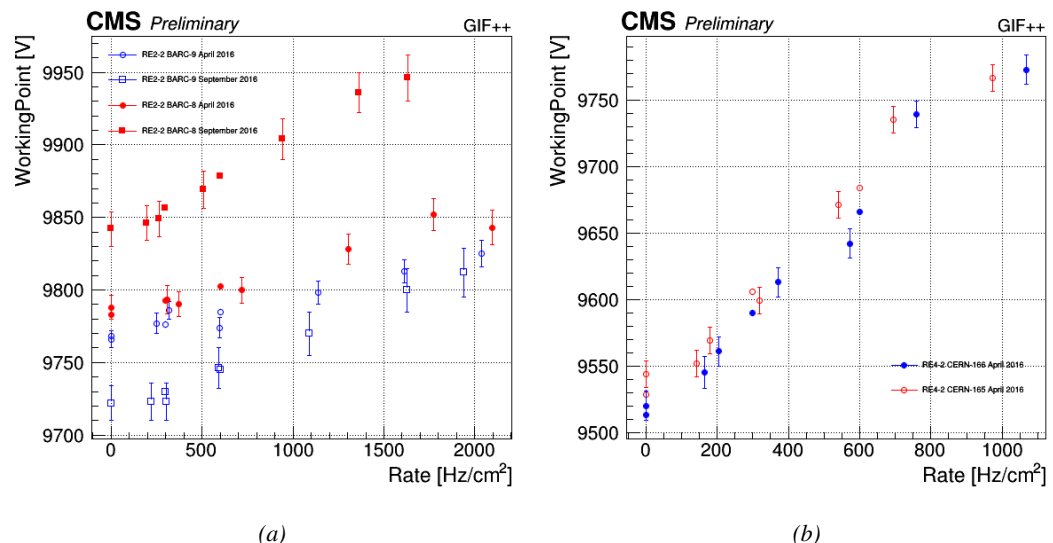


Figure 4.19: Evolution of the working point for RE2 (4.19a) and RE4 (4.19b) with increasing extrapolated γ rate per unit area at working point. Both irradiated (blue) and non irradiated (red) chambers are shown.

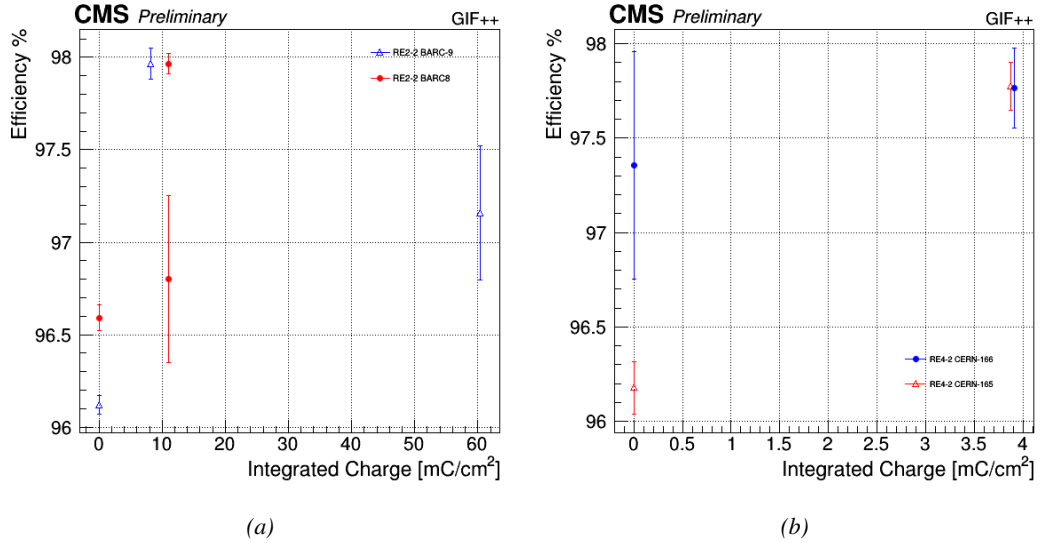


Figure 4.20: Evolution of the maximum efficiency at HL-LHC conditions, i.e. a background hit rate per unit area of 300 Hz/cm², with increasing integrated charge for RE2 (4.20a) and RE4 (4.20b) detectors. Both irradiated (blue) and non irradiated (red) chambers are shown. The integrated charge for non irradiated detectors is recorded during test beam periods and stays small with respect to the charge accumulated in irradiated chambers.

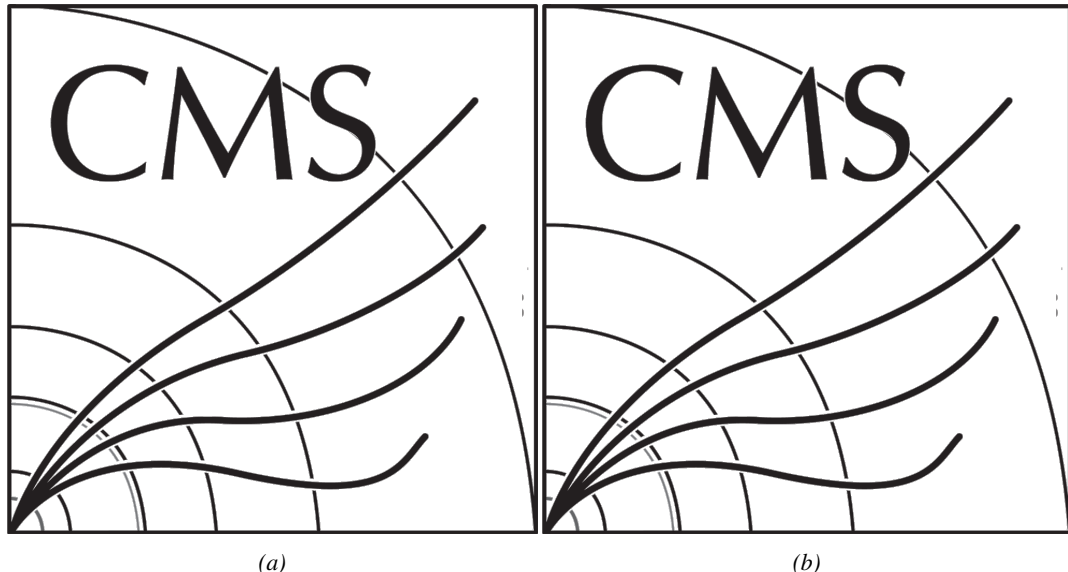


Figure 4.21: Comparison of the efficiency sigmoid before (triangles) and after (circles) irradiation for RE2 (4.21a) and RE4 (4.21b) detectors. Both irradiated (blue) and non irradiated (red) chambers are shown.

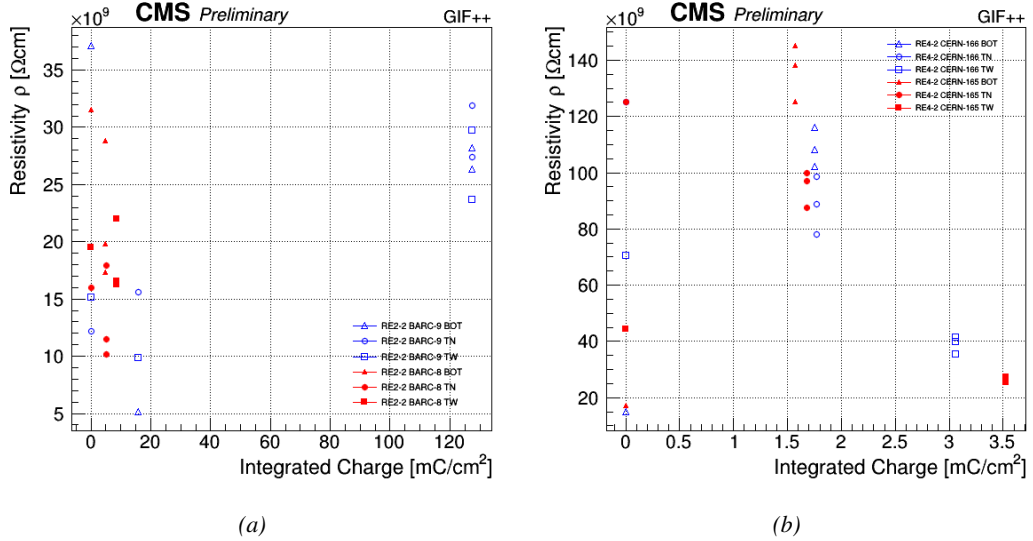


Figure 4.22: Evolution of the Bakelite resistivity for RE2 (4.22a) and RE4 (4.22b) detectors. Both irradiated (blue) and non-irradiated (red) chambers are shown.

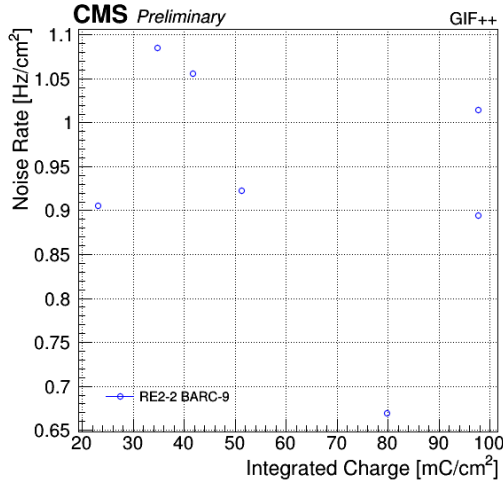


Figure 4.23: Evolution of the noise rate per unit area for the irradiated chamber RE2-2-BARC-9 only.

4.4.1 Description of the Data Acquisition

For the longevity studies, four spare chambers of the present system are used. Two spare RPCs of the RE2,3 stations as well as two spare RPCs from the new RE4 stations have been mounted in a Trolley. Six RE4 gaps are also placed in the trolley. The trolley is placed inside the GIFT++ in the upstream region of the bunker, taking the cesium source as a reference. The trolley is oriented for the detection surface of the chambers to be orthogonal to the beam line. The system can be moved along the orthogonal plane in order to have the beam in all η -partitions. For the aging the trolley is

1382 moved outside the beam line and is placed in a distance of 5.2 m to the source, which irradiates the
 1383 bunker using an attenuation filter of 2.2 which corresponds to a fluence of 10^7 gamma/cm^2 .

1384 During GIF++ operation, the data collected can be divided into different categories as several
 1385 parameters are monitored in addition to the usual RPC performance data. On one hand, to know
 1386 the performance of a chamber, it is need to measure its efficiency and to know the background
 1387 conditions in which it is operated. To do this, the hit signals from the chamber are recorded and
 1388 stored in a ROOT file via a Data Acquisition (DAQ) software. On the other hand, it is also very
 1389 important to monitor parameters such as environmental pressure and temperature, gas temperature
 1390 and humidity, RPC HV, LV, and currents, or even source and beam status. This is done through the
 1391 GIF++ web Detector Control Software (DCS) that stores this information in a database.

1392 Two different types of tests are conducted on RPCs via the DAQ. Indeed, the performance of the
 1393 detectors is measured periodically during dedicated test beam periods using the H4 muon beam. In
 1394 between these test beam periods, when the beam is not available, the chambers are irradiated by the
 1395 ^{137}Cs in order to accumulate deposited charge and the gamma background is measured.

1396 RPCs under test are connected through LVDS cables to V1190A Time-to-Digital Converter
 1397 (TDC) modules manufactured by CAEN. These modules, located in the rack area outside of the
 1398 bunker, get the logic signals sent by the chambers and save them into their buffers. Due to the
 1399 limited size of the buffers, the collected data is regularly erased and replaced. A trigger signal is
 1400 needed for the TDC modules to send the useful data to the DAQ computer via a V1718 CAEN USB
 1401 communication module.

1402 In the case of performance test, the trigger signal used for data acquisition is generated by the
 1403 coincidence of three scintillators. A first one is placed upstream outside of the bunker, a second one
 1404 is placed downstream outside of the bunker, while a third one is placed in front of the trolley, close by
 1405 the chambers. Every time a trigger is sent to the TDCs, i.e. every time a muon is detected, knowing
 1406 the time delay in between the trigger and the RPC signals, signals located in the right time window
 1407 are extracted from the buffers and saved for later analysis. Signals are taken in a time window of
 1408 400 ns centered on the muon peak (here we could show a time spectrum). On the other hand, in the
 1409 case of background rate measurement, the trigger signal needs to be "random" not to measure muons
 1410 but to look at gamma background. A trigger pulse is continuously generated at a rate of 300 Hz using
 1411 a dual timer. To integrate an as great as possible time, all signals contained within a time window of
 1412 10us prior to the random trigger signal are extracted form the buffers and saved for further analysis
 1413 (here another time spectrum to illustrate could be useful, maybe even place both spectrum together
 1414 as a single Figure).

1415 The signals sent to the TDCs correspond to hit collections in the RPCs. When a particle hits
 1416 a RPC, it induce a signal in the pickup strips of the RPC readout. If this signal is higher than the
 1417 detection threshold, a LVDS signal is sent to the TDCs. The data is then organised into 4 branches
 1418 keeping track of the event number, the hit multiplicity for the whole setup, and the time and channel
 1419 profile of the hits in the TDCs.

1420 4.4.2 RPC current, environmental and operation parameter monitoring

1421 In order to take into account the variation of pressure and temperature between different data taking
 1422 periods the applied voltage is corrected following the relationship :

$$1423 HV_{eff} = HV_{app} \times \left(0.2 + 0.8 \cdot \frac{P_0}{P} \times \frac{T}{T_0} \right) \quad (4.10)$$

¹⁴²³ where T_0 (=293 K) and P_0 (=990 mbar) are the reference values.

¹⁴²⁴ **4.4.3 Measurement procedure**

¹⁴²⁵ Insert a short description of the online tools (DAQ, DCS, DQM).

¹⁴²⁶ Insert a short description of the offline tools : tracking and efficiency algorithm.

¹⁴²⁷ Identify long term aging effects we are monitoring the rates per strip.

¹⁴²⁸ **4.4.4 Longevity studies results**

5

1429

1430

Investigation on high rate RPCs

1431 **5.1 Rate limitations and ageing of RPCs**

1432 **5.1.1 Low resistivity electrodes**

1433 **5.1.2 Low noise front-end electronics**

1434 **5.2 Construction of prototypes**

1435 **5.3 Results and discussions**

6

Conclusions and outlooks

1436

1437

1438 **6.1 Conclusions**

1439 **6.2 Outlooks**

A

1440

1441

A data acquisition software for CAEN VME TDCs

1442

1443 Certifying detectors in the perspective of HL-LHC required to develop tools for the GIF++ experiment.
1444 Among them was the C++ Data Acquisition (DAQ) software that allows to make the communications
1445 in between a computer and TDC modules in order to retrieve the RPC data [57]. In this
1446 appendix, details about this software, as of how the software was written, how it functions and how
1447 it can be exported to another similar setup, will be given.

1448 A.1 GIF++ DAQ file tree

1449 GIF++ DAQ source code is fully available on github at https://github.com/afagot/GIF_DAQ. The software requires 3 non-optional dependencies:

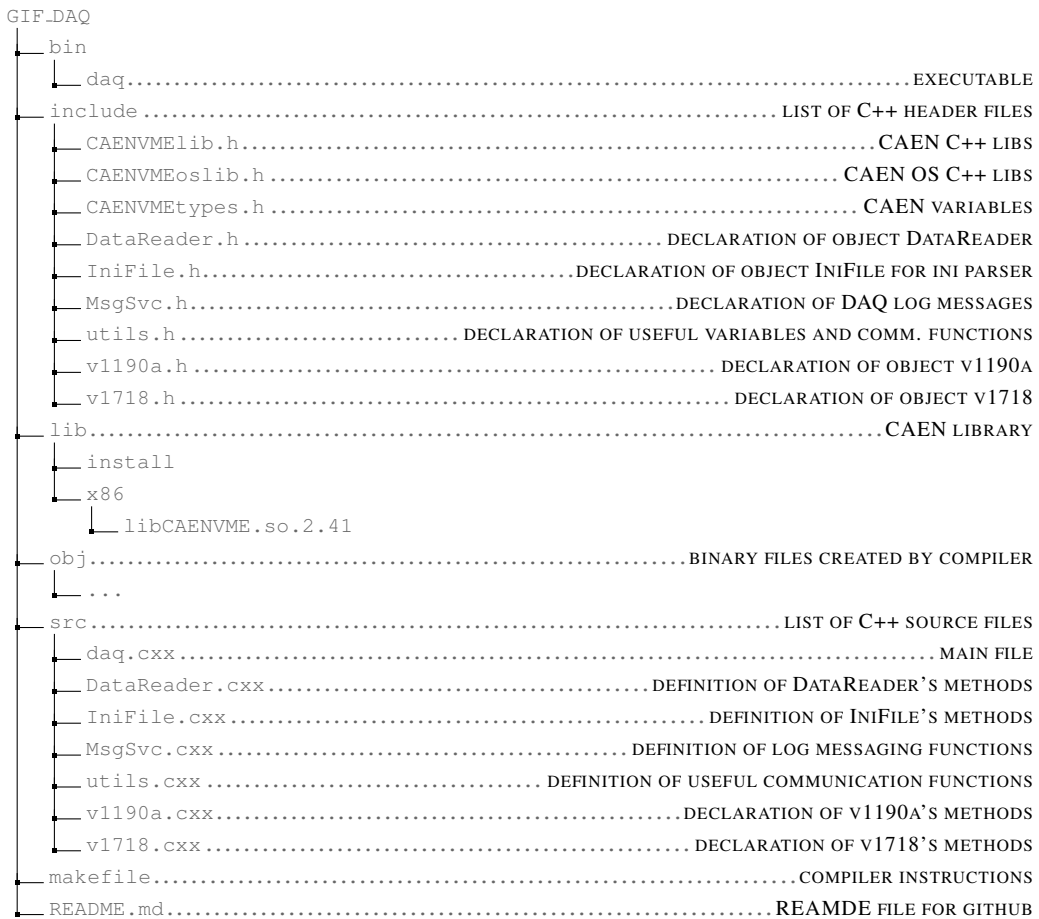
- 1451 • CAEN USB Driver, to mount the VME hardware,
1452 • CAEN VME Library, to communicate with the VME hardware, and
1453 • ROOT, to organize the collected data into a TTree.

1454 The CAEN VME library will not be packaged by distributions and will need to be installed man-
1455 ually. To compile the GIF++ DAQ project via a terminal, from the DAQ folder use the command:

1456 make

1458 The source code tree is provided below along with comments to give an overview of the files' con-
1459 tent. The different objects created for this project (`v1718`, `v1190a`, `IniFile` & `DataReader`) will be
1460 described in details in the following sections.

1461



1462 A.2 Usage of the DAQ

1463 GIF++ DAQ, as used in GIF++, is not a standalone software. Indeed, the system being more complexe,
 1464 the DAQ only is a sub-layer of the software architecture developped to control and monitor
 1465 the RPCs that are placed into the bunker for performance study in an irradiated environment. The top
 1466 layer of GIF++ is a Web Detector Control System (webDCS) application. The DAQ is only called
 1467 by the webDCS when data needs to be acquired. The webDCS operates the DAQ through command
 1468 line. To start the DAQ, the webDCS calls:

1469

1470 bin/daq /path/to/the/log/file/in/the/output/data/folder

1471 where /path/to/the/log/file/in/the/output/data/folder is the only argument required. This
 1472 log file is important for the webDCS as this file contains all the content of the communication of the
 1473 webDCS and the different systems monitored by the webDCS. Its content is constantly displayed
 1474 during data taking for the users to be able to follow the operations. The communication messages
 1475 are normally sent to the webDCS log file via the functions declared in file MsgSvc.h, typically
 1476 MSG_INFO(string message).

1477

1478 A.3 Description of the readout setup

1479 The CMS RPC setup at GIF++ counts 5 V1190A Time-to-Digital Converter (TDC) manufactured
 1480 by CAEN [58]. V1190A are VME units accepting 128 independent Multi-Hit/Multi-Event TDC
 1481 channels whose signals are treated by 4 100 ps high performance TDC chips developed by CERN
 1482 / ECP-MIC Division. The communication between the computer and the TDCs to transfer data is
 1483 done via a V1718 VME master module also manufactured by CAEN and operated from a USB
 1484 port [59]. These VME modules are all hosted into a 6U VME 6021 powered crate manufactured by
 1485 W-Ie-Ne-R than can accommodate up to 21 VME bus cards [60]. These 3 components of the DAQ
 1486 setup are shown in Figure A.1.

1487

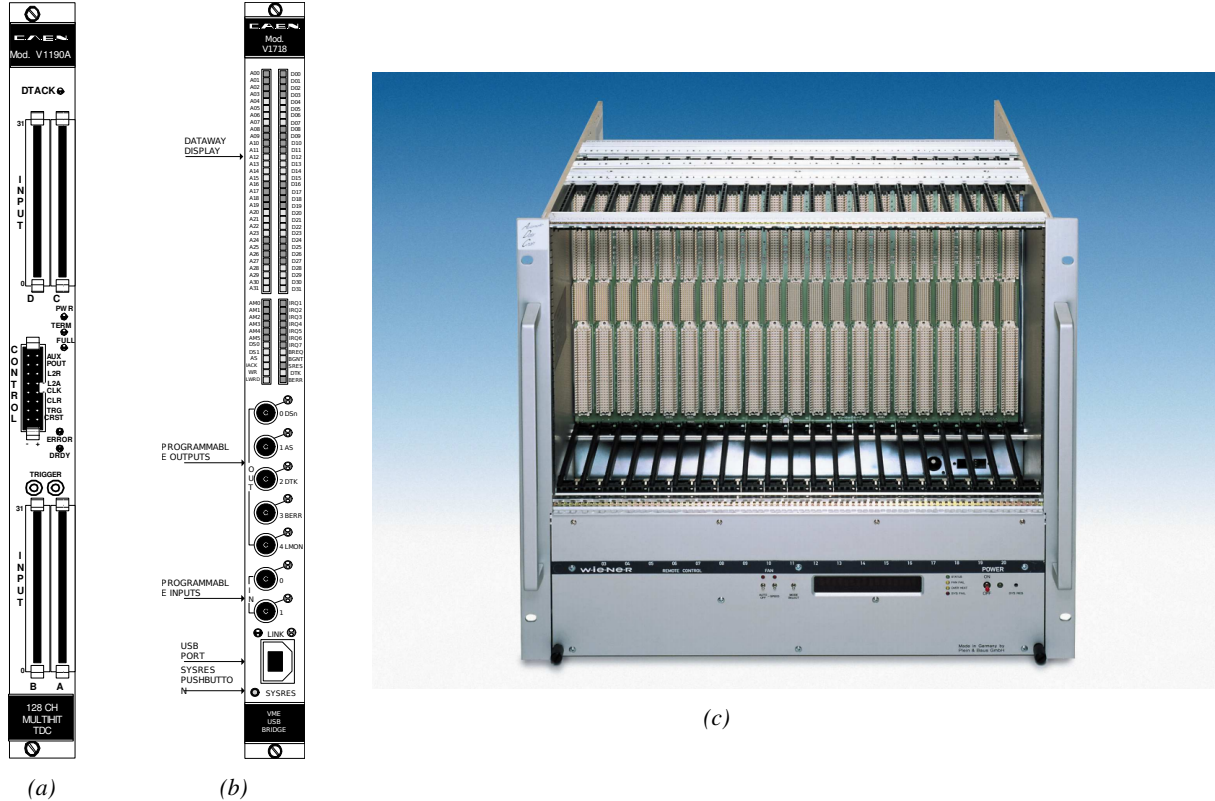


Figure A.1: (A.1a) View of the front panel of a V1190A TDC module [58]. (A.1b) View of the front panel of a V1718 Bridge module [59]. (A.1c) View of the front panel of a 6U 6021 VME crate [60].

1488

A.4 Data read-out

1489 To efficiently perform a data readout algorithm, C++ objects to handle the VME modules (TDCs
 1490 and VME bridge) have been created along with objects to store data and read the configuration file

1491 that comes as an input of the DAQ software.

1492

1493 A.4.1 V1190A TDCs

1494 The DAQ used at GIF takes profit of the *Trigger Matching Mode* offered by V1190A modules.
 1495 This setting is enabled through the method `v1190a::SetTrigMatching (int ntdcs)` where `ntdcs`
 1496 is the total number of TDCs in the setup this setting needs to be enabled for (Source Code A.1). A
 1497 trigger matching is performed in between a trigger time tag, a trigger signal sent into the TRIGGER
 1498 input of the TDC visible on Figure A.1a, and the channel time measurements, signals recorded from
 1499 the detectors under test in our case. Control over this data acquisition mode, explained through
 1500 Figure A.2, is offered via 4 programmable parameters:

- 1501 • **match window:** the matching between a trigger and a hit is done within a programmable time
 1502 window. This is set via the method

1503 `void v1190a::SetTrigWindowWidth(Uint windowHeight, int ntdcs)`

- 1504 • **window offset:** temporal distance between the trigger tag and the start of the trigger matching
 1505 window. This is set via the method

1506 `void v1190a::SetTrigWindowWidth(Uint windowHeight, int ntdcs)`

- 1507 • **extra search margin:** an extended time window is used to ensure that all matching hits are
 1508 found. This is set via the method

1509 `void v1190a::SetTrigSearchMargin(Uint searchMargin, int ntdcs)`

- 1510 • **reject margin:** older hits are automatically rejected to prevent buffer overflows and to speed
 1511 up the search time. This is set via the method

1512 `void v1190a::SetTrigRejectionMargin(Uint rejectMargin, int ntdcs)`

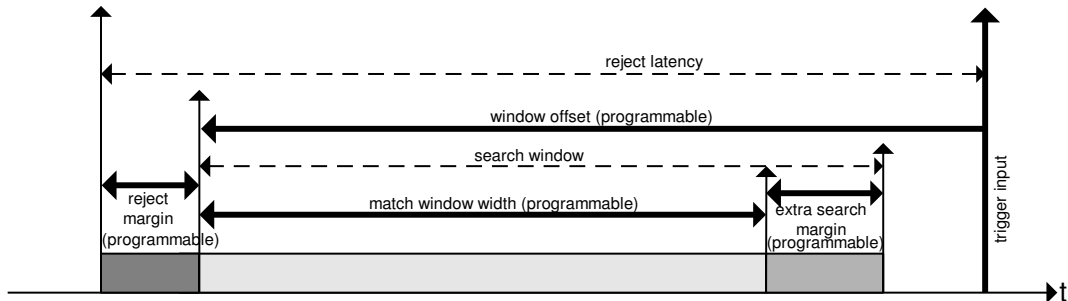


Figure A.2: Module V1190A Trigger Matching Mode timing diagram [58].

1513 Each of these 4 parameters are given in number of clocks, 1 clock being 25 ns long. It is easy to
 1514 understand at this level that there are 3 possible functioning settings:

- 1515 • **1:** the match window is entirely contained after the trigger signal,

- 1516 • **2:** the match window overlaps the trigger signal, or

- 1517 • **3:** the match window is entirely contained before the trigger signal as displayed on Figure A.2.

1518 In both the first and second cases, the sum of the window width and of the offset can be set to
1519 a maximum of 40 clocks, which corresponds to 1 μ s. Evidently, the offset can be negative, allowing
1520 for a longer match window, with the constraint of having the window ending at most 1 μ s after the
1521 trigger signal. In the third case, the maximum negative offset allowed is of 2048 clocks (12 bit) cor-
1522 responding to 51.2 μ s, the match window being strictly smaller than the offset. In the case of GIF++,
1523 the choice has been made to use this last setting by delaying the trigger signal. During the studies
1524 performed in GIF++, both the efficiency of the RPCs, probed using a muon beam, and the noise or
1525 gamma background rate are monitored. The extra search and reject margins are left unused.
1526 To probe the efficiency of RPC detectors, the trigger time tag is provided by the coïncidence of
1527 scintillators when a bunch of muons passes through GIF++ area is used to trigger the data acquisi-
1528 tion. For this measurement, it is useful to reduce the match window width only to contain the muon
1529 information. Indeed, the delay in between a trigger signal and the detection of the corresponding
1530 muon in the RPC being very contant (typically a few tens of ns due to jitter and cable length), the
1531 muon signals are very localised in time. Thus, due to a delay of approximalety 325 ns in between
1532 the muons and the trigger, the settings where chosen to have a window width of 24 clocks (600 ns)
1533 centered on the muon peak thanks to a negative offset of 29 clocks (725 ns).
1534 On the otherhand, monitoring the rates don't require for the DAQ to look at a specific time window.
1535 It is important to integrate enough time to have a robust measurement of the rate as the number of
1536 hits per time unit. The triggerring signal is provided by a pulse generator at a frequency of 300 Hz
1537 to ensure that the data taking occurs in a random way, with respect to beam physics, to probe only
1538 the irradiation spectrum on the detectors. The match window is set to 400 clocks (10 μ s) and the
1539 negative offset to 401 clocks as it needs to exceed the value of the match window.

```

1540
class v1190a
{
    private :
        long             Handle;
        vector<Data32>   Address;
        CVDataWidth      DataWidth;
        CVAddressModifier AddressModifier;

    public:

        v1190a(long handle, IniFile *inifile, int ntdcs);
        ~v1190a();
        Data16 write_op_reg(Data32 address, int code, string error);
        Data16 read_op_reg(Data32 address, string error);
        void Reset(int ntdcs);
        void Clear(int ntdcs);
        void TestWR(Data16 value,int ntdcs);
        void CheckTDCStatus(int ntdcs);
        void CheckCommunication(int ntdcs);
        void SetTDCTestMode(Data16 mode,int ntdcs);
        void SetTrigMatching(int ntdcs);
        void SetTrigTimeSubtraction(Data16 mode,int ntdcs);
        void SetTrigWindowWidth(Uint windowHeight,int ntdcs);
        void SetTrigWindowOffset(Uint windowOffset,int ntdcs);
        void SetTrigSearchMargin(Uint searchMargin,int ntdcs);
        void SetTrigRejectionMargin(Uint rejectMargin,int ntdcs);
        void GetTrigConfiguration(int ntdcs);
        void SetTrigConfiguration(IniFile *inifile,int ntdcs);
        void SetTDCDetectionMode(Data16 mode,int ntdcs);
        void SetTDCResolution(Data16 lsb,int ntdcs);
        void SetTDCDeadTime(Data16 time,int ntdcs);
        void SetTDCHeadTrailer(Data16 mode,int ntdcs);
        void SetTDCEventSize(Data16 size,int ntdcs);
        void SwitchChannels(IniFile *inifile,int ntdcs);
        void SetIRQ(Data32 level, Data32 count,int ntdcs);
        void SetBlockTransferMode(Data16 mode,int ntdcs);
        void Set(IniFile *inifile,int ntdcs);
        void CheckStatus(CVErrorCodes status) const;
        int ReadBlockD32(Uint tdc, const Data16 address,
                         Data32 *data, const Uint words, bool ignore_berr);
        Uint Read(RAWData *DataList,int ntdcs);
};

1541

```

1542 *Source Code A.1: Description of C++ object v1190a.*

1543 The v1190a object, defined in the DAQ software as in Source Code A.1, offers the possibility to
 1544 concatenate all TDCs in the readout setup into a single object containing a list of hardware addresses
 1545 (addresses to access the TDCs' buffer through the VME crate) and each constructor and method acts
 1546 on the list of TDCs.

1547

1548 A.4.2 DataReader

1549 Enabled thanks to v1190a::SetBlockTransferMode(Data16 mode, int ntdcs), the data transfer
 1550 is done via Block Transfer (BLT). Using BLT allows to tranfer a fixed number of events called a
 1551 *block*. This is used together with an Almost Full Level (AFL) of the TDCs' output buffers, defined

1552 through `v1190a::SetIRQ(Data32 level, Data32 count, int ntdcs)`. This AFL gives the maximum amount of 32735 words (16 bits, corresponding to the depth of a TDC output buffer) that can
 1553 written in a buffer before an Interrupt Request (IRQ) is generated and seen by the VME Bridge,
 1554 stopping the data acquisition to transfer the content of each TDC buffers before resuming. For each
 1555 trigger, 6 words or more are written into the TDC buffer:

- 1557 • a **global header** providing information of the event number since the beginning of the data
 acquisition,
- 1559 • a **TDC header**,
- 1560 • the **TDC data** (*if any*), 1 for each hit recorded during the event, providing the channel and the
 time stamp associated to the hit,
- 1562 • a **TDC error** providing error flags,
- 1563 • a **TDC trailer**,
- 1564 • a **global trigger time tag** that provides the absolute trigger time relatively to the last reset,
 and
- 1566 • a **global trailer** providing the total word count in the event.

1567 As previously described in Section ??, CMS RPC FEEs provide us with 100 ns long LVDS output
 1568 signals that are injected into the TDCs' input. Any avalanche signal that gives a signal above the
 1569 FEEs threshold is thus recorded by the TDCs as a hit within the match window. Each hit is assigned
 1570 to a specific TDC channel with a time stamp, with a precision of 100 ps. The reference time, $t_0 = 0$,
 1571 is provided by the beginning of the match window. Thus for each trigger, coming from a scintillator
 1572 coïncidence or the pulse generator, a list of hits is stored into the TDCs' buffers and will then be
 1573 transferred into a ROOT Tree.

1574 When the BLT is used, it is easy to understand that the maximum number of words that have
 1575 been set as ALF will not be a finite number of events or, at least, the number of events that would
 1576 be recorded into the TDC buffers will not be a multiple of the block size. In the last BLT cycle to
 1577 tranfer data, the number of events to transfer will most propably be lower than the block size. In that
 1578 case, the TDC can add fillers at the end of the block but this option requires to send more data to the
 1579 computer and is thus a little slower. Another solution is to finish the transfer after the last event by
 1580 sending a bus error that states that the BLT reached the last event in the pile. This method has been
 1581 chosen in GIF++.

1583 Due to irradiation, an event in GIF++ can count up to 300 words per TDC. A limit of 4096 words
 1584 (12 bits) has been set to generate IRQ which represent from 14 to almost 700 events depending on
 1585 the average of hits collected per event. Then the block size has been set to 100 events with enabled
 1586 bus errors. When an AFL is reached for one of the TDCs, the VME bridge stops the acquisition by
 1587 sending a BUSY signal.

1589

The data is then transferred one TDC at a time into a structure called `RAWData` (Source Code A.2).

```
1591 struct RAWData{
    vector<int> *EventList;
    vector<int> *NHitsList;
    vector<int> *QFlagList;
    vector<vector<int> > *ChannelList;
    vector<vector<float> > *TimeStampList;
}
1592
```

Source Code A.2: Description of data holding C++ structure RAWData.

In order to organize the data transfer and the data storage, an object called `DataReader` was created (Source Code A.3). On one hand, it has `v1718` and `v1190a` objects as private members for communication purposes, such as VME modules settings via the configuration file `*iniFile` or data read-out through `v1190a::Read()` and on the other hand, it contains the struture `RAWData` that allows to organise the data in vectors reproducing the tree structure of a ROOT file.

```
1599 class DataReader
{
    private:
        bool      StopFlag;
        IniFile *iniFile;
        Data32   MaxTriggers;
        v1718   *VME;
        int       nTDCs;
        v1190a  *TDCs;
        RAWData  TDCData;

    public:
        DataReader();
        virtual ~DataReader();
        void     SetIniFile(string inifilename);
        void     SetMaxTriggers();
        Data32   GetMaxTriggers();
        void     SetVME();
        void     SetTDC();
        int      GetQFlag(Uint it);
        void     Init(string inifilename);
        void     FlushBuffer();
        void     Update();
        string   GetFileName();
        void     WriteRunRegistry(string filename);
        void     Run();
};

1600
```

Source Code A.3: Description of C++ object DataReader.

1602 Each event is transferred from `TDCData` and saved into branches of a ROOT `TTree` as 3 integers
1603 that represent the event ID (`EventCount`), the number of hits read from the TDCs (`nHits`), and the
1604 quality flag that provides information for any problem in the data transfer (`qflag`), and 2 lists of
1605 `nHits` elements containing the fired TDC channels (`TDCCH`) and their respective time stamps (`TDCTS`),
1606 as presented in Source Code A.4. The ROOT file file is named using information contained into
1607 the configuration file, presented in section A.5.2. The needed information is extracted using method
1608 `DataReader::GetFileName()` and allow to build the output filename format `ScanXXXXXX_HVX_DAQ.root`

1609 where ScanXXXXXX is a 6 digit number representing the scan number into GIFT++ database and HVX
 1610 the HV step within the scan that can be more than a single digit. An example of ROOT data file is
 1611 provided with Figure A.3.

```
1612
RAWData TDCData;
TFile *outputFile = new TFile(outputFileName.c_str(),"recreate");
TTree *RAWDataTree = new TTree("RAWData","RAWData");

int EventCount = -9;
int nHits = -8;
int qflag = -7;
vector<int> TDCCh;
vector<float> TDCTS;

RAWDataTree->Branch("EventNumber",&EventCount, "EventNumber/I");
RAWDataTree->Branch("number_of_hits",&nHits,"number_of_hits/I");
RAWDataTree->Branch("Quality_flag",&qflag,"Quality_flag/I");
RAWDataTree->Branch("TDC_channel",&TDCCh);
RAWDataTree->Branch("TDC_TimeStamp",&TDCTS);

1613
//...
//Here read the TDC data using v1190a::Read() and place it into
//TDCData for as long as you didn't collect the requested amount
//of data.
//...

for(Uint i=0; i<TDCData.EventList->size(); i++){
    EventCount = TDCData.EventList->at(i);
    nHits = TDCData.NHitsList->at(i);
    qflag = TDCData.QFlagList->at(i);
    TDCCh = TDCData.ChannelList->at(i);
    TDCTS = TDCData.TimeStampList->at(i);
    RAWDataTree->Fill();
}
```

1614 *Source Code A.4: Highlight of the data transfer and organisation within DataReader::Run() after the data has been collected into TDCData.*

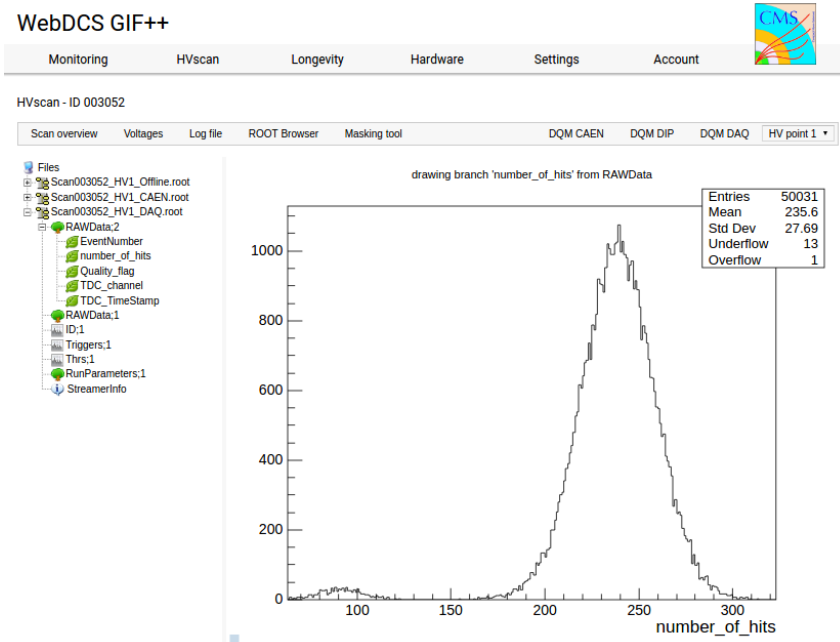


Figure A.3: Structure of the ROOT output file generated by the DAQ. The 5 branches (EventNumber, number_of_hits, Quality_flag, TDC_channel and TDC_TimeStamp) are visible on the left panel of the ROOT browser. On the right panel is visible the histogram corresponding to the variable nHits. In this specific example, there were approximately 50k events recorded to measure the gamma irradiation rate on the detectors. Each event is stored as a single entry in the TTree.

1615 A.4.3 Data quality flag

1616 Among the parameters that are recorded for each event, the quality flag, defined in Source Code A.5,
 1617 is determined on the fly by checking the data recorded by every single TDC. From method `v1190a::Read()`,
 1618 it can be understood that the content of each TDC buffer is readout one TDC at a time. Entries are
 1619 created in the data list for the first TDC and then, when the second buffer is readout, events corre-
 1620 sponding to entries that have already been created to store data for the previous TDC are added to
 1621 the existing list element. On the contrary, when an event entry has not been yet created in the data
 1622 list, a new entry is created.

```
1623
  typedef enum _QualityFlag {
    GOOD      = 1,
    CORRUPTED = 0
} QualityFlag;
```

1625 *Source Code A.5: Definition of the quality flag `enum`.*

1626 It is possible that each TDC buffer contains a different number of events. In cases where the first
 1627 element in the buffer list is an event for corresponds to a new entry, the difference in between the
 1628 entry from the buffer and the last entry in the data list is recorded and checked. If it is greater than 1,
 1629 what should never be the case, the quality flag is set to CORRUPTED for this TDC and an empty entry
 1630 is created in the place of the missing ones. Missing entries are believe to be the result of a bad hold

1631 on the TDC buffers at the moment of the readout. Indeed, the software hold is effective only on 1
 1632 TDC at a time and no solution as been found yet to completely block the writting in the buffers when
 1633 an IRQ is received.

1634 At the end of each BLT cycle, the ID of the last entry stored for each TDC buffer is not recorded.
 1635 When starting the next cycle, if the first entry in the pile corresponds to an event already existing
 1636 in the list, the readout will start from this list element and will not be able to check the difference
 1637 in between this entry's ID and the one of the last entry that was recorded for this TDC buffer in
 1638 the previous cycle. In the case events were missing, the flag stays at its initial value of 0, which is
 1639 similar to CORRUPTED and it is assumed that then this TDC will not contribute to `number_of_hits`,
 1640 `TDC_channel` or `TDC_TimeStamp`.

1641 Finally, since there will be 1 `RAWData` entry per TDC for each event (meaning `nTDCs` entries,
 1642 referring to `DataReader` private attribute), the individual flags of each TDC will be added together.
 1643 The final format is an integer composed `nTDCs` digits where each digit is the flag of a specific TDC.
 1644 This is constructed using powers of 10 like follows:

```
1645 TDC 0: QFlag = 100 × _QualityFlag
1646 TDC 1: QFlag = 101 × _QualityFlag
1647 ...
1648 TDC N: QFlag = 10N × _QualityFlag
```

1649 and the final flag to be with N digits:

1650 `QFlag = n....3210`

1651 each digit being 1 or 0. Below is given an example with a 4 TDCs setup.

1652 If all TDCs were good : `QFlag = 1111`,
 1653 but if TDC 2 was corrupted : `QFlag = 1011`.

1654 When data taking is over and the data contained in the dynamical `RAWData` structure is transferred
 1655 to the ROOT file, all the 0s are changed into 2s by calling the method `DataReader::GetQFlag()`.
 1656 This will help translating the flag without knowing the number of TDCs beforehand. Indeed, a flag
 1657 111 could be due to a 3 TDC setup with 3 good individual TDC flags or to a more than 3 TDC setup
 1658 with TDCs those ID is greater than 2 being CORRUPTED, thus giving a 0.

1659 The quality flag has been introduced quite late, in October 2017 only, to the list of GIFT++ DAQ
 1660 parameters to be recorded into the output ROOT file. Before this addition, the missing data, corrupting
 1661 the quality for the offline analysis, was contributing to artificially fill data with lower multiplicity.
 1662 Looking at `TBranch number_of_hits` provides an information about the data of the full GIFT++
 1663 setup. When a TDC is not able to transfer data for a specific event, the effect is a reduction of the
 1664 total number of hits recorded in the full setup, this is what can be seen from Figure A.4. After offline
 1665 reconstruction detector by detector, the effect of missing events can be seen in the artificially filled
 1666 bin at multiplicity 0 shown in Figure A.5. Nonetheless, for data with high irradiation levels, as it is
 1667 the case for Figure A.5a, discarding the fake multiplicity 0 data can be done easily during the offline
 1668 analysis. At lower radiation, the missing events contribution becomes more problematic as the multi-
 1669 tiplicity distribution overlaps the multiplicity 0 and that in the same time the proportion of missing

events decreases. Attempts to fit the distribution with a Poisson or skew distribution function were not conclusive and this very problem has been at the origin of the quality flag that allows to give a non ambiguous information about each event quality.

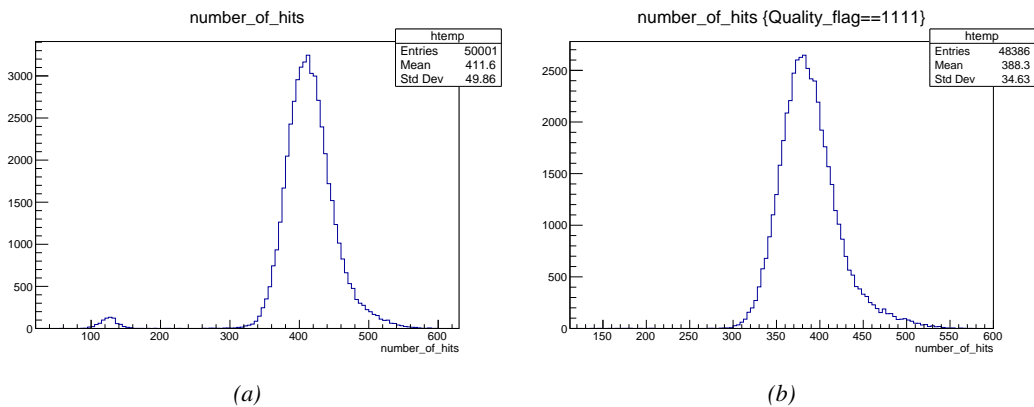


Figure A.4: The effect of the quality flag is explained by presenting the content of `TBranch number_of_hits` of a data file without `Quality_flag` in Figure A.4a and the content of the same `TBranch` for data corresponding to a `Quality_flag` where all TDCs were labelled as `GOOD` in Figure A.4b taken with similar conditions. It can be noted that the number of entries in Figure A.4b is slightly lower than in Figure A.4a due to the excluded events.

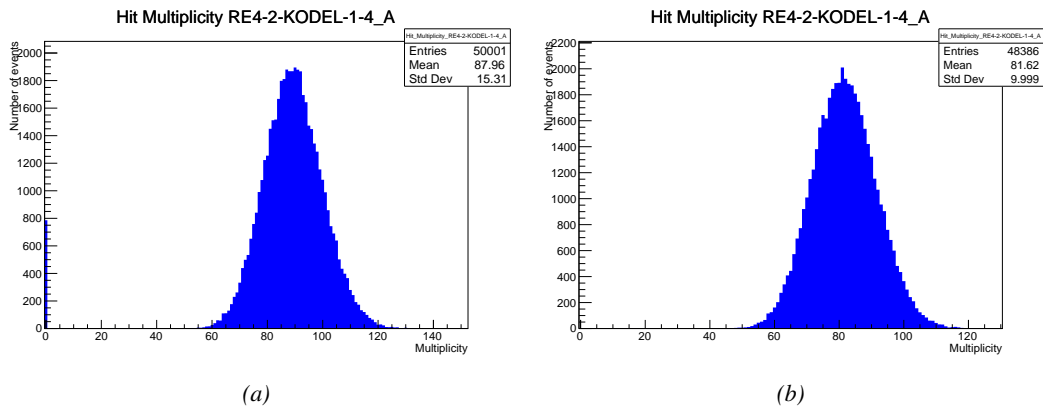


Figure A.5: Using the same data as previously showed in Figure A.4, the effect of the quality flag is explained by presenting the reconstructed hit multiplicity of a data file without `Quality_flag` in Figure A.5a and the reconstructed content of the same RPC partition for data corresponding to a `Quality_flag` where all TDCs were labelled as `GOOD` in Figure A.5b taken with similar conditions. The artificial high content of bin 0 is completely suppressed.

A.5 Communications

1675 To ensure data readout and dialog in between the machine and the TDCs or in between the webDCS
1676 and the DAQ, different communication solutions were used. First of all, it is important to have a

1677 module to allow the communication in between the TDCs and the computer from which the DAQ
 1678 operates. When this communication is effective, shifters using the webDCS to control data taking
 1679 can thus send instructions to the DAQ.

1680

1681 A.5.1 V1718 USB Bridge

1682 In the previous section, the data transfer has been discussed. The importance of the `v1718` object
 1683 (Source Code A.6), used as private member of `DataReader`, was not explicated. VME master
 1684 modules are used for communication purposes as they host the USB port that connects the pow-
 1685 ered crate buffer to the computer where the DAQ is installed. From the source code point of view,
 1686 this object is used to control the communication status, by reading the returned error codes with
 1687 `v1718::CheckStatus()`, or to check for IRQs coming from the TDCs through `v1718::CheckIRQ()`.
 1688 Finally, to ensure that triggers are blocked at the hardware level, a NIM pulse is sent out of one of the
 1689 5 programmable outputs (`v1718::SendBUSY()`) to the VETO of the coincidence module where the
 1690 trigger signals originate from. As long as this signal is ON, no trigger can reach the TDCs anymore.
 1691

```
1692 class v1718{
1693     private:
1694         int             Handle;
1695         Data32          Data;           // Data
1696         CVIRQLevels    Level;         // Interrupt level
1697         CVAddressModifier AM;          // Addressing Mode
1698         CVDataWidth     DataSize;       // Data Format
1699         Data32          BaseAddress;   // Base Address
1700
1701     public:
1702         v1718(IniFile *inifile);
1703         ~v1718();
1704         long            GetHandle(void) const;
1705         int             SetData(Data16 data);
1706         Data16          GetData(void);
1707         int             SetLevel(CVIRQLevels level);
1708         CVIRQLevels    GetLevel(void);
1709         int             SetAM(CVAddressModifier am);
1710         CVAddressModifier GetAM(void);
1711         int             SetDatasize(CVDataWidth datasize);
1712         CVDataWidth     GetDataSize(void);
1713         int             SetBaseAddress(Data16 baseaddress);
1714         Data16          GetBaseAddress(void);
1715         void            CheckStatus(CVErrorCodes status) const;
1716         void            CheckIRQ();
1717         void            SetPulsers();
1718         void            SendBUSY(BusyLevel level);
1719     };
1720 }
```

1693 *Source Code A.6: Description of C++ object v1718.*

1694 A.5.2 Configuration file

1695 The DAQ software takes as input a configuration file written using INI standard [61]. This file is
 1696 partly filled with the information provided by the shifters when starting data acquisition using the
 1697 webDCS, as shown by Figure A.6. This information is written in section [`General`] and will later

1698 be stored in the ROOT file that contains the DAQ data as can be seen from Figure A.3. Indeed,
 1699 another `TTree` called `RunParameters` as well as the 2 histograms `ID`, containing the scan number,
 1700 start and stop time stamps, and `Triggers`, containing the number of triggers requested by the shifter,
 1701 are available in the data files. Moreover, `ScanID` and `HV` are then used to construct the file name
 1702 thanks to the method `DataReader::GetFileName()`.

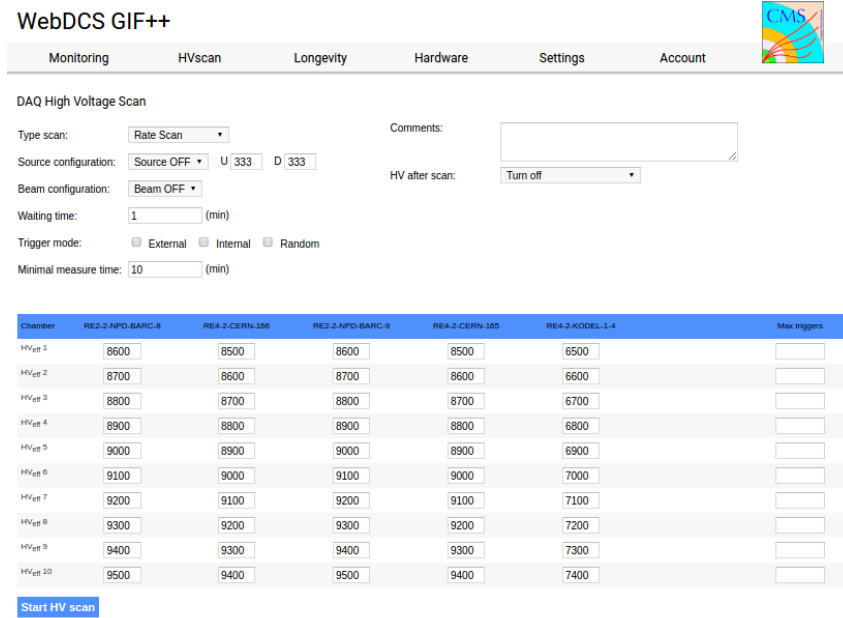


Figure A.6: WebDCS DAQ scan page. On this page, shifters need to choose the type of scan (Rate, Efficiency or Noise Reference scan), the gamma source configuration at the moment of data taking, the beam configuration, and the trigger mode. These information will be stored in the DAQ ROOT output. Are also given the minimal measurement time and waiting time after ramping up of the detectors is over before starting the data acquisition. Then, the list of HV points to scan and the number of triggers for each run of the scan are given in the table underneath.

1703 The rest of the information is written beforehand in the configuration file template, as explicated
 1704 in Source Code A.7, and contains the hardware addresses to the different VME modules in the
 1705 setup as well as settings for the TDCs. As the TDC settings available in the configuration file are not
 1706 supposed to be modified, an improvement would be to remove them from the configuration file and
 1707 to hardcode them inside of the DAQ code itself or to place them into a different INI file that would
 1708 host only the TDC settings to lower the probability for a bad manipulation of the configuration file
 1709 that can be modified from one of webDCS' menus.

```
1710
[General]
TdcS=4
ScanID=$scanid
HV=$HV
RunType=$runtype
MaxTriggers=$maxtriggers
Beam=$beam
[VMEInterface]
Type=V1718
BaseAddress=0xFF0000
Name=VmeInterface
[TDC0]
Type=V1190A
BaseAddress=0x00000000
Name=Tdc0
StatusA00-15=1
StatusA16-31=1
StatusB00-15=1
StatusB16-31=1
StatusC00-15=1
StatusC16-31=1
StatusD00-15=1
StatusD16-31=1
[TDC1]
Type=V1190A
BaseAddress=0x11110000
Name=Tdc1
StatusA00-15=1
StatusA16-31=1
StatusB00-15=1
StatusB16-31=1
StatusC00-15=1
StatusC16-31=1
StatusD00-15=1
StatusD16-31=1
1711
[TDC2]
Type=V1190A
BaseAddress=0x22220000
Name=Tdc2
StatusA00-15=1
StatusA16-31=1
StatusB00-15=1
StatusB16-31=1
StatusC00-15=1
StatusC16-31=1
StatusD00-15=1
StatusD16-31=1
[TDC3]
Type=V1190A
BaseAddress=0x44440000
Name=Tdc3
StatusA00-15=1
StatusA16-31=1
StatusB00-15=1
StatusB16-31=1
StatusC00-15=1
StatusC16-31=1
StatusD00-15=1
StatusD16-31=1
[TDCSettings]
TriggerExtraSearchMargin=0
TriggerRejectMargin=0
TriggerTimeSubtraction=0b1
TdcDetectionMode=0b01
TdcResolution=0b10
TdcDeadTime=0b00
TdcHeadTrailer=0b1
TdcEventSize=0b1001
TdcTestMode=0b0
BLTMode=1
```

Source Code A.7: INI configuration file template for 4 TDCs. In section [General], the number of TDCs is explicitated and information about the ongoing run is given. Then, there are sections for each and every VME modules. There buffer addresses are given and for the TDCs, the list of channels to enable is given. Finally, in section [TDCSettings], a part of the TDC settings are given.

1713 In order to retrieve the information of the configuration file, the object `IniFile` has been developed
 1714 to provide an INI parser, presented in Source Code A.8. It contains private methods returning a
 1715 boolean to check the type of line written in the file, whether a comment, a group header or a key line
 1716 (`IniFile::CheckIfComment()`, `IniFile::CheckIfGroup()` and `IniFile::CheckIfToken()`). The
 1717 key may sometimes be referred to as *token* in the source code. Moreover, the private element
 1718 `FileData` is a map of `const string` to `string` that allows to store the data contained inside the
 1719 configuration file via the public method `IniFile::GetFileData()` following the formatting (see
 1720 method `IniFile::Read()`):

```
1721
 1722     string group, token, value;
 1723     // Get the field values for the 3 strings.
 1724     // Then concatenate group and token together as a single string
 1725     // with a dot separation.
 1726     token = group + "." + token;
 1727     FileData[token] = value;
```

1723 More methods have been written to translate the different keys into the right variable format
 1724 when used by the DAQ. For example, to get a `float` value out of the configuration file data, knowing
 1725 the group and the key needed, the method `IniFile::floatType()` can be used. It takes 3 arguments
 1726 being the group name and key name (both `string`), and a default `float` value used as exception in
 1727 the case the expected combination of group and key cannot be found in the configuration file. This
 1728 default value is then used and the DAQ continues on working after sending an alert in the log file for
 1729 further debugging.

```

1730 typedef map< const string, string > IniFileData;

class IniFile{
    private:
        bool          CheckIfComment (string line);
        bool          CheckIfGroup(string line, string& group);
        bool          CheckIfToken(string line, string& key, string& value);
        string         FileName;
        IniFileData   FileData;
        int           Error;

    public:
        IniFile();
        IniFile(string filename);
        virtual      ~IniFile();

        // Basic file operations
        void          SetFileName(string filename);
        int           Read();
        int           Write();
        IniFileData   GetFileData();

        // Data readout methods
        Data32         addressType (string groupname, string keyname, Data32
→     defaultvalue);
        long          intType     (string groupname, string keyname, long
→     defaultvalue);
        long long    longType    (string groupname, string keyname, long long
→     defaultvalue );
        string         stringType  (string groupname, string keyname, string
→     defaultvalue );
        float         floatType   (string groupname, string keyname, float
→     defaultvalue );

        // Error methods
        string         GetErrorMsg();
};

1731

```

1732 *Source Code A.8: Description of C++ object `IniFile` used as a parser for INI file format.*

1733 A.5.3 WebDCS/DAQ intercommunication

1734 When shifters send instructions to the DAQ via the configuration file, it is the webDCS itself that
 1735 gives the start command to the DAQ and then the 2 softwares use inter-process communication
 1736 through file to synchronise themselves. This communication file is represented by the variable **const**
 1737 **string** __runstatuspath.

1738 On one side, the webDCS sends commands or status that are readout by the DAQ:

- 1739 ● INIT, status sent when launching a scan and read via function `CtrlRunStatus(...)`,
- 1740 ● START, command to start data taking and read via function `CheckSTART()`,
- 1741 ● STOP, command to stop data taking at the end of the scan and read via function `CheckSTOP()`,
 1742 and
- 1743 ● KILL, command to kill data taking sent by user and read via function `CheckKILL()`

and on the other, the DAQ sends status that are controled by the webDCS:

- 1745 ● `DAQ_RDY`, sent with `SendDAQReady()` to signify that the DAQ is ready to receive commands
1746 from the webDCS,
- 1747 ● `RUNNING`, sent with `SendDAQRunning()` to signify that the DAQ is taking data,
- 1748 ● `DAQ_ERR`, sent with `SendDAQError()` to signify that the DAQ didn't receive the expected com-
1749 mand from the webDCS or that the launch command didn't have the right number of argu-
1750 ments,
- 1751 ● `RD_ERR`, sent when the DAQ wasn't able to read the communication file, and
- 1752 ● `WR_ERR`, sent when the DAQ wasn't able to write into the communication file.

1753 **A.5.4 Example of inter-process communication cycle**

1754 Under normal conditions, the webDCS and the DAQ processes exchange commands and status via
1755 the file hosted at the address `__runstatuspath`, as explained in subsection A.5.3. An example of
1756 cycle is given in Table A.1. In this example, the steps 3 to 5 are repeated as long as the webDCS tells
1757 the DAQ to take data. A data taking cycle is the equivalent as what is called a *Scan* in GIFT++ jargon,
1758 referring to a set a runs with several HV steps. Each repetition of steps 3 to 5 is then equivalent to a
1759 single *Run*.

1760 At any moment during the data taking, for any reason, the shifter can decide that the data taking
1761 needs to be stopped before it reached the end of the scheduled cycle. Thus at any moment on the
1762 cycle, the content of the inter-process communication file will be changed to `KILL` and the DAQ will
1763 shut down right away. The DAQ checks for `KILL` signals every 5s after the TDCs configuration is
1764 over. So far, the function `CheckKILL()` has been used only inside of the data taking loop of method
1765 `DataReader::Run()` and thus, if the shifter decides to KILL the data taking during the TDC con-
1766 figuration phase or the HV ramping in between 2 HV steps, the DAQ will not be stopped smoothly
1767 and a *force kill* command will be sent to stop the DAQ process that is still awake on the computer.
1768 Improvements can be brought on this part of the software to make sure that the DAQ can safely
1769 shutdown at any moment.

1772 **A.6 Software export**

1773 In section A.2 was discussed the fact that the DAQ as written in its last version is not a standalone
1774 software. It is possible to make it a standalone program that could be adapted to any VME setup
1775 using V1190A and V1718 modules by creating a GUI for the software or by printing the log mes-
1776 sages that are normally printed in the webDCS through the log file, directly into the terminal. This
1777 method was used by the DAQ up to version 3.0 moment where the webDCS was completed. Also, it
1778 is possible to check branches of DAQ v2.X to have example of communication through a terminal.

1779 DAQ v2.X is nonetheless limited in it's possibilities and requires a lot of offline manual interven-
1780 tions from the users. Indeed, there is no communication of the software with the detectors' power
1781 supply system that would allow for a user a predefine a list of voltages to operate the detectors at

step	actions of webDCS	status of DAQ	<code>__runstatuspath</code>
1	launch DAQ ramp voltages ramping over wait for currents stabilization	readout of IniFile configuration of TDCs	INIT
2		configuration done send DAQ ready wait for START signal	DAQ_RDY
3	waiting time over send START		START
4	wait for run to end monitor DAQ run status	data taking ongoing check for KILL signal	RUNNING
5		run over send DAQ_RDY wait for next DCS signal	DAQ_RDY
6	ramp voltages ramping over wait for currents stabilization		DAQ_RDY
3	waiting time over send START		START
4	wait for run to end monitor DAQ run status	update IniFile information data taking ongoing check for KILL signal	RUNNING
5		run over send DAQ_RDY wait for next DCS signal	DAQ_RDY
7	send command STOP	DAQ shuts down	STOP

Table A.1: Inter-process communication cycles in between the webDCS and the DAQ through file string signals.

1783 and loop over to take data without any further manual intervention. In v2.X, the data is taken for a
1784 single detector setting and at the end of each run, the softwares asks the user if he intends on taking
1785 more runs. If so, the software invites the user to set the operating voltages accordingly to what is
1786 necessary and to manual update the configuration file in consequence. This working mode can be a
1787 very first approach before an evolution and has been successfully used by colleagues from different
1788 collaborations.

1789

1790 For a more robust operation, it is recommended to develop a GUI or a web application to inter-
1791 face the DAQ. Moreover, to limit the amount of manual interventions, and thus the probability to
1792 make mistakes, it is also recommended to add an extra feature into the DAQ by installing the HV
1793 Wrapper library provided by CAEN of which an example of use in a similar DAQ software devel-
1794 opped by a master student of UGent, and called TinyDAQ, is provided on UGent's github. Then, this
1795 HV Wrapper will help you communicating with and give instructions to a CAEN HV powered crate
1796 and can be added into the DAQ at the same level where the communication with the user was made
1797 in DAQ v2.X. In case you are using another kind of power system for your detectors, it is stringly
1798 adviced to use HV modules or crates that can be remotely controled via a using C++ libraries.

1799

B

1800

1801

Details on the offline analysis package

1802 The data collected in GIF++ thanks to the DAQ described in Appendix A is difficult to interpret by
1803 a human user that doesn't have a clear idea of the raw data architecture of the ROOT data files. In
1804 order to render the data human readable, a C++ offline analysis tool was designed to provide users
1805 with detector by detector histograms that give a clear overview of the parameters monitored during
1806 the data acquisition [62]. In this appendix, details about this software in the context of GIF++, as of
1807 how the software was written and how it functions will be given.

1808 B.1 GIF++ Offline Analysis file tree

1809 GIF++ Offline Analysis source code is fully available on github at https://github.com/aafagot/GIF_OfflineAnalysis. The software requires ROOT as non-optionnal dependency
1810 as it takes ROOT files in input and write an output ROOT file containing histograms. To compile the
1811 GIF++ Offline Analysis project is compiled with cmake. To compile, first a build/ directory must
1812 be created to compile from there:

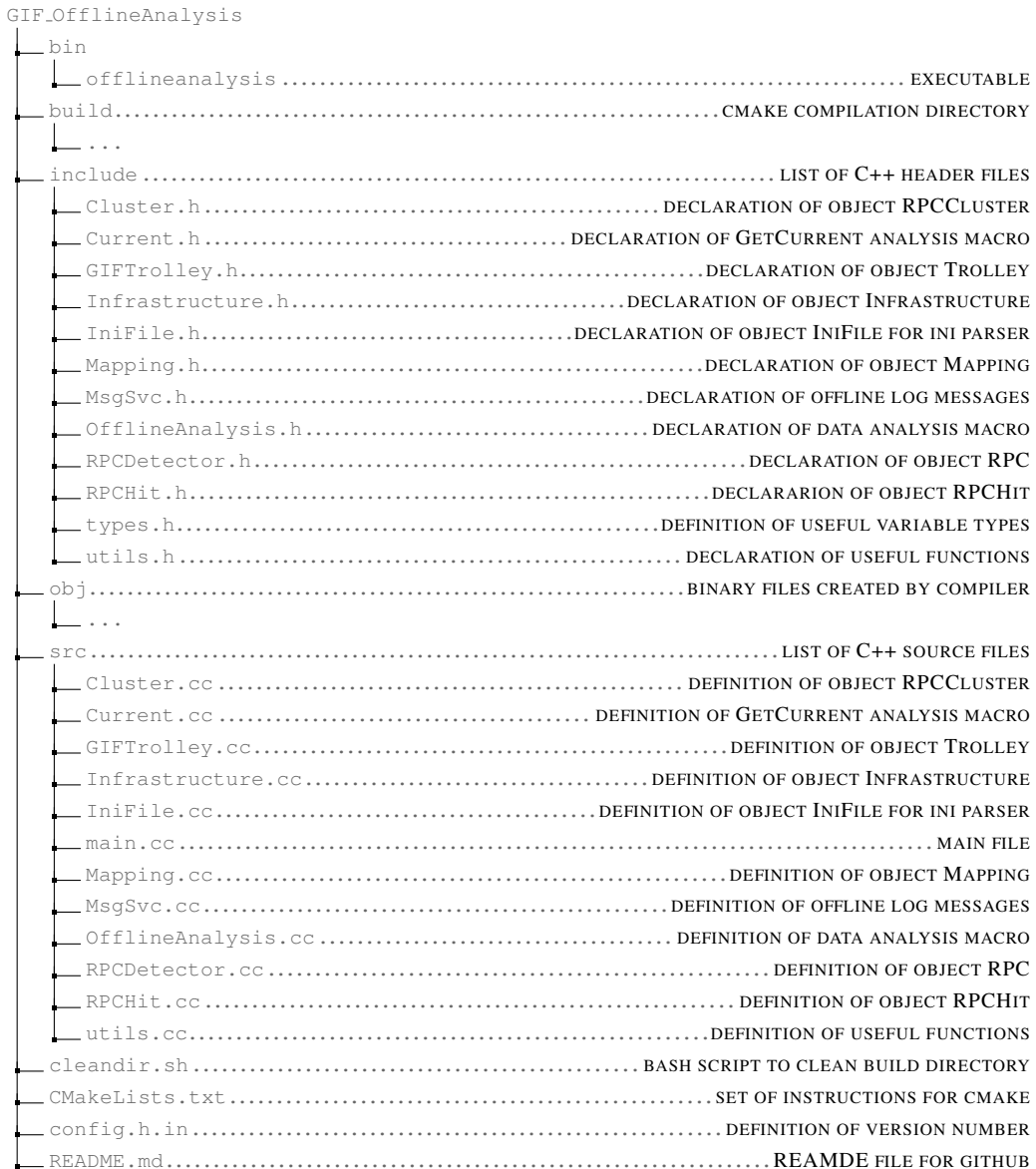
```
1814 mkdir build
1815 cd build
1816 cmake ..
1817 make
1818 make install
```

1816 To clean the directory and create a new build directory, the bash script cleandir.sh can be used:

```
1817
1818 ./cleandir.sh
```

1819 The source code tree is provided below along with comments to give an overview of the files' con-
1820 tent. The different objects created for this project (`Infrastructure`, `Trolley`, `RPC`, `Mapping`, `RPCHit`,
1821 `RPCCluster` and `Inifile`) will be described in details in the following sections.

1822



1823

B.2 Usage of the Offline Analysis

1824
1825

In order to use the Offline Analysis tool, it is necessary to know the Scan number and the HV Step of the run that needs to be analysed. This information needs to be written in the following format:

1826
1827

```
Scan00XXXX_HVY
```

1828
1829

where XXXX is the scan ID and Y is the high voltage step (in case of a high voltage scan, data will be taken for several HV steps). This format corresponds to the base name of data files in the database

1830 of the Gif++ webDCS. Usually, the offline analysis tool is automatically called by the webDCS at
 1831 the end of data taking or by a user from the webDCS panel if an update of the tool was brought.
 1832 Nonetheless, an expert can locally launch the analysis for tests on the Gif++ computer, or a user can
 1833 get the code on its local machine from github and download data from the webDCS for its own anal-
 1834 ysis. To launch the code, the following command can be used from the `GIF_OfflineAnalysis` folder:

1835
 1836 `bin/offlineanalysis /path/to/Scan00XXXX_HVY`

1837 where, `/path/to/Scan00XXXX_HVY` refers to the local data files. Then, the offline tool will by itself
 1838 take care of finding all available ROOT data files present in the folder, as listed below:

- 1839
 - 1840 ● `Scan00XXXX_HVY_DAQ.root` containing the TDC data as described in Appendix ?? (events, hit
 and timestamp lists), and
 - 1841 ● `Scan00XXXX_HVY_CAEN.root` containing the CAEN mainframe data recorded by the monitor-
 ing tool webDCS during data taking (HVs and currents of every HV channels). This file is
 created independently of the DAQ.

1844 B.2.1 Output of the offline tool

1845 B.2.1.1 ROOT file

1846 The analysis gives in output ROOT datafiles that are saved into the data folder and called using the
 1847 naming convention `Scan00XXXX_HVY_Offline.root`. Inside those, a list of `TH1` histograms can be
 1848 found. Its size will vary as a function of the number of detectors in the setup as each set of histograms
 1849 is produced detector by detector. For each partition of each chamber, can be found:

- 1850
 - 1851 ● `Time_Profile_Tt_Sc_p` shows the time profile of all recorded events (number of events per
 time bin),
 - 1852 ● `Hit_Profile_Tt_Sc_p` shows the hit profile of all recorded events (number of events per chan-
 nel),
 - 1854 ● `Hit_Multiplicity_Tt_Sc_p` shows the hit multiplicity (number of hits per event) of all recorded
 events (number of occurrences per multiplicity bin),
 - 1856 ● `Strip_Mean_Noise_Tt_Sc_p` shows noise/gamma rate per unit area for each strip in a se-
 lected time range. After filters are applied on `Time_Profile_Tt_Sc_p`, the filtered version
 of `Hit_Profile_Tt_Sc_p` is normalised to the total integrated time and active detection area
 of a single channel,
 - 1860 ● `Strip_Activity_Tt_Sc_p` shows noise/gamma activity for each strip (normalised version of
 previous histogram - strip activity = strip rate / average partition rate),
 - 1862 ● `Strip_Homogeneity_Tt_Sc_p` shows the *homogeneity* of a given partition ($\text{homogeneity} = \exp(-\text{strip rates standard deviation(strip rates in partition/average partition rate)})$),
 - 1864 ● `mask_Strip_Mean_Noise_Tt_Sc_p` shows noise/gamma rate per unit area for each masked
 strip in a selected time range. Offline, the user can control the noise/gamma rate and decide to
 mask the strips that are judged to be noisy or dead. This is done via the *Masking Tool* provided
 by the webDCS,

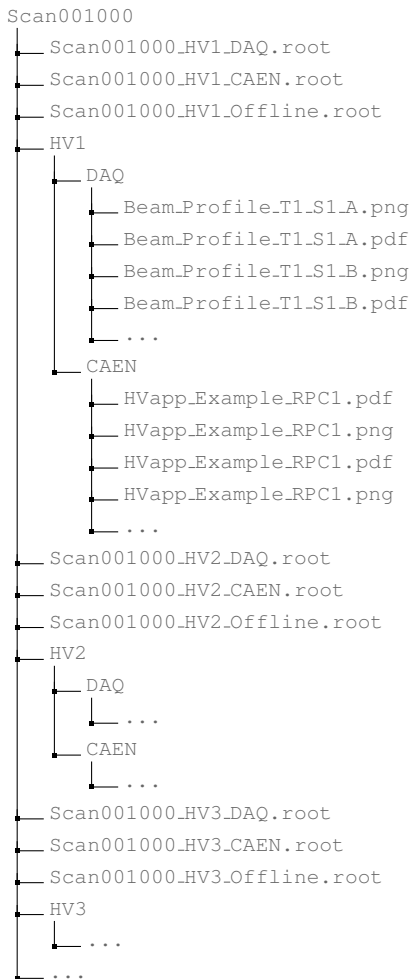
- 1868 ● `mask_Strip_Activity_Tt_Sc_p` shows noise/gamma activity per unit area for each masked
1869 strip with respect to the average rate of active strips,
- 1870 ● `NoiseCSize_H_Tt_Sc_p` shows noise/gamma cluster size, a cluster being constructed out of
1871 adjacent strips giving a signal at the *same time* (hits within a time window of 25 ns),
- 1872 ● `NoiseCMult_H_Tt_Sc_p` shows noise/gamma cluster multiplicity (number of reconstructed
1873 clusters per event),
- 1874 ● `Chip_Mean_Noise_Tt_Sc_p` shows the same information than `Strip_Mean_Noise_Tt_Scp` us-
1875 ing a different binning (1 chip corresponds to 8 strips),
- 1876 ● `Chip_Activity_Tt_Sc_p` shows the same information than `Strip_Activity_Tt_Scp` using
1877 chip binning,
- 1878 ● `Chip_Homogeneity_Tt_Sc_p` shows the homogeneity of a given partition using chip binning,
- 1879 ● `Beam_Profile_Tt_Sc_p` shows the estimated beam profile when taking efficiency scan. This
1880 is obtained by filtering `Time_Profile_Tt_Sc_p` to only consider the muon peak where the
1881 noise/gamma background has been subtracted. The resulting hit profile corresponds to the
1882 beam profile on the detector channels,
- 1883 ● `L0_Efficiency_Tt_Sc_p` shows the level 0 efficiency that was estimated **without** muon track-
1884 ing,
- 1885 ● `MuonCSize_H_Tt_Sc_p` shows the level 0 muon cluster size that was estimated **without** muon
1886 tracking, and
- 1887 ● `MuonCMult_H_Tt_Sc_p` shows the level 0 muon cluster multiplicity that was estimated **without**
1888 muon tracking.

1889 In the histogram labels, t stands for the trolley number (1 or 3), c for the chamber slot label in
1890 trolley t and p for the partition label (A, B, C or D depending on the chamber layout) as explained
1891 in Chapter ??.

1892 In the context of GIF++, an extra script called by the webDCS is called to extract the histograms
1893 from the ROOT files. The histograms are then stored in PNG and PDF formats into the correspond-
1894 ing folder (a single folder per HV step, so per ROOT file). the goal is to then display the histograms
1895 on the Data Quality Monitoring (DQM) page of the webDCS in order for the users to control the
1896 quality of the data taking at the end of data taking. An example of histogram organisation is given
1897 below:

1898

1899



1900 ***Here can put some screens from the webDCS to show the DQM and the plots available to users.***
 1901

1902 **B.2.1.2 CSV files**

1903 Moreover, up to 3 CSV files can be created depending on which ones of the 3 input files were in the
 1904 data folder:

- 1905 • `Offline-Corrupted.csv` , is used to keep track of the amount of data that was corrupted and
 1906 removed from old data format files that don't contain any data quality flag.
- 1907 • `Offline-Current.csv` , contains the summary of the currents and voltages applied on each
 1908 RPC HV channel.
- 1909 • `Offline-L0-EffC1.csv` , is used to write the efficiencies, cluster size and cluster multiplicity
 1910 of efficiency runs. Note that `L0` refers here to *Level 0* and means that the results of efficiency and
 1911 clusterization are a first approximation calculated without performing any muon tracking in

1912 between the different detectors. This offline tool provides the user with a preliminar calculation
 1913 of the efficiency and of the muon event parameters. Another analysis software especially
 1914 dedicated to muon tracking is called on selected data to retrieve the results of efficiency and
 1915 muon clusterization using a tracking algorithm to discriminate noise or gamma from muons
 1916 as muons are the only particles that pass through the full setup, leaving hits than can be used
 1917 to reconstruct their tracks.

- 1918 ● `Offline-Rate.csv`, is used to write the noise or gamma rates measured in the detector readout
 1919 partitions.

1920 Note that these 4 CSV files are created along with their *headers* (`Offline-[...]-Header.csv`
 1921 containing the names of each data columns) and are automatically merged together when the offline
 1922 analysis tool is called from the webDCS, contrary to the case where the tool is runned locally from
 1923 the terminal as the merging bash script is then not called. Thus, the resulting files, used to make
 1924 official plots, are:

- 1925 ● `Corrupted.csv`,
 1926 ● `Current.csv`,
 1927 ● `L0-EffCl.csv`.
 1928 ● `Rate.csv`.

1929 **B.3 Analysis inputs and information handling**

1930 The usage of the Offline Analysis tool as well as its output have been presented in the previous section.
 1931 It is now important to dig further and start looking at the source code and the inputs necessary
 1932 for the tool to work. Indeed, other than the raw ROOT data files that are analysed, more information
 1933 needs to be imported inside of the program to perform the analysis such as the description of the
 1934 setup inside of GIFT++ at the time of data taking (number of trolleys, of RPCs, dimensions of the
 1935 detectors, etc...) or the mapping that links the TDC channels to the coresponding RPC channels in
 1936 order to translate the TDC information into human readable data. 2 files are used to transmit all this
 1937 information:
 1938

- 1939 ● `Dimensions.ini`, that provides the necessary setup and RPC information, and
 1940 ● `ChannelsMapping.csv`, that gives the link between the TDC and RPC channels as well as the
 1941 *mask* for each channel (masked or not?).

1942 **B.3.1 Dimensions file and InFile parser**

1943 This input file, present in every data folder, allows the analysis tool to know of the number of active
 1944 trolleys, the number of active RPCs in those trolleys, and the details about each RPCs such as
 1945 the number of RPC gaps, the number of pseudo-rapidity partitions (for CMS-like prototypes), the
 1946 number of strips per partion or the dimensions. To do so, there are 3 types of groups in the INI file
 1947 architecture. A first general group, appearing only once at the head of the document, gives information
 1948 about the number of active trolleys as well as their IDs, as presented in Source Code B.1. For

1949 each active trolley, a group similar to Source Code B.2 can be found containing information about
 1950 the number of active detectors in the trolley and their IDs. Each trolley group as a `Tt` name format,
 1951 where `t` is the trolley ID. Finally, for each detector stored in slots of an active trolley, there is a group
 1952 providing information about their names and dimensions, as shown in Source Code B.3. Each slot
 1953 group as a `TtSs` name format, where `s` is the slot ID of trolley `t` where the active RPC is hosted.

```
1954 [General]
1955 nTrolleys=2
  TrolleysID=13
```

1956 *Source Code B.1: Example of `[General]` group as might be found in `Dimensions.ini`. In Gif++, only 2 trolleys are available to hold RPCs and place them inside of the bunker for irradiation. The IDs of the trolleys are written in a single string as "13" and then read character by character by the program.*

```
1957 [T1]
  nSlots=4
  SlotsID=1234
```

1958 *Source Code B.2: Example of trolley group as might be found in `Dimensions.ini`. In this example, the file tells that there are 4 detectors placed in the holding slots of the trolley `T1` and that their IDs, written as a single string variable, are 1, 2, 3 and 4.*

```
1959 [T1S1]
  Name=RE2-2-NPD-BARC-8
  Partitions=3
  Gaps=3
  Gap1=BOT
  Gap2=TN
  Gap3=TW
  AreaGap1=11694.25
  AreaGap2=6432
  AreaGap3=4582.82
  Strips=32
  ActiveArea-A=157.8
  ActiveArea-B=121.69
  ActiveArea-C=93.03
```

1960 *Source Code B.3: Example of slot group as might be found in `Dimensions.ini`. In this example, the file provides information about a detector named `RE2-2-NPD-BARC-8`, having 3 pseudo-rapidity readout partitions and stored in slot `S1` of trolley `T1`. This is a CMS RE2-2 type of detector. This information will then be used for example to compute the rate per unit area calculation.*

1961 This information is readout and stored in a C++ object called `IniFile`, that parses the information
 1962 in the INI input file and stores it into a local buffer for later use. This INI parser is the exact same
 1963 one that was previously developed for the Gif++ DAQ and described in Appendix A.5.2.

1964 B.3.2 TDC to RPC link file and Mapping

1965 The same way the INI dimension file information is stored using `map`, the channel mapping and mask
 1966 information is stored and accessed through `map`. First of all, the mapping CSV file is organised into
 1967 3 columns separated by tabulations (and not by commas, as expected for CSV files as it is easier using
 1968 streams to read tab or space separated data using C++):

1969

1970 RPC_channel TDC_channel mask

1971 using as formatting for each field:

1972 TSCCC TCCC M

1974 TSCCC is a 5-digit integer where T is the trolley ID, s the slot ID in which the RPC is held insite
 1975 the trolley T and CCC is the RPC channel number, or *strip* number, that can take values up to
 1976 3-digits depending on the detector,

1977 TCCC is a 4 digit integer where T is the TDC ID, CCC is the TDC channel number that can take values
 1978 in between 0 and 127, and

1979 M is a 1-digit integer indicating if the channel should be considered ($M = 1$) or discarded ($M = 0$)
 1980 during analysis.

1981 This mapping and masking information is readout and stored thanks to the object `Mapping`, pre-
 1982 sented in Source Code B.4. Similarly to `IniFile` objects, this class has private methods. The first
 1983 one, `Mapping::CheckIfNewLine()` is used to find the newline character '`\n`' or return character
 1984 '`\r`' (depending on which kind of operating system interacted with the file). This is used for the
 1985 simple reason that the masking information has been introduced only during the year 2017 but the
 1986 channel mapping files exist since 2015 and the very beginning of data taking at GIF++. This means
 1987 that in the older data folders, before the upgrade, the channel mapping file only had 2 columns, the
 1988 RPC channel and the TDC channel. For compatibility reasons, this method helps controling the
 1989 character following the readout of the 2 first fields of a line. In case any end of line character is
 1990 found, no mask information is present in the file and the default $M = 1$ is used. On the contrary, if
 1991 the next character was a tabulation or a space, the mask information is present.

1992 Once the 3 fields have been readout, the second private method `Mapping::CheckIfTDCCh()` is
 1993 used to control that the TDC channel is an existing TDC channel. Finally, the information is stored
 1994 into 3 different maps (`Link`, `ReverseLink` and `Mask`) thanks to the public method `Mapping::Read()`.
 1995 `Link` allows to get the RPC channel by knowing the TDC channel while `ReverseLink` does the op-
 1996 posite by returning the TDC channel by knowing the RPC channel. Finally, `Mask` returns the mask
 1997 associated to a given RPC channel.

```

1998 typedef map<Uint,Uint> MappingData;

1999 class Mapping {
2000     private:
2001         bool          CheckIfNewLine(char next);
2002         bool          CheckIfTDCCh(Uint channel);
2003         string        FileName;
2004         MappingData  Link;
2005         MappingData  ReverseLink;
2006         MappingData  Mask;
2007         int           Error;
2008
2009     public:
2010         Mapping();
2011         Mapping(string baseName);
2012         ~Mapping();
2013
2014         void SetFileName(const string filename);
2015         int  Read();
2016         Uint GetLink(Uint tdcchannel);
2017         Uint GetReverse(Uint rpcchannel);
2018         Uint GetMask(Uint rpcchannel);
2019     };

```

2000 *Source Code B.4: Description of C++ object Mapping used as a parser for the channel mapping and mask file.*

2001 B.4 Description of GIF++ setup within the Offline Analysis tool

2002 In the previous section, the tool input files have been discussed. The dimension file information is
 2003 stored in a map hosted by the `IniFile` object. But this information is then used to create a series of
 2004 new objects that helps defining the GIF++ infrastructure directly into the Offline Analysis. Indeed,
 2005 from the `RPC`, to the more general `Infrastructure`, every element of the GIF++ infrastrucutre is
 2006 recreated for each data analysis based on the information provided in input. All this information
 2007 about the infrastructure will be used to assign each hit signal to a specific strip channel of a specific
 2008 detector, and having a specific active area. This way, rate per unit area calculation is possible.
 2009

2010 B.4.1 RPC objects

2011 `RPC` objects have been developped to represent physical active detectors in GIF++ at the moment
 2012 of data taking. Thus, there are as many `RPC` objects created during the analysis than there were
 2013 active `RPCs` tested during a run. Each `RPC` hosts the information present in the corresponding INI
 2014 slot group, as shown in B.3, and organises it using a similar architecture. This can be seen from
 2015 Source B.5.

2016 To make the object more compact, the lists of gap labels, of gap active areas and strip active
 2017 areas are stored into `vector` dynamical containers. `RPC` objects are always contructed thanks to the
 2018 dimension file information stored into the `IniFILE` and their ID, using the format `TtSs`. Using the
 2019 `RPC` ID, the constructor calls the methods of `IniFILE` to initialise the `RPC`. The other constructors
 2020 are not used but exist in case of need. Finally, some getters have been written to access the different
 2021 private parameters storing the detector information.

2022

```

class RPC{
    private:
        string      name;           //RPC name as in webDCS database
        Uint        nGaps;          //Number of gaps in the RPC
        Uint        nPartitions;    //Number of partitions in the RPC
        Uint        nStrips;         //Number of strips per partition
        vector<string> gaps;       //List of gap labels (BOT, TOP, etc...)
        vector<float>  gapGeo;        //List of gap active areas
        vector<float>  stripGeo;      //List of strip active areas

    public:
        RPC();
        RPC(string ID, IniFile* geofile);
        RPC(const RPC& other);
        ~RPC();
        RPC& operator=(const RPC& other);

        string GetName();
        Uint GetNGaps();
        Uint GetNPartitions();
        Uint GetNStrips();
        string GetGap(Uint g);
        float GetGapGeo(Uint g);
        float GetStripGeo(Uint p);
};

```

2023

2024 *Source Code B.5: Description of C++ objects RPC that describe each active detectors used during data taking.*

2025

B.4.2 Trolley objects

2026 Trolley objects have been developped to represent physical active trolleys in GIFT++ at the moment
 2027 of data taking. Thus, there are as many trolley objects created during the analysis than there were
 2028 active trolleys hosting tested RPCs during a run. Each Trolley hosts the information present in the
 2029 corresponding INI trolley group, as shown in B.2, and organises it using a similar architecture. In
 2030 addition to the information hosted in the INI file, these object have a dynamical container of RPC
 2031 objects, representing the active detectors the active trolley was hosting at the time of data taking.
 2032 This can been seen from Source Code B.6.

2033 Trolley objects are always contructed thanks to the dimension file information stored into the
 2034 IniFILE and their ID, using the format Tt. Using the Trolley ID, the constructor calls the methods
 2035 of IniFILE to initialise the Trolley. Retrieving the information of the RPC IDs via SlotsID, a new
 2036 RPC is constructed and added to the container RPCs for each character in the ID string. The other
 2037 constructors are not used but exist in case of need. Finally, some getters have been written to access
 2038 the different private parameters storing the trolley and detectors information.

```

2039 class Trolley{
2040     private:
2041         Uint          nSlots; //Number of active RPCs in the considered trolley
2042         string        SlotsID; //Active RPC IDs written into a string
2043         vector<RPC*> RPCs;   //List of active RPCs
2044
2045     public:
2046         //Constructors, destructor and operator =
2047         Trolley();
2048         Trolley(string ID, IniFile* geofile);
2049         Trolley(const Trolley& other);
2050         ~Trolley();
2051         Trolley& operator=(const Trolley& other);
2052
2053         //Get GIFTrolley members
2054         Uint    GetNSlots();
2055         string  GetSlotsID();
2056         Uint    GetSlotID(Uint s);
2057
2058         //Manage RPC list
2059         RPC*   GetRPC(Uint r);
2060         void   DeleteRPC(Uint r);
2061
2062         //Methods to get members of RPC objects stored in RPCs
2063         string  GetName(Uint r);
2064         Uint    GetNGaps(Uint r);
2065         Uint    GetNPartitions(Uint r);
2066         Uint    GetNStrips(Uint r);
2067         string  GetGap(Uint r, Uint g);
2068         float   GetGapGeo(Uint r, Uint g);
2069         float   GetStripGeo(Uint r, Uint p);
2070     };

```

Source Code B.6: Description of C++ objects `Trolley` that describe each active trolley used during data taking.

2042 B.4.3 Infrastructure object

2043 The `Infrastructure` object has been developped to represent the GIFT++ bunker area dedicated to
 2044 CMS RPC experiments. With this very specific object, all the information about the CMS RPC
 2045 setup within GIFT++ at the moment of data taking is stored. It hosts the information present in the
 2046 corresponding INI general group, as shown in B.1, and organises it using a similar architecture. In
 2047 addition to the information hosted in the INI file, this object have a dynamical container of `Trolley`
 2048 objects, representing the active tolleys in GIFT++ area. This can be seen from Source Code B.7.

2049 The `Infrastructure` object is always contructed thanks to the dimension file information stored
 2050 into the `IniFILE`. Retrieving the information of the trolley IDs via `TrolleysID`, a new `Trolley` is
 2051 constructed and added to the container `Trolleys` for each character in the ID `string`. By extension,
 2052 it is easy to understand that the process described in Section B.4.2 for the construction of RPCs
 2053 takes place when a trolley is constructed. The other constructors are not used but exist in case of
 2054 need. Finally, some getters have been written to access the different private parameters storing the
 2055 infrastructure, tolleys and detectors information.

```

2056
class Infrastructure {
    private:
        Uint             nTrolleys;   //Number of active Trolleys in the run
        string          TrolleysID; //Active trolley IDs written into a string
        vector<Trolley*> Trolleys; //List of active Trolleys (struct)

    public:
        //Constructors and destructor
        Infrastructure();
        Infrastructure(IniFile* geofile);
        Infrastructure(const Infrastructure& other);
        ~Infrastructure();
        Infrastructure& operator=(const Infrastructure& other);

        //Get Infrastructure members
        Uint  GetNTrolleys();
        string GetTrolleysID();
        Uint  GetTrolleyID(Uint t);

2057
        //Manage Trolleys
        Trolley* GetTrolley(Uint t);
        void     DeleteTrolley(Uint t);

        //Methods to get members of GIFTrolley objects stored in Trolleys
        Uint  GetNSlots(Uint t);
        string GetSlotsID(Uint t);
        Uint  GetSlotID(Uint t, Uint s);
        RPC*  GetRPC(Uint t, Uint r);

        //Methods to get members of RPC objects stored in RPCs
        string GetName(Uint t, Uint r);
        Uint  GetNGaps(Uint t, Uint r);
        Uint  GetNPartitions(Uint t, Uint r);
        Uint  GetNStrips(Uint t, Uint r);
        string GetGap(Uint t, Uint r, Uint g);
        float  GetGapGeo(Uint t, Uint r, Uint g);
        float  GetStripGeo(Uint t, Uint r, Uint p);
    };

```

Source Code B.7: Description of C++ object *Infrastructure* that contains the full information about CMS RPC experiment in GIF++.

2059 B.5 Handeling of data

2060 As discussed in Appendix A.4.2, the raw data as a `TTree` architecture where every entry is related to
 2061 a trigger signal provided by a muon or a random pulse, whether the goal of the data taking was to
 2062 measure the performance of the detector or the noise/gamma background respectively. Each of these
 2063 entries, referred also as events, contain a more or less full list of hits in the TDC channels to which
 2064 the detectors are connected. To this list of hits corresponds a list of time stamps, marking the arrival
 2065 of the hits within the TDC channel.

2066 The infrastructure of the CMS RPC experiment within GIF++ being defined, combining the
 2067 information about the raw data with the information provided by both the mapping/mask file and the
 2068 dimension file allows to build new physical objects that will help in computing efficiency or rates.

2069 B.5.1 RPC hits

2070 The raw data stored in the ROOT file as output of the GIFT++ DAQ, is readout by the analysis tool
 2071 using the structure `RAWData` presented in Source Code B.9 that differs from the structure presented
 2072 in Appendix A.4.2 as it is not meant to hold all of the data contained in the ROOT file. In this sense,
 2073 this structure is in the case of the offline analysis tool not a dynamical object and will only be storing
 2074 a single event contained in a single entry of the `TTree`.

2075

```

class RPCHit {
    private:
        Uint Channel;      //RPC channel according to mapping (5 digits)
        Uint Trolley;     //0, 1 or 3 (1st digit of the RPC channel)
        Uint Station;     //Slot where is held the RPC in Trolley (2nd digit)
        Uint Strip;       //Physical RPC strip where the hit occurred (last 3
    →   digits)
        Uint Partition;   //Readout partition along eta segmentation
        float TimeStamp;  //Time stamp of the arrival in TDC

    public:
        //Constructors, destructor & operator =
        RPCHit();
        RPCHit(Uint channel, float time, Infrastructure* Infra);
        RPCHit(const RPCHit& other);
        ~RPCHit();
        RPCHit& operator=(const RPCHit& other);

        //Get RPCHit members
        Uint GetChannel();
        Uint GetTrolley();
        Uint GetStation();
        Uint GetStrip();
        Uint GetPartition();
        float GetTime();
    };

    typedef vector<RPCHit> HitList;
    typedef struct GIFHitList { HitList rpc[NTROLLEYS][NSLOTS][NPARTITIONS]; }
    →   GIFHitList;

    bool SortHitbyStrip(RPCHit h1, RPCHit h2);
    bool SortHitbyTime(RPCHit h1, RPCHit h2);
}

```

2076

Source Code B.8: Description of C++ object `RPCHit`.

2077
 2078

```

struct RAWData{
    int          iEvent;    //Event i
    int          TDCNHits; //Number of hits in event i
    int          QFlag;    //Quality flag list (1 flag digit per TDC)
    vector<Uint> *TDCCh;  //List of channels giving hits per event
    vector<float> *TDCTS;   //List of the corresponding time stamps
};

```

2079

Source Code B.9: Description of C++ structure `RAWData`.

2080
 2081
 2082

Each member of the structure is then linked to the corresponding branch of the ROOT data tree,
 as shown in the example of Source Code B.10, and using the method `GetEntry(int i)` of the ROOT
 class `TTree` will update the state of the members of `RAWData`.

```

2083   TTree* dataTree = (TTree*)dataFile.Get("RAWData");
2084   RAWData data;
2085
2086   dataTree->SetBranchAddress("EventNumber", &data.iEvent);
2087   dataTree->SetBranchAddress("number_of_hits", &data.TDCNHits);
2088   dataTree->SetBranchAddress("Quality_flag", &data.QFlag);
2089   dataTree->SetBranchAddress("TDC_channel", &data.TDCCh);
2090   dataTree->SetBranchAddress("TDC_TimeStamp", &data.TDCTS);

```

2085 *Source Code B.10: Example of link in between RAWData and TTree.*

2086 The data is then analysed entry by entry and to each element of the TDC channel list, a `RPCHit` is
 2087 constructed by linking each TDC channel to the corresponding RPC channel thanks to the `Mapping`
 2088 object. The information carried by the RPC channel format allows to easily retrieve the trolley and
 2089 slot from which the hit was recorded (see section B.3.2). Using these 2 values, the readout partition
 2090 can be found by knowing the strip channel and comparing it with the number of partitions and strips
 2091 per partition stored into the `Infrastructure` object.

2092 Thus `RPCHit` objects are then stored into 3D dynamical list called `GIFHitList` (Source Code B.9)
 2093 where the 3 dimensions refer to the 3 layers of the readout in `GIF++` : in the bunker there are *trolleys*
 2094 (τ) holding detectors in *slots* (s) and each detector readout is divided into 1 or more pseudo-rapidity
 2095 *partitions* (p). Using these 3 information allows to assign an address to each readout partition and
 2096 this address will point to a specific hit list.

2097

2098 **B.5.2 Clusters of hits**

2099 All the hits contained in the ROOT file have been sorted into the different hit lists through the
 2100 `GIFHitList`. At this point, it is possible to start looking for clusters. A cluster is a group of adjacent
 2101 strips getting hits within a time window of 25 ns. These strips are then assumed to be part of the same
 2102 physical avalanche signal generated by a muon passing through the chamber or by the interaction of
 2103 a gamma stopping into the electrodes of the RPCs.

2104 To keep the cluster information, `RPCCluster` objects have been defined as shown in Source
 2105 Code B.11. Using the information of each individual `RPCHit` taken out of the hit list, it stores
 2106 the cluster size (number of adjacent strips composing the cluster), the first and last hit, the center for
 2107 spatial reconstruction and finally the start and stop time stamps as well as te time spread in between
 2108 the first and last hit.

```

2109 class RPCCluster{
2110     private:
2111         Uint ClusterSize; //Size of cluster #ID
2112         Uint FirstStrip; //First strip of cluster #ID
2113         Uint LastStrip; //Last strip of cluster #ID
2114         float Center; //Center of cluster #ID ((first+last)/2)
2115         float StartStamp; //Time stamp of the earliest hit of cluster #ID
2116         float StopStamp; //Time stamp of the latest hit of cluster #ID
2117         float TimeSpread; //Time difference between earliest and latest hits
2118                                     //of cluster #ID
2119
2120     public:
2121         //Constructors, destructor & operator =
2122         RPCCluster();
2123         RPCCluster(HitList List, Uint cID, Uint cSize, Uint first, Uint firstID);
2124         RPCCluster(const RPCCluster& other);
2125         ~RPCCluster();
2126         RPCCluster& operator=(const RPCCluster& other);
2127
2128         //Get Cluster members
2129         Uint GetID();
2130         Uint GetSize();
2131         Uint GetFirstStrip();
2132         Uint GetLastStrip();
2133         float GetCenter();
2134         float GetStart();
2135         float GetStop();
2136         float GetSpread();
2137     };
2138
2139 typedef vector<RPCCluster> ClusterList;
2140
2141 //Other functions to build cluster lists out of hit lists
2142 void BuildClusters(HitList &cluster, ClusterList &clusterList);
2143 void Clusterization(HitList &hits, TH1 *hcSize, TH1 *hcMult);

```

Source Code B.11: Description of C++ object cluster.

To investigate the hit list of a given detector partition, the function `Clusterization()` defined in `include/Cluster.h` needs the hits in the list to be time sorted. This is achieved by calling function `sort()` of library `<algorithm>` using the comparator `SortHitbyTime(RPCHit h1, RPCHit h2)` defined in `include/RPCHit.h` that returns `true` if the time stamp of hit `h1` is lower than that of `h2`. A first isolation of strips is made only based on time information. All the hits within the 25 ns window are taken separately from the rest. Then, this sub-list of hits is sorted this time by ascending strip number, using this time the comparator `SortHitbyStrip(RPCHit h1, RPCHit h2)`. Finally, the groups of adjacent strips are used to construct `RPCCluster` objects that are then stored in a temporary list of clusters that is at the end of the process used to know how many clusters were reconstructed and to fill their sizes into an histogram that will allows to know the mean size of muon or gamma clusters.

2124 B.6 DAQ data Analysis

2125 All the ingredients to analyse GIF++ data have been defined. This section will focus on the different
2126 part of the analysis performed on the data, from determining the type of data the tool is dealing with

2127 to calculating the rate in each detector or reconstructing muon or gamma clusters.

2128 B.6.1 Determination of the run type

2129 In GIF++, both the performance of the detectors in detecting muons in an irradiated environment and
 2130 the gamma background can be independantly measured. These corresponds to different run types
 2131 and thus, to different TDC settings giving different data to look at.

2132

2133 In the case of performance measurements, the trigger for data taking is provided by the coïncidence
 2134 of several scintillators when muons from the beam passing through the area are detected. Data
 2135 is collected in a 600 ns wide window around the arrival of muons in the RPCs. The expected time
 2136 distribution of hits is shown in Figure B.1a. The muon peak is clearly visible in the center of the
 2137 distribution and is to be extracted from the gamma background that composes the flat part of the
 2138 distribution.

2139 On the other hand, gamma background or noise measurements are focussed on the non muon
 2140 related physics and the trigger needs to be independant from the muons to give a good measurement
 2141 of the gamma/noise distribution as seen by the detectors. The trigger is then provided by a pulse
 2142 generator at a frequency of 300 Hz whose pulse is not likely to be on time with a muon. In order
 2143 to increase the integrated time without increasing the acquisition time too much, the width of the
 2144 acquisition windows are increased to 10 μ s. The time distribution of the hits is expected to be flat, as
 2145 shown by Figure B.1b.

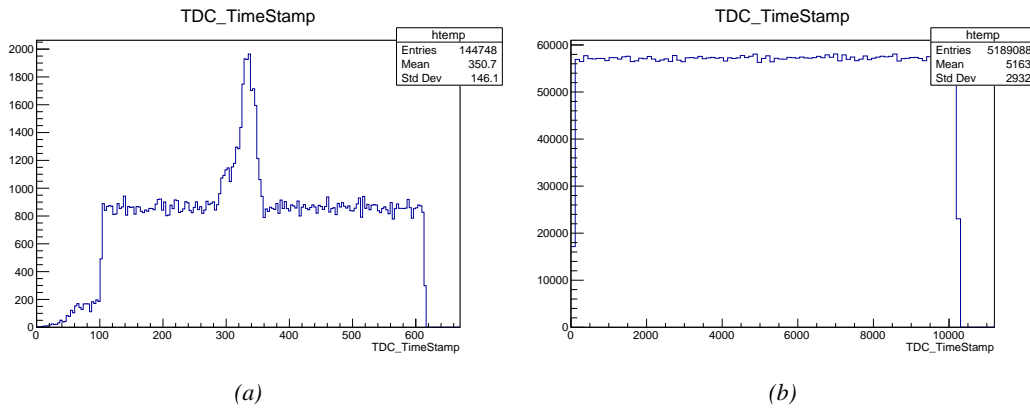


Figure B.1: Example of expected hit time distributions in the cases of efficiency (Figure B.1a) and noise/gamma rate per unit area (Figure B.1b) measurements as extracted from the raw ROOT files. The unit along the x-axis corresponds to ns. The fact that "the" muon peak is not well defined in Figure B.1a is due to the contribution of all the RPCs being tested at the same time that don't necessarily have the same signal arrival time. Each individual peak can have an offset with the ones of other detectors. The inconsistency in the first 100 ns of both time distributions is an artefact of the TDCs and are systematically rejected during the analysis.

2146 The ROOT files include a TTree called RunParameters containing, among other things, the in-
 2147 formation related to the type of run. The run type can then be accessed as described by Source
 2148 Code B.12 and the function IsEfficiencyRun() is then used to determine if the run file is an effi-
 2149 ciency run or, on the contrary, another type of run (noise or gamma measurement).

```

2150
2151     TTree* RunParameters = (TTree*)dataFile.Get("RunParameters");
2152     TString* RunType = new TString();
2153     RunParameters->SetBranchAddress("RunType", &RunType);
2154     RunParameters->GetEntry(0);

```

2152 *Source Code B.12: Access to the run type contained in `TTree* RunParameters`.*

2153 Finally, the data files will have a slightly different content whether it was collected before or after
 2154 October 2017 and the upgrade of the DAQ software that brought a new information into the ROOT
 2155 output. This is discussed in Appendix A.4.3 and implies that the analysis will differ a little depending
 2156 on the data format. Indeed, as no information on the data quality is stored, in older data files, the cor-
 2157 rections for missing events has to be done at the end of the analysis. The information about the type
 2158 of data format is stored in the variable `bool isNewFormat` by checking the list of branches contained
 2159 in the data tree via the methods `TTree::GetListOfBranches()` and `TCollection::Contains()`.

2160 B.6.2 Beam time window calculation for efficiency runs

2161 Knowing the run type is important first of all to know the width of the acquisition window to be used
 2162 for the rate calculation and finally to be able to seek for muons. Indeed, the peak that appears in the
 2163 time distribution for each detectors is then fitted to extract the most probable time window in which
 2164 the tool should look for muon hits. The data outside of this time window is then used to evaluate the
 2165 noise or gamma background the detector was subjected to during the data taking. Computing the
 2166 position of the peak is done calling the function `SetBeamWindow()` defined in file `src/RPCHit.cc` that
 2167 loops a first time on the data. The data is first sorted in a 3D array of 1D histograms (`GIFH1Array`, see
 2168 `include/types.h`). Then the location of the highest bin is determined using `TH1::GetMaximumBin()`
 2169 and is used to define a window in which a gaussian fit will be applied to compute the peak width.
 2170 This window is a 80 ns defined by Formula B.1 around the central bin.

$$t_{center}(ns) = \text{bin} \times \text{width}_{\text{bin}}(ns) \quad (\text{B.1a})$$

$$[t_{low}; t_{high}] = [t_{center} - 40; t_{center} + 40] \quad (\text{B.1b})$$

2171 Before the fit is performed, the average number of noise/gamma hits per bin is evaluated using
 2172 the data outside of the fit window. Excluding the first 100 ns, the average number of hits per bin
 2173 due to the noise or gamma is defined by Formula B.2 after extracting the amount of hits in the time
 2174 windows $[100; t_{low}]$ and $[t_{high}; 600]$ thanks to the method `TH1::Integral()`. This average number
 2175 of hits is then subtracted to every bin of the 1D histogram, in order to *clean* it from the noise or
 2176 gamma contribution as much as possible to improve the fit quality. Bins where $\langle n_{\text{hits}} \rangle$ is greater
 2177 than the actual bin content are set to 0.

$$\Delta t_{noise}(ns) = 600 \overbrace{-t_{high} + t_{low}}^{-80ns} - 100 = 420ns \quad (\text{B.2a})$$

$$\langle n_{\text{hits}} \rangle = \text{width}_{\text{bin}}(ns) \times \frac{\sum_{t=100}^{t_{low}} + \sum_{t=t_{high}}^{600}}{\Delta t_{noise}(ns)} \quad (\text{B.2b})$$

2178 Finally, the fit parameters are extracted and saved for each detector in 3D arrays of `float`
 2179 (`muonPeak`, see `include/types.h`), a first one for the mean arrival time of the muons, `PeakTime`,

2180 and a second one for the width of the peak, `PeakWidth`. The width is defined as 6σ of the gaussian
 2181 fit. The same settings are applied to every partitions of the same detector. To determine which one
 2182 of the detector's partitions is directly illuminated by the beam, the peak height of each partition is
 2183 compared and the highest one is then used to define the peak settings.

2184 **B.6.3 Data loop and histogram filling**

2185 3D arrays of histogram are created to store the data and display it on the DQM of GIF++ webDCS
 2186 for the use of shifters. These histograms, presented in section B.2.1.1, are filled while looping on
 2187 the data. Before starting the analysis loop, it is necessary to control the entry quality for the new
 2188 file formats featuring `QFlag`. If the `QFlag` value for this entry shows that 1 TDC or more have a
 2189 `CORRUPTED` flag, then this event is discarded. The loss of statistics is low enough to be neglected.
 2190 `QFlag` is controled using the function `IsCorruptedEvent()` defined in `src/utils.cc`. As explained
 2191 in Appendix A.4.3, each digit of this integer represent a TDC flag that can be 1 or 2. Each 2 is
 2192 the sign of a `CORRUPTED` state. Then, the data is accessed entry by entry in the ROOT `TTree` using
 2193 `RAWData` and each hit in the hit list is assigned to a detector channel and saved in the corresponding
 2194 histograms. In the first part of the analysis, in which the loop over the ROOT file's content is
 2195 performed, the different steps are:

2196 **1- RPC channel assignment and control:** a check is done on the RPC channel extracted thanks
 2197 to the mapping via the method `Mapping::GetLink()`. If the channel is not initialised and is 0, or if
 2198 the TDC channel was greater than 5127, the hit is discarded. This means there was a problem in the
 2199 mapping. Often a mapping problem leads to the crash of the offline tool.

2200 **2- Creation of a `RPCHit` object:** to easily get the trolley, slot and partition in which the hit has
 2201 been assigned, this object is particularly helpful.

2202 **3- General histograms are filled:** the hit is filled into the time distribution and the general hit
 2203 distribution histograms, and if the arrival time is within the first 100 ns, it is discarded and nothing
 2204 else happens and the loop proceeds with the next hit in the list.

2205 **4- Multiplicity counter:** the hit multiplicity counter of the corresponding detectors incremented.

2206 **5-a- Efficiency runs - Is the hit within the peak window? :** if the peak is contained in the peak
 2207 window previously defined in section B.6.2, the hit is filled into the beam hit profile histogram of
 2208 the corresponding chamber, added into the list of muon hits and increments the counter of *in time*
 2209 hits. The term *in time* here refers to the hits that are likely to be muons by arriving in the expected
 2210 time window. If the hit is outside of the peak window, it is filled into the noise profile histogram
 2211 of the corresponding detector, added into the list of noise/gamma hits and increments the counter of
 2212 noise/gamma hits.

2213 **5-b- Noise/gamma rate runs - Noise histograms are filled:** the hit is filled into the noise profile
 2214 histogram of the corresponding detector, added into the list of noise/gamma hits and increments the
 2215 counter of noise/gamma hits.

2216

2217 After the loop on the hit list of the entry is over, the next step is to clusterize the 3D lists filled
 2218 in the previous steps. A 3D loop is then started over the active trolley, slot and RPC partitions to
 2219 access these objects. Each `NoiseHitList` and `MuonHitList`, in case of efficiency run, are clusterized
 2220 as described in section B.5.2. There corresponding cluster size and multiplicity histograms are filled
 2221 at the end of the clustering process. Then, the efficiency histogram is filled in case of efficiency run.
 2222 The selection is simply made by checking whether the RPC detected signals in the peak window
 2223 during this event. Nevertheless, it is useful to highlight that at this level, it is not possible yet to
 2224 discriminate in between a muon hit and noise or gamma hit. Thus, `MuonCSize_H`, `MuonCMult_H`
 2225 and `Efficiency0_H` are subjected to noise and gamma contamination. This contamination will be
 2226 estimated and corrected at the moment the results will be written into output CSV files. Finally, the
 2227 loop ends on the filling of the general hit multiplicity histogram.

2228 **B.6.4 Results calculation**

2229 As mentioned in section B.2.1, the analysis of DAQ data provides the user with 3 CSV files and
 2230 a ROOT file associated to each and every ROOT data file. The fourth CSV file is provided by the
 2231 extraction of the CEAN main frame data monitored during data taking and will be discussed later.
 2232 After looping on the data in the previous part of the analysis macro, the output files are created and a
 2233 3D loop on each RPC readout partitions is started to extract the histograms parameters and compute
 2234 the final results.

2235

2236 **B.6.4.1 Rate normalisation**

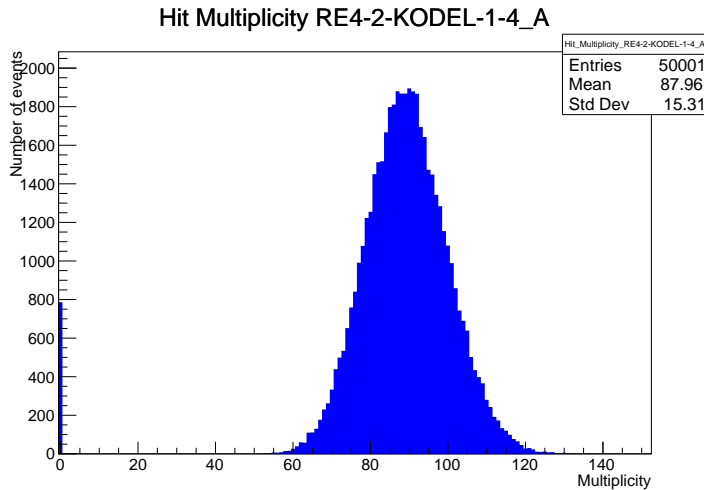


Figure B.2: The effect of the quality flag is explained by presenting the reconstructed hit multiplicity of a data file without `Quality_flag`. The artificial high content of bin 0 is the effect of corrupted data.

2237 To analyse old data format files, not containing any quality flag, it is needed to estimate the amount
 2238 of corrupted data via a fit as the corrupted data will always fill events with a fake "0 multiplicity".
 2239 Indeed, as no hits were stored in the DAQ ROOT files, these events artificially contribute to fill
 2240 the bin corresponding to a null multiplicity, as shown in Figure B.2. In the case the mean of the

hit multiplicity distribution is high, the contribution of the corrupted data can easily be evaluated for later correction by comparing the level of the bin at multiplicity 0 and of a skew fit curve that should indicate a value consistent with 0. A skew fit has been chosen over a Poisson fit as it was giving better results for lower mean multiplicity values. Nevertheless, for low irradiation cases, as explained in Appendix A.4.3, the hit multiplicity distribution mean is, on the contrary, rather small and the probability to record events without hits can't be considered small anymore, leading to a difficult and non-reliable estimation of the corruption. As can be seen in Source Code B.13, conditions have been applied to prevent bad fits and wrong corruption estimation in cases where :

- The difference in between the data for multiplicity 1 and the corresponding fit value should be lower than 1% of the total amount of data : $\frac{|n_{m=1} - sk(1)|}{N_{tot}} < 0.01$ where $n_{m=1}$ is the number of entries with multiplicity 1, $sk(1)$ the value of the skew fit, as defined by Formula 4.3, for multiplicity 1 and N_{tot} the total number of entries.

- The amount of data contained in the multiplicity 0 bin should not exceed 40% : $\frac{n_{m=0}}{N_{tot}} \leq 0.4$ where $n_{m=0}$ is the number of entries with multiplicity 0. This number has been determined to be the maximum to be able to separate the excess of data due to corruption from the hit multiplicity distribution.

Those 2 conditions need to be fulfilled to estimate the corruption of old data format files. If the fit was successful, the level of corruption is written in `Offline-Corrupted.csv` and the number of corrupted entries, refered as the integer `nEmptyEvent`, is subtracted from the total number of entries when the rate normalisation factor is computed as explicit in Source Code B.13. Note that for new data format files, the number of corrupted entries being set to 0, the definition of `rate_norm` stays valid.

```

2263
if(!isNewFormat){
    TF1* GaussFit = new TF1("gaussfit","[0]*exp(-0.5*((x-[1])/[2])**2)",0,Xmax);
    GaussFit->SetParameter(0,100);
    GaussFit->SetParameter(1,10);
    GaussFit->SetParameter(2,1);
    HitMultiplicity_H.rpc[T][S][p]->Fit(GaussFit,"LIQR","",0.5,Xmax);

    TF1* SkewFit = new TF1("skewfit","[0]*exp(-0.5*((x-[1])/[2])**2) / (1 +
→ exp(-[3]*(x-[4])))",0,Xmax);
    SkewFit->SetParameter(0,GaussFit->GetParameter(0));
    SkewFit->SetParameter(1,GaussFit->GetParameter(1));
    SkewFit->SetParameter(2,GaussFit->GetParameter(2));
    SkewFit->SetParameter(3,1);
    SkewFit->SetParameter(4,1);
    HitMultiplicity_H.rpc[T][S][p]->Fit(SkewFit,"LIQR","",0.5,Xmax);

    double fitValue = SkewFit->Eval(1,0,0,0);
    double dataValue = (double)HitMultiplicity_H.rpc[T][S][p]->GetBinContent(2);
    double difference = TMath::Abs(dataValue - fitValue);
    double fitTOdataVSentries_ratio = difference / (double)nEntries;
    bool isFitGOOD = fitTOdataVSentries_ratio < 0.01;

2264
    double nSinglehit = (double)HitMultiplicity_H.rpc[T][S][p]->GetBinContent(1);
    double lowMultRatio = nSinglehit / (double)nEntries;
    bool isMultLOW = lowMultRatio > 0.4;

    if(isFitGOOD && !isMultLOW){
        nEmptyEvent = HitMultiplicity_H.rpc[T][S][p]->GetBinContent(1);
        nPhysics = (int)SkewFit->Eval(0,0,0,0);
        if(nPhysics < nEmptyEvent)
            nEmptyEvent = nEmptyEvent-nPhysics;
    }
}

double corrupt_ratio = 100.*(double)nEmptyEvent / (double)nEntries;
outputCorrCSV << corrupt_ratio << '\t';

float rate_norm = 0.;
float stripArea = GIFIInfra->GetStripGeo(tr,sl,p);

if(IsEfficiencyRun(RunType)){
    float noiseWindow = BMTDCWINDOW - TIMEREJECT - 2*PeakWidth.rpc[T][S][p];
    rate_norm = (nEntries-nEmptyEvent)*noiseWindow*1e-9*stripArea;
} else
    rate_norm = (nEntries-nEmptyEvent)*RDMNOISEWDW*1e-9*stripArea;

```

Source Code B.13: Definition of the rate normalisation variable. It takes into account the number of non corrupted entries and the time window used for noise calculation, to estimate the total integrated time, and the strip active area to express the result as rate per unit area.

2266 B.6.4.2 Rate and activity

2267 At this point, the strip rate histograms, StripNoiseProfile_H.rpc[T][S][p], only contain an in-
2268 formation about the total number of noise or rate hits each channel received during the data taking.
2269 As described in Source Code B.14, a loop on the strip channels will be used to normalise the content
2270 of the rate distribution histogram for each detector partitions. The initial number of hits recorded for
2271 a given bin will be extracted and 2 values will be computed:

- 2272 ● the strip rate, defined as the number of hits recorded in the bin normalised like described in
 2273 the previous section, using the variable `rate_norm`, and

- 2274 ● the strip activity, defined as the number of hits recorded in the bin normalised to the average
 2275 number of hits per bin contained in the partition histogram, using the variable `averageNhit`.
 2276 This value provides an information on the homogeneity of the detector response to the gamma
 2277 background or of the detector noise. An activity of 1 corresponds to an average response.
 2278 Above 1, the channel is more active than the average and bellow 1, the channel is less active.

```

int nNoise = StripNoiseProfile_H.rpc[T][S][p]->GetEntries();
float averageNhit = (nNoise>0) ? (float)(nNoise/nStripsPart) : 1.;

for(Uint st = 1; st <= nStripsPart; st++) {
    float stripRate =
        StripNoiseProfile_H.rpc[T][S][p]->GetBinContent(st)/rate_norm;
    float stripAct =
        StripNoiseProfile_H.rpc[T][S][p]->GetBinContent(st)/averageNhit;

    StripNoiseProfile_H.rpc[T][S][p]->SetBinContent(st,stripRate);
    StripActivity_H.rpc[T][S][p]->SetBinContent(st,stripAct);
}

```

2280 *Source Code B.14: Description of the loop that allows to set the content of each strip rate and strip activity
 channel for each detector partition.*

2281 On each detector partitions, which are readout by a single FEE, all the channels are not processed
 2282 by the same chip. Each chip can give a different noise response and thus, histograms using a chip
 2283 binning are used to investigate chip related noise behaviours. The average values of the strip rate
 2284 or activity grouped into a given chip are extracted using the using the function `GetChipBin()` and
 2285 stored in dedicated histograms as described in Source Codes B.15 and B.16 respectively.

```

float GetChipBin(TH1* H, Uint chip){
    Uint start = 1 + chip*NSTRIPSCHIP;
    int nActive = NSTRIPSCHIP;
    float mean = 0.;

    for(Uint b = start; b <= (chip+1)*NSTRIPSCHIP; b++) {
        float value = H->GetBinContent(b);
        mean += value;
        if(value == 0.) nActive--;
    }

    if(nActive != 0) mean /= (float)nActive;
    else mean = 0.;

    return mean;
}

```

2288 *Source Code B.15: Function used to compute the content of a bin for an histogram using chip binning.*

```

2289   for(UInt ch = 0; ch < (nStripsPart/NSTRIPSCHIP); ch++) {
      ChipMeanNoiseProf_H.rpc[T][S][p]->
          SetBinContent(ch+1,GetChipBin(StripNoiseProfile_H.rpc[T][S][p],ch));
      ChipActivity_H.rpc[T][S][p]->
          SetBinContent(ch+1,GetChipBin(StripActivity_H.rpc[T][S][p],ch));
}

```

Source Code B.16: Description of the loop that allows to set the content of each chip rate and chip activity bins for each detector partition knowing the information contained in the corresponding strip distribution histograms.

The activity variable is used to evaluate the homogeneity of the detector response to background or of the detector noise. The homogeneity h_p of each detector partition can be evaluated using the formula $h_p = \exp(-\sigma_p^R / \langle R \rangle_p)$, where $\langle R \rangle_p$ is the partition mean rate and σ_p^R is the rate standard deviation calculated over the partition channels. The more homogeneously the rates are distributed and the smaller will σ_p^R be, and the closer to 1 will h_p get. On the contrary, if the standard deviation of the channel's rates is large, h_p will rapidly get to 0. This value is saved into histograms as shown in Source Code B.17 and could in the future be used to monitor through time, once extracted, the evolution of every partition homogeneity. This could be of great help to understand the apparition of eventual hot spots due to ageing of the chambers subjected to high radiation levels. The monitored homogeneity information could then be combined with a monitoring of the activity of each individual channel in order to have a finer information. Monitoring tools have been suggested and need to be developed for this purpose.

```

2303   float MeanPartSDev = GetTH1StdDev(StripNoiseProfile_H.rpc[T][S][p]);
   float strip_homog = (MeanPartRate==0)
     ? 0.
     : exp(-MeanPartSDev/MeanPartRate);
   StripHomogeneity_H.rpc[T][S][p]->Fill("exp -#left(#frac{\#sigma_{Strip
     \rightarrow Rate}}{\#mu_{Strip Rate}}\#right)",strip_homog);
   StripHomogeneity_H.rpc[T][S][p]->GetYaxis()->SetRangeUser(0.,1.);

2304   float ChipStDevMean = GetTH1StdDev(ChipMeanNoiseProf_H.rpc[T][S][p]);
   float chip_homog = (MeanPartRate==0)
     ? 0.
     : exp(-ChipStDevMean/MeanPartRate);
   ChipHomogeneity_H.rpc[T][S][p]->Fill("exp -#left(#frac{\#sigma_{Chip
     \rightarrow Rate}}{\#mu_{Chip Rate}}\#right)",chip_homog);
   ChipHomogeneity_H.rpc[T][S][p]->GetYaxis()->SetRangeUser(0.,1.);

```

Source Code B.17: Storage of the homogeneity into dedicated histograms.

2306 B.6.4.3 Strip masking tool

The offline tool is automatically called at the end of each data taking to analyse the data and offer the shifter DQM histograms to control the data quality. After the histograms have been published online in the DQM page, the shifter can decide to mask noisy or dead channels that will contribute to bias the final rate calculation by editing the mask column of `ChannelsMapping.csv` as can be seen in Figure B.3.

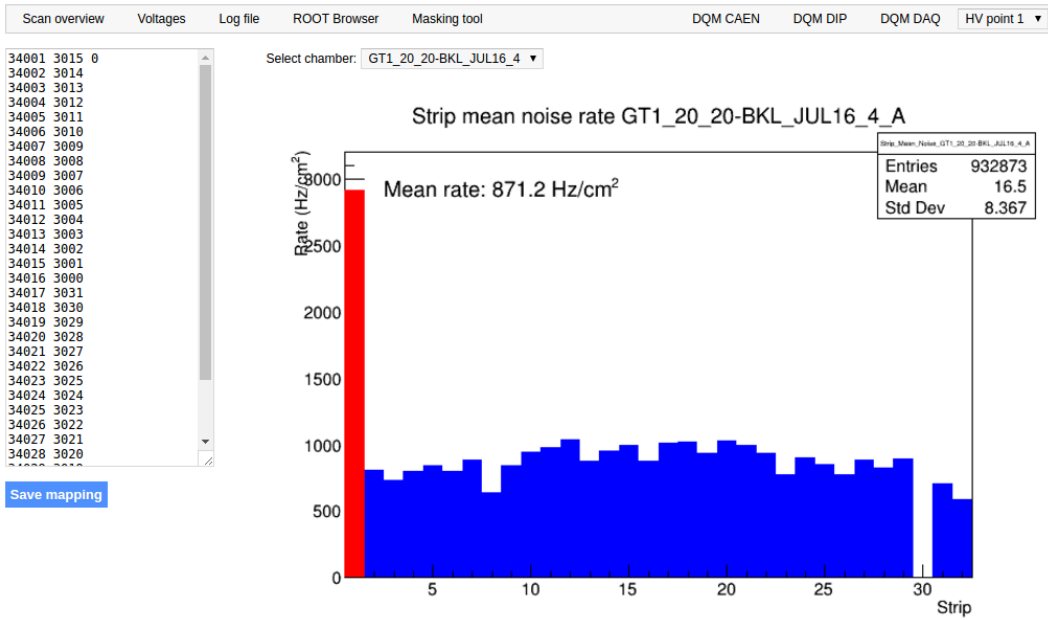


Figure B.3: Display of the masking tool page on the webDCS. The window on the left allows the shifter to edit ChannelsMapping.csv. To mask a channel, it only is needed to set the 3rd field corresponding to the strip to mask to 0. It is not necessary for older mapping file formats to add a 1 for each strip that is not masked as the code is versatile and the default behaviour is to consider missing mask fields as active strips. The effect of the mask is directly visible for noisy channels as the corresponding bin turns red. The global effect of masking strips will be an update of the rate value showed on the histogram that will take into consideration the rejected channels.

2312 From the code point of view, the function `GetTH1Mean()` is used to retrieve the mean rate par-
 2313 tition by partition after the rates have been calculated strip by strip and filled into the histograms
 2314 `StripNoiseProfile_H.rpc[T][S][p]`, as described through Source Code B.18.

2315 Once the mask for each rejected channel has been updated, the shifter can manually run the of-
 2316 fline tool again to update the DQM plots, now including the masked strips, as well the rate results
 2317 written in the output CSV file `Offline-Rate.csv`. If not done during the shifts, the strip masking
 2318 procedure needs to be carefully done by the person in charge of data analysis on the scans that were
 2319 selected to produce the final results.

```

2320
float GetTH1Mean(TH1* H) {
    int nBins = H->GetNbinsX();
    int nActive = nBins;
    float mean = 0.;

    for(int b = 1; b <= nBins; b++) {
        float value = H->GetBinContent(b);
        mean += value;
        if(value == 0.) nActive--;
    }

    if(nActive != 0) mean /= (float)nActive;
    else mean = 0.;

    return mean;
}

```

Source Code B.18: The function `GetTH1Mean()` is used to return the mean along the y-axis of TH1 histograms containing rate information. In order to take into account masked strips whose rate is set to 0, the function looks for masked channels and decrement the number of active channels for each null value found.

2323 B.6.4.4 Output CSV files filling

2324 All the histograms have been filled. Parameters will then be extracted from them to compute the
 2325 final results that will later be used to produce plots. Once the results have been computed, the very
 2326 last step of the offline macro is to write these values into the corresponding CSV outputs. Aside of
 2327 the file `Offline-Corrupted.csv`, 2 CSV files are being written by the macro `offlineAnalysis()`,
 2328 `Offline-Rates.csv` and `Offline-L0-EffCl.csv` that respectively contain information about noise
 2329 or gamma rates, cluster size and multiplicity, and about level 0 reconstruction of the detector effi-
 2330 ciency, muon cluster size and multiplicity. Details on the computation and file writing are respec-
 2331 tively given in Sources Codes B.19 and B.20.

2332 **Noise/gamma background variables** are computed and written in the output file for each detector
 2333 partitions. A detector average of the hit and cluster rate is also provided, as shown through Sources
 2334 Code B.19. The variables that are written for each partition are:

- 2335 • The mean partition hit rate per unit area, `MeanPartRate`, that is extracted from the histogram
 2336 `StripNoiseProfile_H` as the mean value along the y-axis, as described in section B.6.4.3. No
 2337 error is recorded for the hit rate as this is considered a single measurement. No statistical error
 2338 can be associated to it and the systematics are unknown.
- 2339 • The mean cluster size, `cSizePart`, is extracted from the histogram `NoiseCSize_H` and it's
 2340 statistical error, `cSizePartErr`, is taken to be 2σ of the total distribution.
- 2341 • The mean cluster multiplicity per trigger, `cMultPart`, is extracted from the histogram `NoiseCMult_H`
 2342 and it's statistical error, `cMultPartErr`, is taken to be 2σ of the total distribution. It is impor-
 2343 tant to point to the fact that this variable gives an information that is dependent on the buffer
 2344 window width used for each trigger for the calculation.
- 2345 • The mean cluster rate per unit area, `ClustPartRate`, is defined as the mean hit rate normalised

2346 to the mean cluster size and it's statistical error, `ClustPartRateErr`, is then obtained using the
 2347 relative statistical error on the mean cluster size.

```

for (UInt tr = 0; tr < GIFInfra->GetNTrolleys(); tr++){
  UInt T = GIFInfra->GetTrolleyID(tr);

  for (UInt sl = 0; sl < GIFInfra->GetNSlots(tr); sl++){
    UInt S = GIFInfra->GetSlotID(tr,sl) - 1;

    float MeanNoiseRate = 0.;
    float ClusterRate = 0.;
    float ClusterSDev = 0.;

    for (UInt p = 0; p < GIFInfra->GetNPartitions(tr,sl); p++){
      float MeanPartRate = GetTH1Mean(StripNoiseProfile_H.rpc[T][S][p]);
      float cSizePart = NoiseCSIZE_H.rpc[T][S][p]->GetMean();
      float cSizePartErr = (NoiseCSIZE_H.rpc[T][S][p]->GetEntries()==0)
        ? 0.
        : 2*NoiseCSIZE_H.rpc[T][S][p]->GetStdDev() /
          sqrt(NoiseCSIZE_H.rpc[T][S][p]->GetEntries());
      float cMultPart = NoiseCMult_H.rpc[T][S][p]->GetMean();
      float cMultPartErr = (NoiseCMult_H.rpc[T][S][p]->GetEntries()==0)
        ? 0.
        : 2*NoiseCMult_H.rpc[T][S][p]->GetStdDev() /
          sqrt(NoiseCMult_H.rpc[T][S][p]->GetEntries());
      float ClustPartRate = (cSizePart==0) ? 0.
        : MeanPartRate/cSizePart;
      float ClustPartRateErr = (cSizePart==0) ? 0.
        : ClustPartRate * cSizePartErr/cSizePart;

      outputRateCSV << MeanPartRate << '\t'
        << cSizePart << '\t' << cSizePartErr << '\t'
        << cMultPart << '\t' << cMultPartErr << '\t'
        << ClustPartRate << '\t' << ClustPartRateErr << '\t';

      RPCarea += stripArea * nStripsPart;
      MeanNoiseRate += MeanPartRate * stripArea * nStripsPart;
      ClusterRate += ClustPartRate * stripArea * nStripsPart;
      ClusterSDev += (cSizePart==0)
        ? 0.
        : ClusterRate*cSizePartErr/cSizePart;
    }

    MeanNoiseRate /= RPCarea;
    ClusterRate /= RPCarea;
    ClusterSDev /= RPCarea;

    outputRateCSV << MeanNoiseRate << '\t'
      << ClusterRate << '\t' << ClusterSDev << '\t';
  }
}

```

Source Code B.19: Description of rate result calculation and writing into the CSV output `Offline-Rate.csv`. Are saved into the file for each detector, the mean partition rate, cluster size and cluster mutiplicity, along with their errors, for each partition and as well as a detector average.

2350 **Muon performance variables** are computed and written in the output file for each detector partitions as shown through Sources Code B.20. The variables that are written for each partition are:

- 2352 ● The muon efficiency, `eff`, extracted from the histogram `Efficiency0_H`. It is reminded that
2353 this offline tool doesn't include any tracking algorithm to identify muons from the beam and
2354 only relies on the hits arriving in the time window corresponding to the beam time. The con-
2355 tent of the efficiency histogram is thus biased by the noise/gamma background contribution
2356 into this window and is thus corrected by estimating the muon data content in the peak re-
2357 gion knowing the noise/gamma content in the rate calculation region. Both time windows
2358 being different, the choice was made to normalise the noise/gamma background calculation
2359 window to it's equivalent beam window in order to have comparable values using the variable
2360 `windowRatio`. Finally, to estimate the data ratio in the peak region, the variable `DataRatio`
2361 is defined as the ratio in between the estimated mean cluster multiplicity of the muons in the
2362 peak region, `MuonCM`, and of the total mean cluster multiplicity in the peak region, `PeakCM`.
2363 `MuonCM` is itself defined as the difference in between the total mean cluster multiplicity in the
2364 peak region and the normalised mean noise/gamma cluster multiplicity calculated outside of
2365 the peak region. The statistical error related to the efficiency, `eff_err`, is computed using a
2366 binomial distribution, as the efficiency measure the probability of "success" and "failure" to
2367 detect muons.
- 2368
2369
2370
2371
2372
2373 ● The mean muon cluster size, `MuonCS`, is calculated using the total mean cluster size and multi-
2374 plicity in the peak region, respectively extracted from histograms `MuonCSize_H` and `MuonCMult_H`,
2375 the noise/gamma background mean cluster size and normalised multiplicity, extracted from
2376 `NoiseCSize_H` and `NoiseCMult_H`, and of the estimated muon cluster multiplicity `MuonCM` pre-
2377 viously explicated. The associated statistical error, `MuonCM_err`, is calculated using the propa-
2378 gation of errors of the mentioned variables.
- 2379 ● The mean muon cluster multiplicity in the peak region, `MuonCM`, explicated above whose sta-
2380 tistical error, `MuonCM_err`, is the sum of statistical error associated to the total mean clus-
2381 ter multiplicity in the peak reagion, `PeakCM_err`, and of the mean noise/gamma cluster size,
2382 `NoiseCM_err`.

2378 In addition to these 2 CSV files, the histograms are saved in ROOT file `Scan00XXXX_HVY_Offline.root`
2379 as explained in section B.2.1.1.

2380

```

for (UInt tr = 0; tr < GIFInfra->GetNTrolleys(); tr++) {
    UInt T = GIFInfra->GetTrolleyID(tr);
    for (UInt sl = 0; sl < GIFInfra->GetNSlots(tr); sl++) {
        UInt S = GIFInfra->GetSlotID(tr,sl) - 1;
        for (UInt p = 0; p < GIFInfra->GetNPartitions(tr,sl); p++) {
            float noiseWindow =
                BMTDCWINDOW - TIMEREJECT - 2*PeakWidth.rpc[T][S][p];
            float peakWindow = 2*PeakWidth.rpc[T][S][p];
            float windowRatio = peakWindow/noiseWindow;

            float PeakCM = MuonCMult_H.rpc[T][S][p]->GetMean();
            float PeakCS = MuonCSize_H.rpc[T][S][p]->GetMean();
            float NoiseCM = NoiseCMult_H.rpc[T][S][p]->GetMean() *windowRatio;
            float NoiseCS = NoiseCSize_H.rpc[T][S][p]->GetMean();
            float MuonCM = (PeakCM<NoiseCM) ? 0. : PeakCM-NoiseCM;
            float MuonCS = (MuonCM==0 || PeakCM*PeakCS<NoiseCM*NoiseCS)
                ? 0.
                : (PeakCM*PeakCS-NoiseCM*NoiseCS) / MuonCM;
            float PeakCM_err = (MuonCMult_H.rpc[T][S][p]->GetEntries()==0.)
                ? 0.
                : 2*MuonCMult_H.rpc[T][S][p]->GetStdDev() /
                    sqrt(MuonCMult_H.rpc[T][S][p]->GetEntries());
            float PeakCS_err = (MuonCSize_H.rpc[T][S][p]->GetEntries()==0.)
                ? 0.
                : 2*MuonCSize_H.rpc[T][S][p]->GetStdDev() /
                    sqrt(MuonCSize_H.rpc[T][S][p]->GetEntries());
            float NoiseCM_err = (NoiseCMult_H.rpc[T][S][p]->GetEntries()==0.)
                ? 0.
                : windowRatio*2*NoiseCMult_H.rpc[T][S][p]->GetStdDev() /
                    sqrt(NoiseCMult_H.rpc[T][S][p]->GetEntries());
            float NoiseCS_err = (NoiseCSize_H.rpc[T][S][p]->GetEntries()==0.)
                ? 0.
                : 2*NoiseCSize_H.rpc[T][S][p]->GetStdDev() /
                    sqrt(NoiseCSize_H.rpc[T][S][p]->GetEntries());
            float MuonCM_err = (MuonCM==0) ? 0. : PeakCM_err+NoiseCM_err;
            float MuonCS_err = (MuonCS==0 || MuonCM==0) ? 0.
                : (PeakCS*PeakCM_err + PeakCM*PeakCS_err +
                    NoiseCS*NoiseCM_err + NoiseCM*NoiseCS_err +
                    MuonCS*MuonCM_err) / MuonCM;

            float DataRatio = MuonCM/PeakCM;
            float DataRatio_err = (MuonCM==0) ? 0.
                : DataRatio*(MuonCM_err/MuonCM + PeakCM_err/PeakCM);
            float eff = DataRatio*Efficiency0_H.rpc[T][S][p]->GetMean();
            float eff_err = DataRatio*2*Efficiency0_H.rpc[T][S][p]->GetStdDev() /
                sqrt(Efficiency0_H.rpc[T][S][p]->GetEntries()) +
                Efficiency0_H.rpc[T][S][p]->GetMean()*DataRatio_err;

            outputEffCSV << eff << '\t' << eff_err << '\t'
                << MuonCS << '\t' << MuonCS_err << '\t'
                << MuonCM << '\t' << MuonCM_err << '\t';
        }
    }
}

```

2381

Source Code B.20: Description of efficiency result calculation and writing into the CSV output Offline-L0-EffCl.csv. Are saved into the file for each detector, the efficiency, corrected taking into account the background in the peak window of the time profile, muon cluster size and muon cluster multiplicity, along with their errors, for each partition and as well as a detector average.

2382

2383 B.7 Current data Analysis

2384 Detectors under test at GIF++ are connected both to a CAEN HV power supply and to a CAEN
2385 ADC that reads the currents inside of the RPC gaps bypassing the supply cable. During data tak-
2386 ing, the webDCS records into a ROOT file called `Scan00XXXX_HVY_CAEN.root` histograms with the
2387 monitored parameters of both CAEN devices. Are recorded for each RPC channels (in most cases,
2388 a channel corresponds to an RPC gap):

- 2389 • the effective voltage, HV_{eff} , set by the webDCS using the PT correction on the CAEN power
2390 supply,
- 2391 • the applied voltage, HV_{app} , monitored by the CAEN power supply, and the statistical error
2392 related to the variations of this value through time to follow the variation of the environmental
2393 parameters defined as the RMS of the histogram divided by the square root of the number of
2394 recorded points,
- 2395 • the monitored current, I_{mon} , monitored by the CAEN power supply, and the statistical error
2396 related to the variations of this value through time to follow the variation of the environmental
2397 parameters defined as the RMS of the histogram divided by the square root of the number of
2398 recorded points,
- 2399 • the corresponding current density, J_{mon} , defined as the monitored current per unit area,
2400 $J_{mon} = I_{mon}/A$, where A is the active area of the corresponding gap,
- 2401 • the ADC current, I_{ADC} , recorded through the CAEN ADC module that monitors the dark
2402 current in the gap itself. First of all, the resolution of such a module is better than that of
2403 CAEN power supplies and moreover, the current is not read-out through the HV supply line
2404 but directly at the chamber level giving the real current inside of the detector. The statistical
2405 error is defined as the RMS of the histogram distribution divided by the square root of the
2406 number of recorded points.

2407 Once extracted through a loop over the element of GIF++ infrastructure via the C++ macro
2408 `GetCurrent()`, these parameters, organised in 9 columns per detector HV supply line, are written in
2409 the output CSV file `Offline-Current.csv`. The macro can be found in the file `Current.cc`.

References

2410

- 2411 [1] T. Massam et al. “Experimental observation of antideuteron production”. In: *Il Nuovo Cimento A* 63 (1965), pp. 10–14.
- 2412
- 2413 [2] UA1 Collaboration. “Experimental observation of isolated large transverse energy electrons with associated missing energy at $s = 540 \text{ GeV}$ ”. In: *Physics Letters B* 122 (1983), pp. 103–116.
- 2414
- 2415
- 2416 [3] UA2 Collaboration. “Observation of single isolated electrons of high transverse momentum in events with missing transverse energy at the CERN pp collider”. In: *Physics Letters B* 122 (1983), pp. 476–485.
- 2417
- 2418
- 2419 [4] UA1 Collaboration. “Experimental observation of lepton pairs of invariant mass around $95 \text{ GeV}/c^2$ at the CERN SPS collider”. In: *Physics Letters B* 126 (1983), pp. 398–410.
- 2420
- 2421 [5] UA2 Collaboration. “Evidence for $Z_0 \rightarrow e^+e^-$ at the CERN pp collider”. In: *Physics Letters B* 129 (1983), pp. 130–140.
- 2422
- 2423 [6] ALEPH Collaboration. “Determination of the number of light neutrino species”. In: *Physics Letters B* 231 (1989), pp. 519–529.
- 2424
- 2425 [7] CERN, ed. (1985).
- 2426 [8] CERN, ed. (1986).
- 2427 [9] CERN, ed. (1994).
- 2428 [10] CERN, ed. (1998).
- 2429 [11] CERN, ed. (1999).
- 2430 [12] CERN. Geneva. LHC Experiments Committee. *Letter of Intent for A Large Ion Collider Experiment [ALICE]*, note = CERN-LHCC-93-016. Tech. rep. ALICE Collaboration, 1993.
- 2431
- 2432 [13] CERN. Geneva. LHC Experiments Committee. *ATLAS : technical proposal for a general-purpose pp experiment at the Large Hadron Collider at CERN*, note = CERN-LHCC-94-43. Tech. rep. ATLAS Collaboration, 1994.
- 2433
- 2434
- 2435 [14] CERN. Geneva. LHC Experiments Committee. *CMS : letter of intent by the CMS Collaboration for a general purpose detector at LHC*, note = CERN-LHCC-92-003. Tech. rep. CMS Collaboration, 1992.
- 2436
- 2437
- 2438 [15] CERN. Geneva. LHC Experiments Committee. *LHCb : letter of intent*. Tech. rep. CERN-LHCC-95-5. LHCb Collaboration, 1995.
- 2439
- 2440 [16] L. Evans and P. Bryant. “LHC Machine”. In: *JINST* 3 (2008). S08001.
- 2441 [17] CMS Collaboration ATLAS Collaboration. “Combined Measurement of the Higgs Boson Mass in pp Collisions at $\sqrt{s} = 7$ and 8 TeV with the ATLAS and CMS Experiments”. In: *Physical Review Letters* 114 (2015). 191803.
- 2442
- 2443
- 2444 [18] LHCb Collaboration. “Observation of $J/\psi p$ Resonances Consistent with Pentaquark States in $\Lambda_b^0 \rightarrow J/\psi K^- p$ Decays”. In: *Physical Review Letters* 115 (2015). 072001.
- 2445

- [19] LHCb Collaboration. “Observation of $J/\psi\phi$ Structures Consistent with Exotic States from Amplitude Analysis of $B^+ \rightarrow J/\psi\phi K^+$ Decays”. In: *Physical Review Letters* 118 (2017). 022003.
- [20] CERN. Geneva. *High-Luminosity Large Hadron Collider (HL-LHC) Technical Design Report V. 0.1*. Tech. rep. CERN-2017-007-M. 2017.
- [21] CERN. Geneva. LHC Experiments Committee. *The CMS muon project : Technical Design Report*. Tech. rep. CERN-LHCC-97-032. CMS Collaboration, 1997.
- [22] CERN. Geneva. LHC Experiments Committee. *Technical Proposal for the Phase-II Upgrade of the CMS Detector*. Tech. rep. CERN-LHCC-2015-010. CMS Collaboration, 2015.
- [23] CERN. Geneva. LHC Experiments Committee. *CMS, the Compact Muon Solenoid : technical proposal*. Tech. rep. CERN-LHCC-94-38. CMS Collaboration, 1994.
- [24] R. Santonico and R. Cardarelli. “Development of resistive plate counters”. In: *Nucl. Instr. Meth. Phys. Res.* 187 (1981), pp. 377–380.
- [25] Yu.N. Pestov and G.V. Fedotovich. *A picosecond time-of-flight spectrometer for the VEPP-2M based on local-discharge spark counter*. Tech. rep. SLAC-TRANS-0184. SLAC, 1978.
- [26] W.W. Ash, ed. *Spark Counter With A Localized Discharge*. Vol. SLAC-R-250. 1982, pp. 127–131.
- [27] I. Crotty et al. “The non-spark mode and high rate operation of resistive parallel plate chambers”. In: *NIMA* 337 (1993), pp. 370–381.
- [28] I. Crotty et al. “Further studies of avalanche mode operation of resistive parallel plate chambers”. In: *NIMA* 346 (1994), pp. 107–113.
- [29] R. Cardarelli et al. “Avalanche and streamer mode operation of resistive plate chambers”. In: *NIMA* 382 (1996), pp. 470–474.
- [30] E. Cerron Zeballos et al. “A new type of resistive plate chamber: The multigap RPC”. In: *NIMA* 374 (1996), pp. 132–135.
- [31] M.C.S. Williams. “The development of the multigap resistive plate chamber”. In: *Nucl. Phys. B* 61 (1998), pp. 250–257.
- [32] H. Czyrkowski et al. “New developments on resistive plate chambers for high rate operation”. In: *NIMA* 419 (1998), pp. 490–496.
- [33] P. Camarri et al. “Streamer suppression with SF₆ in RPCs operated in avalanche mode”. In: *NIMA* 414 (1998), pp. 317–324.
- [34] E. Cerron Zeballos et al. “Effect of adding SF₆ to the gas mixture in a multigap resistive plate chamber”. In: *NIMA* 419 (1998), pp. 475–478.
- [35] CERN. Geneva. LHC Experiments Committee. *ATLAS muon spectrometer: Technical design report*. Tech. rep. CERN-LHCC-97-22. ATLAS Collaboration, 1997.
- [36] CERN. Geneva. LHC Experiments Committee. *ALICE Time-Of-Flight system (TOF) : Technical Design Report*. Tech. rep. CERN-LHCC-2000-012. ALICE Collaboration, 2000.
- [37] The CALICE collaboration. “First results of the CALICE SDHCAL technological prototype”. In: *JINST* 11 (2016).
- [38] PoS, ed. *Density Imaging of Volcanoes with Atmospheric Muons using GRPCs*. International Europhysics Conference on High Energy Physics - HEP 2011. 2011.
- [39] C. Lippmann. “Detector Physics of Resistive Plate Chambers”. PhD thesis. Johann Wolfgang Goethe-Universität, 2003.

BIBLIOGRAPHY

- [40] M. Abbrescia et al. “Properties of C₂H₂F₄-based gas mixture for avalanche mode operation of resistive plate chambers”. In: *NIMA* 398 (1997), pp. 173–179.
- [41] G. Battistoni et al. “Sensitivity of streamer mode to single ionization electrons”. In: *NIMA* 235 (1985), pp. 91–97.
- [42] W. Riegler. “Induced signals in resistive plate chambers”. In: *NIMA* 491 (2002), pp. 258–271.
- [43] E. Cerron Zeballos et al. “A comparison of the wide gap and narrow gap resistive plate chamber”. In: *NIMA* 373 (1996), pp. 35–42.
- [44] M. Abbrescia et al. “Cosmic ray tests of double-gap resistive plate chambers for the CMS experiment”. In: *NIMA* 550 (2005), pp. 116–126.
- [45] ALICE Collaboration. “A study of the multigap RPC at the gamma irradiation facility at CERN”. In: *NIMA* 490 (2002), pp. 58–70.
- [46] B. Bonner et al. “A multigap resistive plate chamber prototype for time-of-flight for the STAR experiment at RHIC”. In: *NIMA* 478 (2002), pp. 176–179.
- [47] S. Yang et al. “Test of high time resolution MRPC with different readout modes for the BESIII upgrade”. In: *NIMA* 763 (2014), pp. 190–196.
- [48] A. Akindinov et al. “RPC with low-resistive phosphate glass electrodes as a candidate for the CBM TOF”. In: *NIMA* 572 (2007), pp. 676–681.
- [49] JINST, ed. *Development of the MRPC for the TOF system of the MultiPurpose Detector*. RPC2016: XII Workshop on Resistive Plate Chambers and Related Detectors. 2016.
- [50] M.C.S. Williams. “Particle identification using time of flight”. In: *Journal of Physics G* 39 (2012).
- [51] A. Alici et al. “Aging and rate effects of the Multigap RPC studied at the Gamma Irradiation Facility at CERN”. In: *NIMA* 579 (2007), pp. 979–988.
- [52] M. Abbrescia et al. “The simulation of resistive plate chambers in avalanche mode: charge spectra and efficiency”. In: *NIMA* 431 (1999), pp. 413–427.
- [53] M. Abbrescia et al. “Study of long-term performance of CMS RPC under irradiation at the CERN GIF”. In: *NIMA* 533 (2004), pp. 102–106.
- [54] H.C. Kim et al. “Quantitative aging study with intense irradiation tests for the CMS forward RPCs”. In: *NIMA* 602 (2009), pp. 771–774.
- [55] S. Agosteo et al. “A facility for the test of large-area muon chambers at high rates”. In: *NIMA* 452 (2000), pp. 94–104.
- [56] PoS, ed. *CERN GIF ++ : A new irradiation facility to test large-area particle detectors for the high-luminosity LHC program*. Vol. TIPP2014. 2014, pp. 102–109.
- [57] A. Fagot. *GIF++ DAQ v4.0*. 2017. URL: https://github.com/afagot/GIF_DAQ.
- [58] CAEN. *Mod. V1190-VX1190 A/B, 128/64 Ch Multihit TDC*. 14th ed. 2016.
- [59] CAEN. *Mod. V1718 VME USB Bridge*. 9th ed. 2009.
- [60] W-Ie-Ne-R. *VME 6021-23 VXI*. 5th ed. 2016.
- [61] Wikipedia. *INI file*. 2017. URL: https://en.wikipedia.org/wiki/INI_file.
- [62] S. Carrillo A. Fagot. *GIF++ Offline Analysis v6*. 2017. URL: https://github.com/afagot/GIF_OfflineAnalysis.